Transient Thermal Hazards from Gas Pipeline Ruptures: From Large Scale Testing to Lab-Scale Investigative Techniques

Submitted in accordance with the requirements for the degree of Doctor of Philosophy

The University of Leeds

Energy Research Institute School of Chemical and Process Engineering

April 2024

Nicholas Ian Cowling

The candidate confirms that the work submitted is his/her own, except where work which has formed part of jointly-authored publications has been included. The contribution of the candidate and the other authors to this work has been explicitly indicated below. The candidate confirms that appropriate credit has been given within the thesis where reference has been made to the work of others.

There were two phases to experimental work in this research:

1. Full scale fracture propagation tests and DNV's test site. The purpose of the tests was confidential, however the author had the opportunity to capture thermal radiation and overpressure data while the tests were being conducted. The candidate discussed the layout with DNV's team responsible for the test and installed the experimental apparatus. DNV's team (led by Dan Allason) were responsible for the successful execution of the test. The candidate was responsible for analysis of the thermal radiation and overpressure data.
2. Laboratory scale tests. The candidate instructed members of University of Leeds' laboratory team to make modifications to the standard setup of the cone calorimeter. The candidate led the tests with the assistance of Allison Halvorson (University of Leeds). The candidate was responsible for the analysis of the test results.

LIST OF PUBLICATIONS

This research has resulted in the following conference publication:

N. Cowling, H. Phylaktou, D. Allason, G.E. Andrews. Thermal Radiation Hazards from Gas Pipeline Rupture Fireballs. In: Proc of the Seventh International Symposium on Fire and Explosion Hazards (ISFEH), 2019, Volume 2, Saint Petersburg, Russia.

(Included in Chapter 4)

The candidate led the writing up of the publication. D. Allason was responsible for the successful execution of the tests. Dr Phylaktou and Prof Andrews supervised the research work and proof-read the publication.

ACKNOWLEDGEMENTS

When starting this research in 2015 I was determined that it would not take 9 years to complete. While it is less than 9 years (so a success!), there have been ups and downs which give me a host of people to thank.

Firstly, I would like to express my utmost thanks my supervisor Dr Roth Phylaktou for his support and guidance throughout this period. I would also like thank Prof Gordon Andrews for his constructive comments and suggestions at the outset that have contributed to this research. I would also like to thank SCAPE labs staff, especially Ed Woodhouse who had to put up with a fire alarm activation, not once but twice. As I said at the time, the second alarm I predicted would occur and was for the purposes of the health and safety team who were present!

I would also like express my appreciation to Allison Halvorson who assisted me in completing the laboratory scale experiments. I wish you all the best with your research.

Last but not least, I would like to thank all my family, friends and colleagues for their constant support and encouragement. In particular, my younger brother Paul, the constant messaging was greatly appreciated – it spurred me on no end. Without the support of my family and friends, I would never have got this far.

ABSTRACT

Although natural gas transmission pipelines are one of the safest forms of transporting gas, the average number of gas pipeline rupture incidents per year is 2 in Europe and 13 in the US (2015 to 2019). Such incidents can cause property and environmental damage as well as injuries/fatalities.

This thesis examines the hazards associated with natural gas pipeline ruptures, focusing on fireballs ensuing from immediate gas releases. The study leverages both large scale rupture tests (1.2 m diameter pipeline and 90-ton release) and laboratory scale experiments to advance the understanding of thermal radiation effects and material responses in such scenarios. The large scale tests, in line with other data confirmed that the fraction of heat radiated for natural gas is 0.3, much lower than 0.6 derived from the recently proposed correlation by Wang and co-workers.

Innovatively, a laboratory setup was designed based on the bench scale cone calorimeter, achieving a high coefficient of determination (0.97) when comparing thermal doses from both scales. This setup enabled the examination of materials (plastics and man-made and natural cellulosic substances) response under varying heat fluxes, to better predict ignition risks for common materials like paper, card and plastics.

The research extends the concept of thermal dose that is used for human exposure to different levels of material response (first onset of smoke, piloted ignition, spontaneous ignition). Empirical correlations were established for the materials tested, achieving a coefficient of determination of 0.88. Statistical analysis was conducted providing confidence in the derived correlations.

The versatile laboratory setup was used to evaluate material behaviour in a high-risk scenarios where the exposure to a heat a flux is variable and transient. Consequently this approach could be utilised to other scenarios, such as deflagrations and military applications.

The results have relevance for the risk management of gas pipelines, potentially influencing the analysis currently undertaken.

TABLE OF CONTENTS

LIST OF TABLES

LIST OF FIGURES

NOMENCLATURE

Symbols			
A	Area (m^2)	l_f	Ground level distance to fireball (m)
A_1	Constant (m^{-2} $s^{-1/3}$)	l_t	Thickness (m)
B_1	Constant (m^{-2} $s^{-1/5}$)	M_w	Molecular Weight (g mol^{-1})
Bi	Biot number (-)	$\dot{m}$	Mass flow rate (kg s^{-1})
C	Heat and storage transfer property (J cm^{-3})	m_f	Mass of gas released (fireball) (kg)
c	Speed of light (m s^{-1})	m_p	Mass of gas in pipeline (kg)
C_d	Coefficient of discharge (-)	P	Pressure (Bar)
c_s	Specific heat capacity (J kg^{-1} K^{-1})	$\dot{Q}$	Heat release rate (kW)
D	Pipeline diameter (m)	$\dot{q}$	Heat flux (kW m^{-2})
D_H	Hydraulic diameter (m)	R	Ideal Gas Constant (J K^{-1} mol^{-1})
D_c	Depth of cover (m)	R_f	Radius of fireball (m)
D_{cra}	Depth of crater (m)	r	Distance to receiver (m)
D_f	Diameter of fireball (m)	Re	Reynolds number
d_o	Distance to object (m)	S	Average surface emissive power (kW m^{-2})
F	Friction Factor (-)	s	distance from lens to object (m)
F_r	fraction of heat radiated (-)	s'	distance from lens to image (m)
f	Frequency (hz)	T	Temperature (K)
f_l	Focal Length (mm)	T_d	Duration of fireball (s)
G	Gas flow (m^3 s^{-1})	t	Time (s)
g	Acceleration due to gravity (m s^{-2})	t_B	Time constant (s)
H	Height (m)	V	Volume (m^3)
$\dot{H}_c$	rate of change of heat flux (W cm^{-2} s^{-1})	v	Velocity (m s^{-1})
h	Convective heat transfer coefficient (kW m^{-2} K^{-1})	V_f	View factor (-)
ha	Hectare	x_f	Distance to fireball from receiver (m)
k	Thermal conductivity (kW m^{-1} K^{-1})	y	Height (m)
L	Thermal Dose Units (kW m^{-2})^x	Z	Compressibility factor (-)
l	Length (m)		
Subscripts		**Greek Symbols**	
*	critical	α	Crater wall angle at the top (°)
0	initial value	β	Angle for focal length (°)
max	maximum	ε	Emissivity (-)
r	reduced	λ	Wavelength (m)
u	upstream	σ	Stefan's constant (kW m^{-2} K^{-4})
		ρ	Density (kg m^{-3})
		γ	Heat Capacity Ratio (-)
		τ	Atmospheric transmissivity (-)
		μ	Dynamic viscosity (Pa s or kg m^{-1} s^{-1})
		μ_{kr}	Critical gas velocity (2.54 m s^{-1})
		ν	Kinematic viscosity (m^2 s^{-1})

Abbreviations	
ALARP	As Low As Reasonably Practical
ASME	American Society of Mechanical Engineers
BLEVE	Boiling Liquid Expanding Vapour Explosion
CCPS	Centre for Chemical Process Safety
CDOIF	Chemical and Downstream Oil Industries Forum
COMAH	Control of Major Accident Hazards
DNV	Det Norske Veritas
EGIG	European Gas pipeline Incident data Group
EMF	Electromagnetic Field
FTT	Fire Testing Technology Ltd.
GSMR	Gas Safety (Management) Regulations
HCA	High Consequence Area
HSE	Health and Safety Executive
HSL	Health and Safety Laboratory
LNG	Liquefied Natural Gas
LPG	Liquefied Petroleum Gas
MAPD	Major Accident Prevention Document
MOD	Ministry of Defence
NDT	Non Destructive Testing
NTSB	National Transportation Safety Board
OGP	Oil and Gas Producers
OSGB	Ordnance Survey Great Britain
PE	Polyethylene
PHMSA	Pipeline and Hazardous Materials Safety Administration
PSR	Pipeline Safety Regulations
SLOD	Significant Likelihood of Death
TDC	Top Dead Centre
TDU	Thermal Dose Units
TNO	The Netherlands Organisation
UK	United Kingdom
UV	Ultra violet

CHAPTER 1

INTRODUCTION

Between 1980 and 2010, worldwide natural gas consumption more than doubled from 1.5 to 3.2 trillion cubic metres (1). Consequently, the use of onshore steel natural gas transmission pipelines has increased rapidly since the 1970's. While the use of natural gas for electricity generation is expected to peak in 2036, as the least carbon intensive fossil fuel it will continue to play a role until 2050 based on current forecasts (2). While hydrogen is a possible replacement for natural gas, this is only expected to be 5% of the world's energy demand (2).

To provide natural gas to homes and businesses, onshore below ground gas pipeline networks are used. In countries with a national gas system, onshore gas pipeline networks consist of transmission pipelines, distribution pipelines and installation pipework.

This work is investigating the effects of thermal radiation following the immediate ignition of a ruptured high pressure natural gas transmission pipeline. As will be shown in this introduction this is a risk which has to be continually managed by gas pipeline operators.

Installation pipework is normally the 'customer's pipework' and therefore is located within a premises (after a meter) and generally supplied at low pressure (less than 1 bar). Transmission and distribution pipelines are the means by which gas is transported from terminals to individual premises. The main difference between transmission and distribution pipelines is pressure and material, i.e. transmission pipelines operate at a pressure greater than 15 bar and are constructed of steel compared with 75 mbar-15 bar for distribution pipelines that are predominately constructed of polyethylene (PE). Therefore, generally the hazard distances associated with transmission pipelines differ to those distribution pipelines and installation pipework.

When gas is transported across countries through transmission pipelines, strategically located compressor stations are used to maintain the pressure. For operators of gas transmission pipelines to maximise their investment, the pipeline should be operated as close to its design pressure and flow specifications, typically in the range from 70 to 100 bar. During seasonal demands/variations/fluctuations, it may be that pipelines may operate below these limits, or conversely, during high demand periods, these limits may be exceeded (3).

1.1. Frequency and Consequences of High Pressure Gas Releases

As of 2019, there are over 140,000 km and 485,000 km of onshore transmission pipelines in Europe (4) and America (5), respectively. Other countries with large networks of gas transmission pipelines are shown in Table 1-1. Failure frequencies can be derived based on historical experience of operating transmission pipelines as shown in Table 1-1. In turn the failure frequencies can be used to estimate the likely number of incidents (gas releases) per year which could give rise to a hazardous situation.

Table 1-1 Gas pipeline lengths and estimated incidents by country/territory

Country	Gas Transmission Pipeline Length (km)	Failure frequency (Per km-year (10^{-4}))	Estimated number of incidents (Per year)*
US	485,000 (5)	2.06	100 (6)
EU	140,000 (4)	2.92 (4)	41
Russia	177,700 (7)	Assumed 2.92	52
Canada	117,000 (8)		34
China	76,000 (7)		22
Ukraine	36,720 (7)		11
Africa	31,555 (9)		9
Australia	30,054 (7)		9
*Numbers of incidents are estimated based in historical failure rates. For comparison in the EU, there were over 50 incidents in 1985 but just over 10 in 2019 (4).			

The causes of gas releases from transmission pipelines include external interference, corrosion, inadequate design, ground movement or escalation events. Depending on the cause, the consequences of the incident can range in severity from pinholes/cracks, to holes or to a complete rupture of the pipeline. European Gas pipeline Incident data Group (EGIG) data (4) shows that the percentage of fatalities of as a function of leak size is 0%, 0.08%, and 0.69% pinhole/crack, holes, and ruptures, respectively (see Figure 1-1).

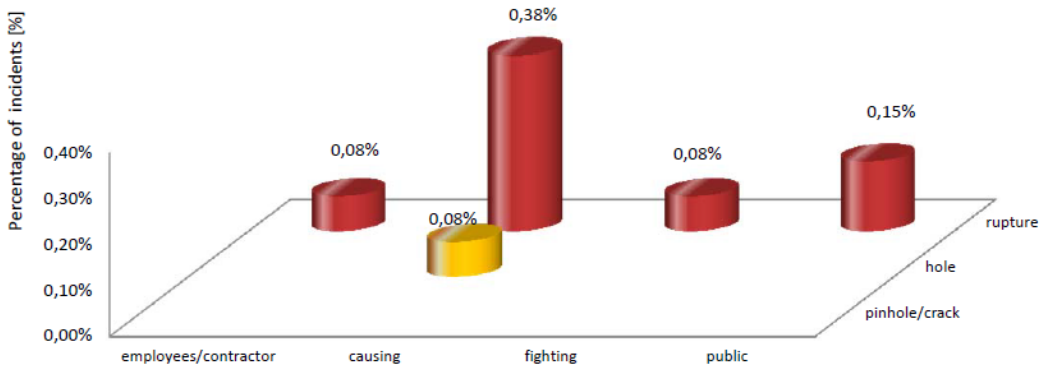

Figure 1-1 Proportion of fatalities from different pipeline failure modes. Reproduced from (4)

The fact that fatalities from ruptures are an order of magnitude higher than from other failure modes indicates the greater risks associated with pipeline ruptures compared to other types of failures.

In Europe (4) there were 1.82 rupture incidents per year on average based on a system length of 140,000 and a rupture failure frequency of 0.013 ruptures per 1000 km per year in the period 2015 to 2019 (inclusive). For the same period in America (6) there were 13.4 rupture incidents per year on average based on 67 ruptures. While the use of historical experience to determine future performance may be over cautious as there has been advances in design, installation, maintenance, implementation of lessons learnt from incidents, the data highlights that such incidents do occur.

Figure 1-1 illustrates that gas pipeline releases can lead to fatalities. Moreover, an ignited release from a transmission pipeline can cause extensive property damage and environmental harm. Considering that gas transmission pipelines traverse open country and are not confined to secure sites, pipeline operators must carefully plan their routes. With population growth and the consequent expansion of residential and commercial developments, the proximity to gas transmission pipelines is likely to increase, elevating the risks. Table 1-2 provides specific examples of fatalities and property damage from selected incidents.

Table 1-2 Data on Pipeline Ruptures Incidents

Location	Date	Diameter (inches)	Duration (mins)	Failure Mode	Fatalities	Property Damage
Edison, New Jersey, US	23rd March 1994	36	~150	Rupture	0	£16.1M
Carlsbad, New Mexico, US	19th August 2000	30	55	Rupture	12	£130k
Ghislenghien, Belgium, EU	30th July 2004	40	20	Rupture	24	£730k
San Bruno, California, US	9th September 2010	30	91	Rupture	8	£364M
Sissonville, West Virgina, US	11th December 2012	20	180	Rupture	0	£650k

1.2. Regulations & Standards

Having identified the frequency of a rupture release is at least a yearly frequency and that previous releases have resulted in fatalities and injuries as well as property and/or environmental damage, this section outlines the Regulations operators of gas transmission have to comply with.

1.2.1. UK and Europe

1.2.1.1. General

In Europe, the regulations are not prescriptive with respect to the design for high pressure pipelines. In Europe, each country has its own national legislation and standards. In the United Kingdom (UK), there are two main items of legislation pipeline operators must comply with; the Pipeline Safety Regulations 1996 (PSR) (10) and the Gas Safety (Management) Regulations 1996 (GSMR) (11).

PSR applies to pipelines operating at a pressure greater than 7 bar. PSR state that a major accident hazard pipelines should have a major accident prevention document (MAPD) which demonstrates that the operator has assessed the risk from major accidents (akin to the Control of Major Accident Hazard Regulations (COMAH) (12)). The MAPD will refer to the pipeline operator's management systems and has to be updated at various stages in the life cycle of the pipeline.

GSMR requires all gas transporters (operators of transmission or distribution networks and not installation pipework) to prepare a Gas Transporters Safety Case and submit this to the Health and Safety Executive (HSE) and be formally accepted by the HSE.

1.2.1.2. Safe proximity distances

Gas transporters in the UK refer to standards within their Safety Cases. The standards in European countries have their origins within early versions of ASME B31.8 (13). ASME B31.8 is an American standard which gives guidance on material selection, welding, design, installation, testing and operation. The prescriptive standards for the design of new pipelines in the UK and the Europe are IGEM/TD/1 (3) and BS EN 1594 (14) respectively. These publications specify requirements for wall thickness, design factors and building proximity distances. The design factor is based on a function of the wall thickness, pressure diameter and specified minimum yield strength of the pipeline. For example, a 1219 mm, 70 bar pipeline with a design factor, greater than 0.3 and less than 0.72 has a building proximity distance of 112 m. Fearnehough (15) states that the building proximity distances in UK standard (IGEM/TD/1) were based on a radiation level of 32 kW m^{-2}, and whilst this criterion is not a safe level, it reflects a judgement for the low frequency of ruptures and a possibility to escape and find cover for radiation and the fact that the majority of the population is indoor most of the time. Where populations lie inside minimum specified minimum proximity distances, the standards do allow pipeline operators to carry out risk assessments to determine whether the risk of an arrangement is ‘As low as reasonably practicable’ (ALARP). An example of such a possible location is given in Figure 1-2, which depending on the wall thickness of the pipeline has building proximity distance of 15.1, 7.1 or 3 m as given by Figure 6 in IGEM/TD/1 (3).

Figure 1-2 Example of a property located ~15 m from a 26 bar transmission pipeline. Reproduced from Google Maps

Where risk assessments are carried out, consideration will be given to other thermal radiation levels in line with HSE guidance. The HSE guidance uses thermal radiation doses to estimate whether a person becomes a casualty/fatality with more conservative limits to be used when considering sensitive populations e.g. the young or elderly (16). As shielding by buildings can reduce the exposure to thermal radiation, account will need to be taken as to whether the building will also ignite and the probability of someone in the building surviving. The building burning distance (different to the building proximity distance) is used in risk assessments which is defined as the distance to thermal radiation flux causing piloted ignition of wood (12 kW m^{-2}) (17). The methodology used by the HSE, assumes that people within houses which are within exposed to a thermal radiation in excess of 40 kW m^{-2} are assumed to become fatalities or that once a value between 25.6 kW m^{-2} and 14.7 kW m^{-2} is reached at a building, it ignites and the inhabitants escape and attempt to find shelter elsewhere, assuming they don't receive a fatal dose in doing so (18). This underscores that the knowledge of thermal radiation close to any ignited release is required.

1.2.2. America

The American regulations were originally based on American Society of Mechanical Engineers (ASME) B31.8 (13) in 1968. Prior to this, general acceptance standards were used. However, since then, welding, materials and coating techniques have greatly improved. The Pipeline and Hazardous Materials Safety Administration (PHMSA) is responsible for ensuring operators are managing the risks from transmission pipelines. Following a spate of incidents in the US, analysis has been undertaken on these incidents. The result of this analysis is to focus efforts on those pipelines in high consequence areas (19). High consequence areas (HCAs) differ for the transportation of different materials (e.g. gas or liquids), but HCAs for natural gas transmission pipelines focus solely on populated areas. HCAs include where high pressure pipelines have been located in close proximity to occupied buildings.

1.3. Previous Incidents

1.3.1. Selected Ruptures

Incident investigations have been carried out into the causes of pipeline failure and some reports have been made publicly available. Based on available information the following incidents with a rupture failure mode have been reviewed. The incidents selected highlight the level damage to the property and environmental that can be caused as well as injuries and fatalities. Where possible durations of events have also

been included and range from 20 minutes to 125 minutes from the incidents selected below.

Cartwright, August 1976

A 20 inch, 53 bar pipeline was ruptured when a road grader cleared a ditch. The gas release was ignited; killed 6 people, burned two houses and several acres of land (20).

Carlsbad, August 2000

A 46.5 bar, 30 inch natural gas pipeline ruptured at 5:26am, ignited and burned for 55 minutes. Twelve people sleeping under a concrete decked steel bridge were killed with damage caused to a further two suspension bridges supporting pipelines (21).

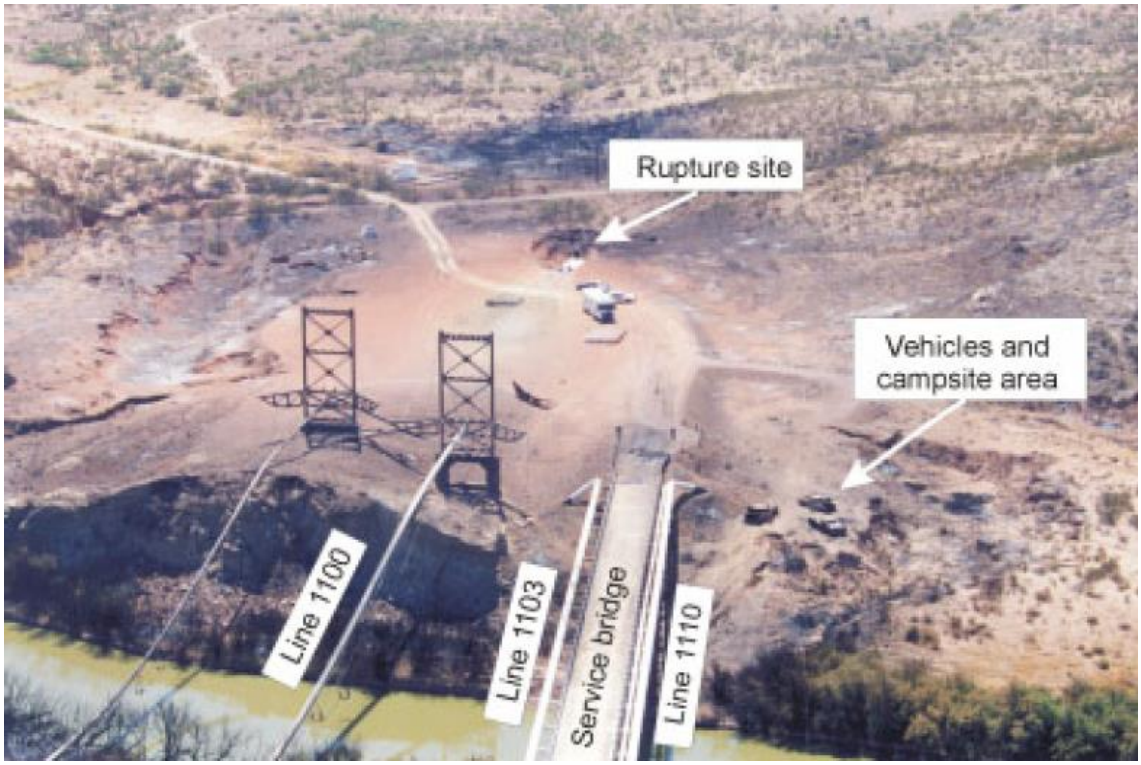

Figure 1-3 Damage caused by rupture of pipeline near Carlsbad. Reproduced from (21)

The three vehicles in Figure 1-3 were destroyed in the incident as well as the vegetation along the riverbanks.

Cleburne, June 2010

A 36 inch diameter pipeline operating at 65.5 bar was struck by an auger (see Figure 1-4). The operator of the auger died in the incident and 6 other workers were burned. The auger was thrown approximately 30 metres from the rupture. The incident began at 2:40pm. The gas pipeline operator closed the upstream valve located 2 miles away at 2:49pm and the downstream valve located 7.8 miles away at 2:55pm. The fire

service arrived at 3:09pm and the area was declared safe to enter at 5:45pm. The area of thermal damage is not stated however, the property and the clean-up cost was quoted as $1,029,000 (22).

Figure 1-4 Natural gas fire after the rupture of pipeline near Cleburne. Reproduced from (22)

San Bruno, September 2010

In September 2010, a 26.6 bar, 30 inch natural gas pipeline ruptured and ignited. The resulting fire killed 8 people and destroyed 38 homes. Thermal damage was also caused to a playground and woodland. Following the release, it took the operating company 95 minutes to stop the flow of gas to the release. The damage spread in a north eastly direction. The wind direction was from the west (23). It should be noted that in this incident, due to the delay in isolating the fire, it is likely once buildings in the vicinity of the rupture site ignited, fires could have spread to cause gas to be released from the gas pipes (distribution network) supplying the properties, which means the damage in Figure 1-5 may not indicate the damage caused only by the ignited release from the ruptured transmission pipeline.

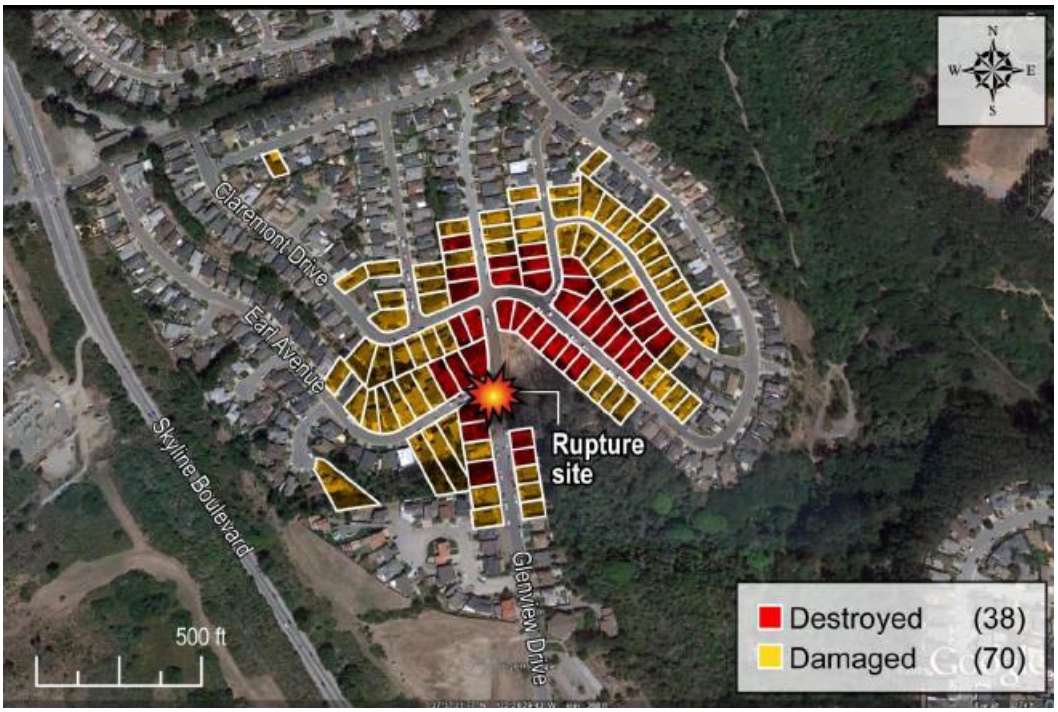

Figure 1-5 Houses damaged or destroyed in San Bruno incident. Reproduced from (23)

Sissonville, December 2012

Just after midday in December 2012, a 20 inch, 64 bar pipeline rupture and ignited (see Figure 1-6). There were no fatalities, although there was fire damage 335 m long and 250 m wide. Three houses were destroyed by the fire (24).

Figure 1-6 Damage following the Sissonville incident. Reproduced from (24)

1.3.2. Ghislenghien, Belgium, July 2004, Incident

In 2004, a 40 inch gas pipeline constructed in 1991 ruptured. Prior to the incident, the pressure was in the pipeline was increased from 60 to 70 bar during a routine operation as the maximum operating pressure of the pipeline was 80 bar. Following the pressure rise, a gas leak was soon reported at 8:45 am. At 9:00 am there was a fire at the location of the leak and at 9:01 am there was a reported explosion. After the rupture, it was estimated that the fire burned for 20 minutes. 24 people were killed by the incident, with 5 of those being fire fighters (25). However, one person who was standing 15 metres from the leak location did survive.

Thermal damage was caused to nearby buildings within a radius of approximately 200 m. Burn damage was observed to be roughly circular with a diameter of approximately 200 m as would be expected (26), but it was also observed that there was limited damage inside a building which was only 130 m from the rupture location (Figure 1-7).

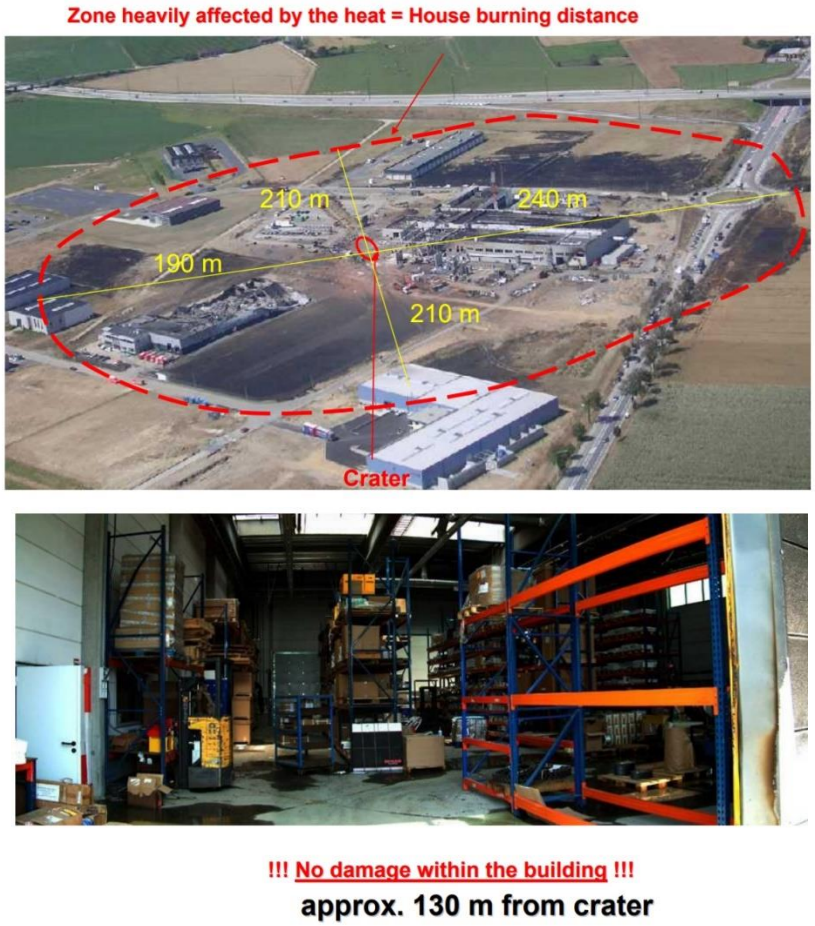

Figure 1-7 Thermal Damage from Belgium Gas Pipeline Incident. Reproduced from (26)

1.4. Aims and Objectives of the Research

Whilst the failure frequency for a rupture event is low, the hazard distances associated with these events range from 3 m to the order of hundreds of metres and previous incidents have led to multiple fatalities. The aim of this research is to measure the intense, short-duration thermal radiation emitted from igniting flammable gas in large scale, underground natural gas pipeline ruptures. The study will explore the implications of such incidents on existing risk assessment methods for subterranean pipelines. Utilising data from large scale tests, a laboratory scale setup will be developed to examine the effects of thermal radiation on various materials during the fireball phase of rupture events. In this controlled environment, the project will investigate how transient thermal radiation impacts different materials, ultimately seeking to determine whether methodical lab scale techniques can be used to develop correlation for 'thermal dose' damage of materials.

A key aspect in determining the acceptability of a pipeline at a particular location is the response of buildings. Currently, the response of the built environment is determined by reference the ignition of wood under a steady-state heat flux, without consideration given to the duration of the exposure.

The methodology for assessing harm to the built environment differs from the approach used to evaluate harm to individuals. The latter is based on a combination of thermal radiation level and the duration of exposure. Though variability is recognized in this approach, an inquiry into the conservatism of employing fixed radiation levels is justified. As such, more cost effective risk reduction strategies might exist.

The research will primarily focus on:

1. Performing large scale gas release experiments to obtain data on the peak values, duration, and thermal radiation flux profiles in fireballs from immediately ignited gas pipeline releases.
2. Developing a laboratory scale setup that can replicate the transient thermal exposure level from these large scale tests.
3. Analysing how materials react to short-term (up to 12 seconds) exposure to variable heat fluxes using the laboratory setup.
4. Exploring the possibility of establishing thermal dose limits (akin to existing limits for human vulnerability) and empirical correlations for materials used in the natural and built environments adjacent to gas pipelines.

CHAPTER 2

LITERATURE REVIEW

2.1. Failure Modes of Natural Gas Transmission Pipeline Ruptures

2.1.1. Introduction

The consequences of high pressure natural gas releases depend on the failure mode. In the UK IGEMTD/2 (17) is the industry standard for carrying out a risk assessment of natural gas transmission pipelines. IGEM/TD/2 defines 3 different broad types of release sizes for transmission pipelines. These are:

- Rupture: the effective diameter of the hole is larger than the pipeline diameter (see Figure 2-1).
- Hole: the effective diameter of the hole is larger than 2 cm and smaller than or equal to the diameter of the pipe (Figure 2-2).
- Pinhole/crack: the effective diameter of the hole is smaller than or equal to 2 cm.

The above can be simplified to unstable defects (those that rupture) and those stable defects (those that don't rupture) (27).

Figure 2-1 Ruptured pipeline. Reproduced from (28)

Figure 2-2 Pipeline with Hole. Reproduced from (29)

An event tree can be used to illustrate the subsequent events for unstable and stable defects as shown in Figure 2-3. The rupture of a gas pipeline can generate missiles, thermal radiation and overpressure hazards which could cause injuries/fatalities, property damage or environmental damage.

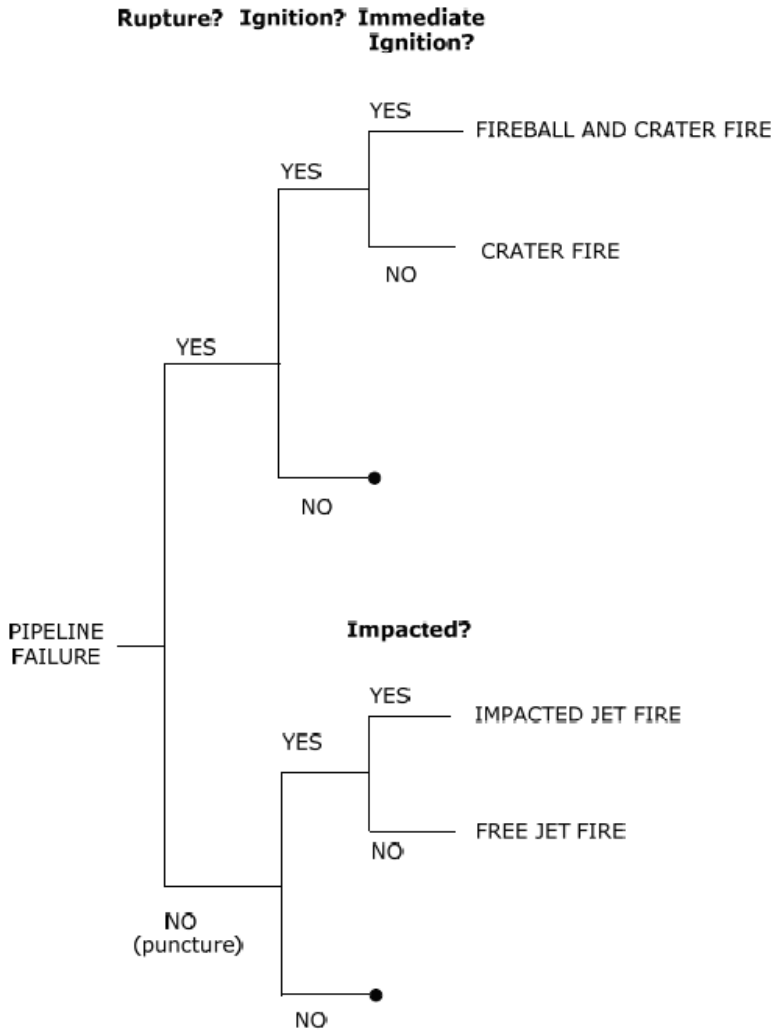

Figure 2-3 Event tree for natural gas pipeline failure. Reproduced from (17)

Whether a stable or unstable defect occurs partly depends on the failure cause. Statistical data on the proportion of different incident causes (e.g. external interference, corrosion, construction defects, ground movement, fatigue) is publicly available (see Figure 2-4) (4).

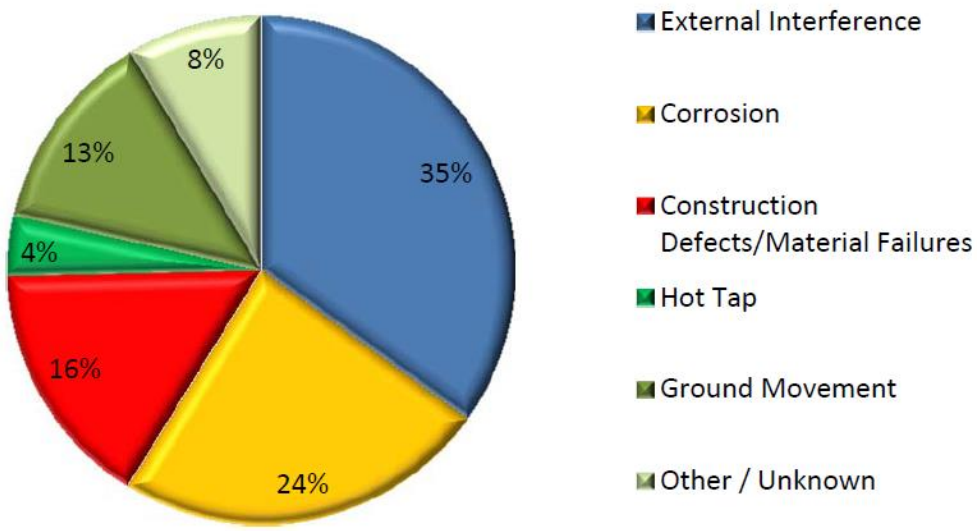

Figure 2-4 Distribution of incidents in the EU (2004-2013). Reproduced from (4)

For pipelines with wall thicknesses greater than 10 mm, the failure frequency rate is dominated by external interference events as the proportion of the overall failure frequency for external interference is greater than corrosion incidents (17). Given information on the failure of such events, coupled with knowledge of the outflow rate, ignition probability and thermal radiation generated, hazard distances can be estimated to estimate the overall risk.

In Section 1 reference was made to fixed thermal radiation hazard distances. Importantly, criteria also include 'Escape distance', Significant Likelihood of Death' (SLOD) and 'Building Burning Distance'.

'Escape Distance' is an indication of the distance from the release at which a dangerous dose would be received. The escape distance is calculated based on a dose of thermal radiation from a fire would be sufficient to result in fatality for the most vulnerable 1% of an average population when outdoors. Conversely, it is a thermal radiation dose from which 99% of an average population would be able to survive. is equivalent to 1060 thermal dose units (TDU) $(kW/m^2)^{4/3}s$ (17).

SLOD is considered to be the distance to which a casualty would occur. SLOD is considered to be equivalent to 50% lethality for normal populations. This is equivalent to 1800 TDU $(kW/m^2)^{4/3}s$ (17).

The 'Building Burning Distance' corresponds to the distance at which typical buildings, such as houses, would catch fire as a result of piloted ignition. These buildings would afford protection to occupants only until ignition occurs (17).

The terms escape distance and SLOD are based on a thermal radiation dose as opposed to a fixed thermal radiation level. Thermal dose is defined and discussed in Section 2.7.1. Typical external interference failure frequency data and their associated hazard distances for a range of pipeline configurations is given in Table 2-1 (17).

Table 2-1 Benchmark data for a range of pipeline cases. Reproduced from (17)

Risk Assessment Parameters	Benchmark Data			
	Case 1	**Case 2**	**Case 3**	**Case 4**
Pipeline diameter (mm)	273	508	762	914
Wall thickness (mm)	6.35	7.9	9.52	11.9
Material grade	X52	X52	X60	X65
Pressure (bar)	38	70	38	70
Area classification (Suburban or Rural)	S	R	R	R
Depth of Cover (m)	1.0	0.9	1.2	1.1
Building proximity distance (m)	16.6	49.2	43.5	76.9
Third party damage rupture failure frequency – estimated (per 1000 km yr)	0.122	0.061	0.010	0.016
Third party damage rupture failure frequency – calculated (per 1000 km yr)	0.053	0.049	0.006	0.014
Building burning distance for ruptures (m) (based on piloted ignition of wood)	69.5	139.1	155.5	221.0
Escape distance for ruptures (1800 tdu) (m)	62.0	147.9	176.7	328.8
Escape distance for ruptures (1% lethality) (m)	83.6	206.5	249.8	452.2

Using the largest failure frequency (0.122 per 1000 km yr) from Table 2-1 for a 273 mm pipeline (Case 1 in Table 2-1) would lead to a rupture event due to external interference approximately once every 8200 years along a 1 km pipeline section. The associated building burning distance for this case is 69.5 m (distance to ~12 kW m^{-2}) and the associated building proximity distance (calculated in accordance with Figure 6 from IGEM/TD/1 (3)) is 16.6 m (distance to ~32 kW m^{-2}).

To validate the above hazard distances, comparison could be made with available experimental data. However, the majority of data for thermal radiation from gas fires is related to jet fires or flares (30). Currently there is limited publicly available data on thermal radiation data from fireballs following a large scale pipeline ruptures with immediate ignition. Two large scale pipeline rupture tests have also been carried out in Canada (31), although only limited data has been reported from these tests. There exist sources of data from liquefied petroleum gas (LPG) boiling liquid expanding vapour explosion (BLEVE) incidents/tests (32), (33), (34). This is discussed further in Section 2.6

2.1.2. Stages of a Natural Gas Transmission Pipeline Release

For a stable defect, Figure 2-3 shows that the consequences of an ignited release would be a jet fire. A jet fire would generate a steady state thermal radiation field which is currently well understood. There are standard tests for assessing whether materials ignite when subjected to steady state tests, for example BS 476-3 (35). In the event of an unstable defect (rupture) of a buried onshore natural gas transmission pipeline, high pressure gas will be instantaneously released leading to the formation of a crater. The initial phase will be highly transient with the formation of a turbulent jet with a mushroom cap. This initial phase can last up to 30 seconds. The gas cloud will increase in height due to the momentum of the release and the entrained air, gradually dispersing to until an almost steady state plume is developed (27).

Whilst missile and overpressure hazards are also generated, experience has shown that from natural gas experiments by Det Norske Veritas (DNV), the hazard distances associated with missile and overpressure are smaller than thermal radiation hazards (36).

The stages of a gas pipeline rupture release can be described in the following stages (see Figure 2-5):

- Outflow from the two pipe ends and generation of gas cloud.
- Formation of crater and flammable gas/air mixture.
- Ignition.
- Thermal radiation (which may be affected by the ambient conditions).

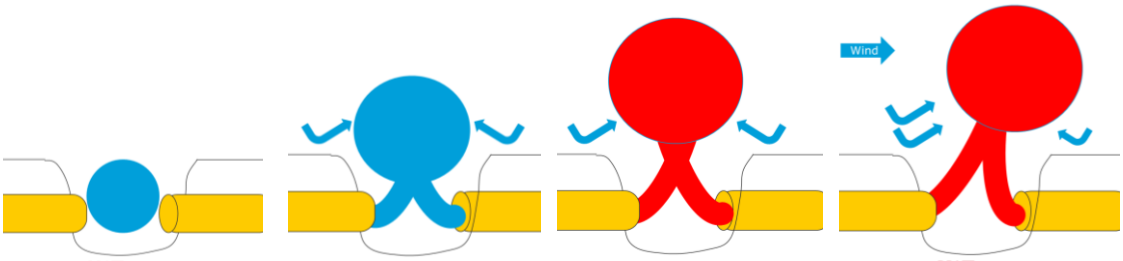

Figure 2-5 Simplified diagram of ignition shortly after a rupture event (red indicates ignited release)

To understand the thermal radiation hazard distance associated with ignited failures of transmission pipelines, the key parameters are:

1. Pressure of the pipeline (known).
2. Diameter of the pipeline (known).
3. Gas outflow in from the pipeline ends.
4. Effect of the crater on the outflow in different atmospheric conditions.
5. Likelihood of ignition.
6. Fire chemistry associated with the ambient conditions.
7. Effect of thermal radiation on people, property, and the environment.

2.2. Gas Outflow

2.2.1. Types of flow

To understand the physics of gas releases (prior to ignition) an understanding of laminar, turbulent, compressible, adiabatic/isothermal and choked flow is required.

2.2.1.1. Laminar and Turbulent Flow

In fluid dynamics, flow regimes are divided into laminar flow and turbulent flow. In laminar flow, the molecules move in an ordered fashion with the same velocity and

hence the path of molecules can be depicted as being seen to move in a layer. Laminar flow generally occurs at lower pressures and properties such as velocity and temperature are constant throughout (see Figure 2-6). The converse is true for turbulent flow. Turbulent flow contains eddies and molecule movement is characterised by turbulent length scales (37).

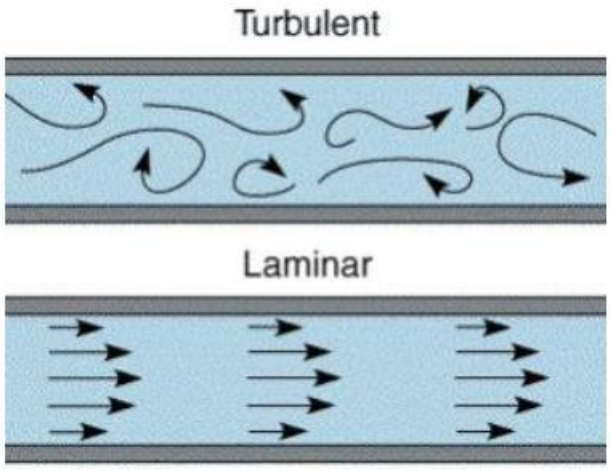

Figure 2-6 Turbulent and Laminar Flow in a Pipe. Reproduced from (38)

The Reynolds number (Re) is a property (developed by Osbourne Reynolds) used to predict the change in flow regime for any fluid:

$$Re = \frac{\rho v l}{\mu} \qquad \textbf{(2-1)}$$

Where:

ρ = density of the fluid (kg m^{-3}).

v = the mean velocity (m s^{-1}).

l = length (m).

μ = the dynamic viscosity of the fluid (Pa·s or kg m^{-1} s^{-1}).

As an important property of describing the flow regime, the point at which fluids change from laminar to turbulent flow is defined by the Reynolds number, with the transition at a value of around 2100. Reynolds numbers greater than 4000 are considered to be fully turbulent. The Reynolds number is a dimensionless number and essentially corresponds to the ratio of inertia forces to viscous forces (39). For gas flow through a pipeline, the velocity of the flow at the pipeline wall is considered to be zero with the thickness of this boundary layer dependent upon the viscosity of the fluid (40).

2.2.1.2. Choked Flow

For any through wall defect in a natural gas transmission pipeline, gas will be released since the pressure in the pipeline is above atmospheric pressure. The release rate will depend upon the pressure and area of the hole up until the flow through the defect becomes 'Choked'. Choked flow occurs where the speed of the gas flow reaches the local speed of sound in the gas as the pressure waves are unable to travel upstream. The Mach number is ratio of the speed of flow to the speed of sound. At subsonic flow the velocity of the gas is less than the local speed of sound. Mach numbers of 0 to 0.8 are considered to be subsonic. At Mach numbers greater than 1, flow is considered to be supersonic. Where the flow approaches the speed of sound, shock waves are created which create discontinuities in the properties of the gas either side of the shock wave (40). In the case of flow through an orifice, a vena contracta forms downstream of the orifice. At this point of minimum flow area must be treated as the equivalent of the throat of a nozzle (37) and therefore the release rate is dependent upon the area of the release. In the case of gas pipeline, the scenario can be considered as one in which there is an infinite reservoir within the pipeline held at a constant pressure (as will be the case until isolation is effected). The point at which flow becomes choked can be determined from (37):

$$\frac{P^*}{P_u} = \left(\frac{2}{\gamma + 1}\right)^{\frac{\gamma}{\gamma - 1}} \qquad \textbf{(2-2)}$$

Where:

γ = heat capacity ratio (dimensionless).

P_u = upstream pressure (bar).

P^* = critical downstream pressure (bar).

For natural gas γ is 1.3, so the pressure at which flow will be choked is ~1.8 bar. Given pressure regimes for transmission pipelines are greater than 15 bar, flow will be

choked for all releases. The mass flow rate for choked flow is as given in equation (2-3) (37):

$$\dot{m} = C_d A \sqrt{\gamma \rho P_u \left(\frac{2}{\gamma+1}\right)^{\frac{\gamma+1}{\gamma-1}}} \quad \textbf{(2-3)}$$

Where:

$\dot{m}$ = mass flow rate (kg s^{-1}).

C_d = coefficient of discharge (dimensionless).

A = discharge area (m^2).

γ = heat capacity ratio (dimensionless).

ρ = gas density (kg m^{-3}).

P_u = pressure upstream of the release (bar).

2.2.2. Experimental Data for Stable Defects (Punctures)

Releases from pipelines can either be a small pinhole leak or a full bore rupture. Figure 2-7 shows experimental data for flowrates of 0.005 kg s^{-1} to 500 kg s^{-1} for a 1 bar, 5 mm hole and 300 bar, 100 mm holes respectively (41).This type of data underlines that outflow from stable defects are well understood.

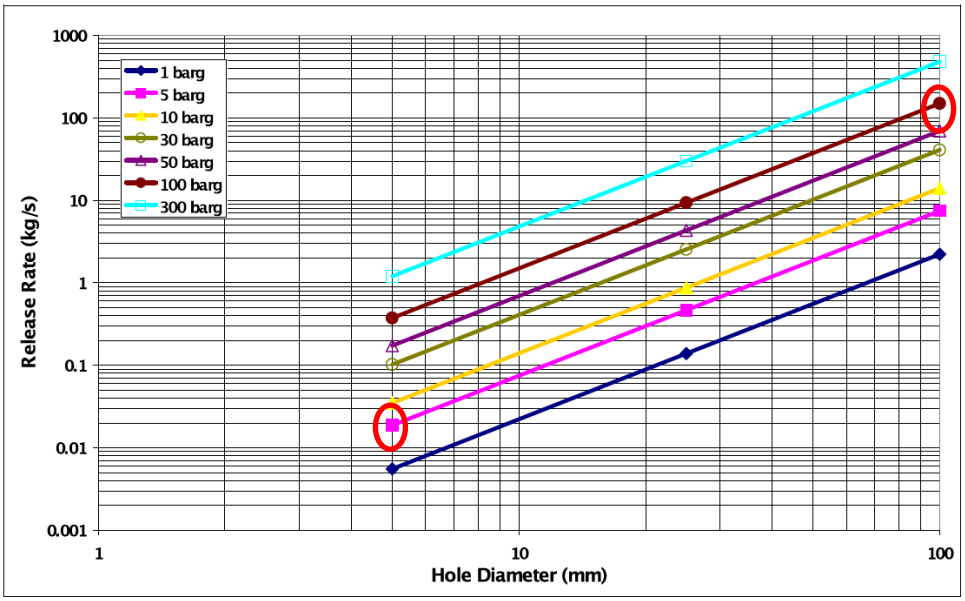

Figure 2-7 Release Rates for Natural Gas at 20°C. Reproduced from (41)

Using Equation (2-3) for 5 mm at 5 bar and for a 100 mm at 100 bar releases gives flow rates of 0.017 kg s^{-1} and 116 kg s^{-1} respectively. This matches with the values given in Figure 2-7 as shown by the highlighted circles.

2.2.3. Modelling Rupture Flows

An equation for mass flow has already been presented in Section 2.2.1.2. However this is based on puncture releases. Flow following a pipeline rupture will vary with time. In the first 30 seconds flow will be highly transient and following this period there will be steady state flow from both ends of the pipeline. This second stage can be modelled like a gas leak from a hole, with steady state flow models as already described (42).

Assuming no change in height (as pipes are laid horizontally), isothermal flow (no temperature change) the following equation (37) can be derived:

$$P_1^2 - P_2^2 = G^2 \frac{RT}{M_w}\left[\frac{4Fl}{D_H} + 2ln\left(\frac{P_1}{P_2}\right)\right] \quad \textbf{(2-4)}$$

P_1 = Upstream pressure (bar)

P_2 = Downstream pressure (bar)

G = gas flow ($m^3\ s^{-1}$)

R = gas constant J mol^{-1} K^{-1}

T = temperature (K)

M_w = molecular weight (g mol^{-1})

F = friction factor (dimensionless)

D_H = hydraulic diameter (m)

l = length (m)

The right-hand term accounts for pressure change due to the acceleration of the gas which occurs due to the change in the density of the gas. The first term accounts for the losses due to friction (37). The solution to this equation can be found by differentiating with respect to P_2:

$$G_{max} = P_2\left(\frac{M_w}{RT}\right)^{\frac{1}{2}} \quad \textbf{(2-5)}$$

For flow from a gas pipeline, the increase in temperature due to friction can be assumed to be offset to thermal losses through the pipeline wall.

Equation (2-5) is for when the specific flow is at a maximum. As stated previously, for the initial stage of gas outflow from a high pressure pipeline, a more complicated approach is required. Tu (43) provides a solution with the mass is conserved, the rate

of change of momentum equals the sum of the forces acting on the fluid (Newton's second law) and the rate of change of energy equals the sum of the rate of heat addition to and the rate of work done on the fluid (First law of thermodynamics).

The equations are complex and are used for many applications in engineering and science. There is no single one solution, however, by making credible assumptions and setting boundary conditions, the partial differential equations can be simplified, and solutions found.

The Pipesafe package is a model that has been developed commercially. This is a one dimensional model, which includes frictional loss effects and uses a simplified form of real gas thermodynamic relationships for the equation of state (44). The friction factor is dependent upon the pipeline diameter and wall roughness is given by:

$$F = \left[\frac{1}{\left(4\log\left(\frac{d}{0.00001524}\right) + 2.28\right)}\right]^2 \qquad \textbf{(2-6)}$$

Heat transfer from the pipeline walls are not included within the model (36). The model has been compared with large scale experimental data and give values within 20% of the flow rate for up to 10 minutes after the initial rupture event (see Figure 2-8). The calculation of the outflow takes into account the influence of failure location and upstream and downstream boundary conditions such that both pipe ends are considered (44).

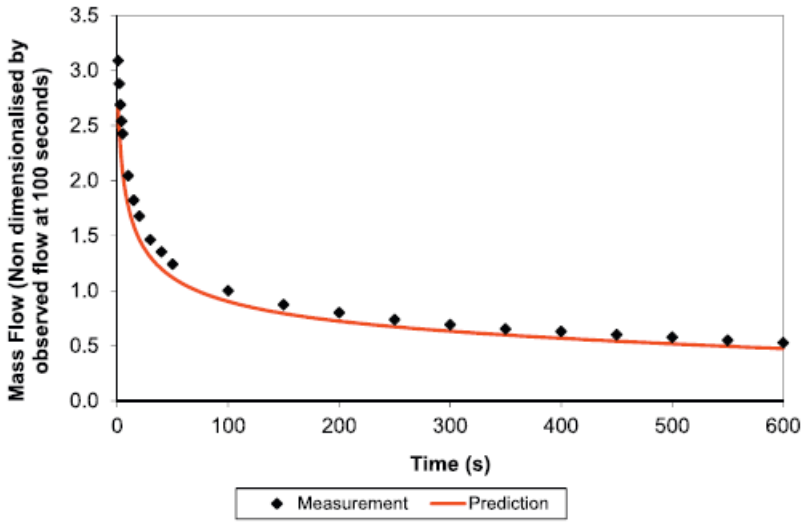

Figure 2-8 Release comparison of predicted flow with large scale experimental data. Data has been normalised to the flow rate at 100 secs as values remain confidential to sponsors of the project. Reproduced from (36)

A model which includes the effects of heat transfer from the walls will provide a better estimate of the temperature of the gas at the exit. Heat transfer from the walls is more critical to determine whether a phase change may occur such that two phase flow that could occur for substances other than natural gas. Models exist to predict the release rate that are based on a set of quasi-linear partial differential equations. The equations are hyperbolic and therefore cannot be solved analytically as there are terms which are unknown or contain functions of dependent and independent variables (45).

Lang, Olorunmaiye and Hanna give other models for the calculation of gas outflow from a ruptured pipeline. The Hanna model assumes that the decompression wave moves in the opposite direction of flow at the speed of sound. This model is used in The Netherlands Organisation (TNO) Yellow Book (46) and the outflow is given by:

$$\dot{m} = \frac{\dot{m}_0}{\left(1 + \frac{m_p}{(t_B \dot{m}_0)}\right)\left[\frac{m_p}{(t_B \dot{m}_0) e^{\left(\frac{-t}{t_B}\right)} + e^{\left(-t t_B \left(\frac{\dot{m}_0}{Q_0}\right)^2\right)}}\right]} \qquad \textbf{(2-7)}$$

Where:

$\dot{m}$ = mass flow rate (kg s^{-1})

m_p = initial mass of gas in pipeline (kg)

t_B = time constant (s)

$\dot{m}_0$ = initial mass flow rate (kg s^{-1})

t = time after rupture (s)

The initial gas flow rate can be calculated using an Equation (2-3), and recalculated at subsequent time intervals for revised values gas in the pipeline.

Equation (2-7) is based on adiabatic flow, uses Equation (2-6) for the friction factor and accounts for the compressibility of the gas. The advantage of the Hanna model as opposed to the PBREAK model is that simple computer programs can be used to predict the flow.

Weaknesses of the Hanna approach are that account is not taken of the heat loss to the walls of the release (so use for two phase flow is not strictly applicable). However, the Hanna model will provide an estimation of the outflow from a ruptured pipeline.

2.2.4. Application of TNO Yellow Book Method to Different Diameter Pipelines

To show the dependence on diameter, calculations for the mass of gas released in the first 20 seconds are given below using the TNO Yellow Book method described in Section 2.2.3. This mass of gas released is required to estimate the thermal radiation in the fireball phase. The results of the calculations are shown in Table 2-2 which used 2500 m for the pipeline length, 70 bar pressure and a density of 60.798 (calculated using the AGA8-92DC method (47)).

Table 2-2 Mass of gas released in 20 seconds for different diameter pipelines at 70 bar

Pipeline Diameter (m)	Mass of gas released in 20 seconds (kg)
0.15	1,139.7
1.2	164,122.7

2.3. Crater formation

2.3.1. Introduction

Natural gas transmission pipelines are predominately buried below ground, therefore gas outflow will be affected by the crater formed following a rupture of a natural gas transmission pipeline. Therefore the consequences for rupture failures depend on physical properties of the crater formed during the initial stages of the release and can affect the definition of the crater (see Figure 2-9). The crater could affect the directional flow of the gas, therefore gas with sufficient momentum would act as a directional jet release that would be less affected by the wind direction, as opposed to gas without sufficient momentum that would disperse as a plume.

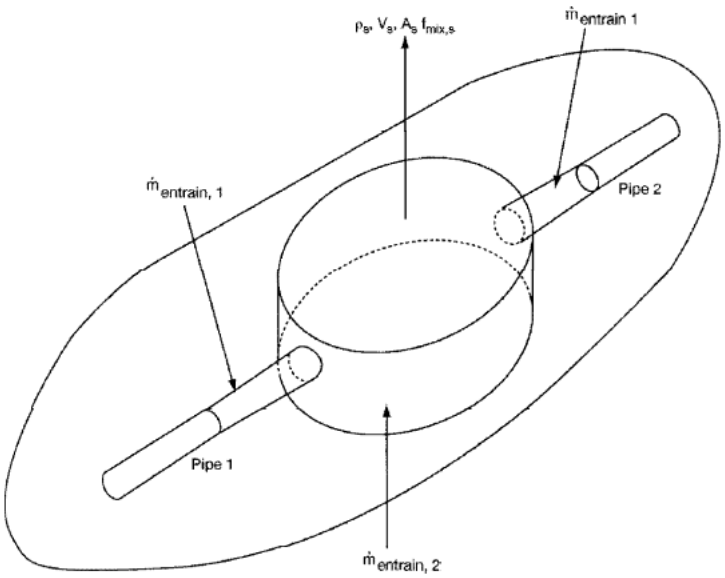

Figure 2-9 Schematic representation of the crater source. Reproduced from (27)

During the rupture of a natural gas transmission pipeline, the energy released leads to the removal of a vast quantity of soil around the pipeline forming a crater which the two open ends sit within. A crater can be defined as a large bowl shape in the ground produced by a fast release of energy such as an explosion or high pressure fracture/release. Simply, the volume and surface area (at ground) level can be deduced by defining the shape of the crater as either semi-hemispherical, circular cone, elliptic cone, rectangular or pyramid. However, the properties dictating the shape formed are complex and involve several parameters. A computer model has been formulated which takes into account the physical properties of air, soil and air/soil interface to determine the craters formed by blast charges (48). Luccioni (48) describes the response of soil and rock when subjected to an explosive release of energy.

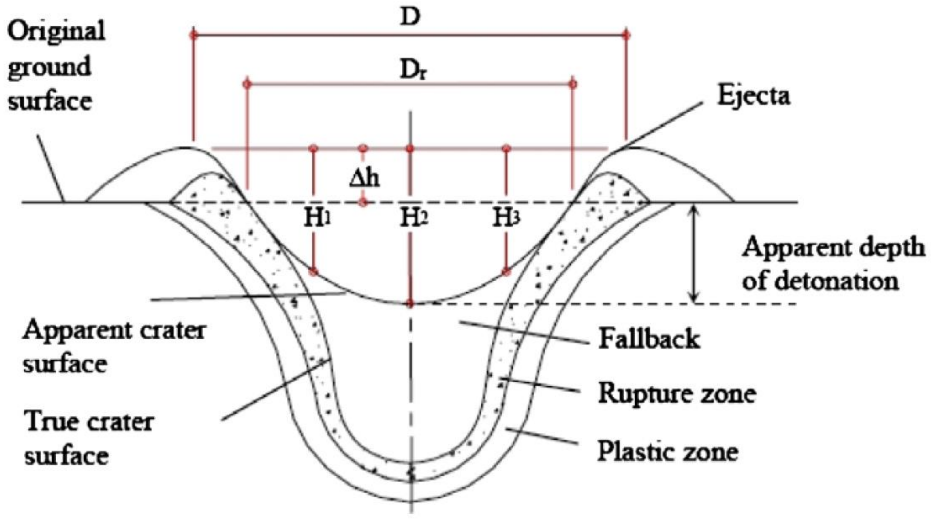

Figure 2-10 Craters formed by explosives. Reproduced from (48)

The conclusions are that explosives must be buried at some depth (of the order a few millimetres) to produce the maximum crater, but after a certain depth the width begins to reduce and that the soil type is not a varying parameter. The case of an explosive differs somewhat to a pipeline rupture. An explosive is concentrated and acts like a point source, whereas in the case of a pipeline rupture the explosive release of energy is spread over a much greater area. Examination of previous incidents shows the length of the crater closely follows the length of the pipeline fracture which is expected as pipeline operators design pipelines such that a fracture is arrested within acceptable lengths (3). Therefore the maximum fracture length is likely to be known. Additionally, the failure mode which leads to the greatest proportion of ruptures, external interference, will lead to defects mainly occurring on the top half of the pipeline. Therefore, the release will be predominately upward and the depth of the crater will follow that of the pipeline depth and the key parameter to define is the crater width and the angle of the crater wall. Figure 2-11 shows the measurements for the San Bruno incident. Figure 2-12 shows crater profiles measured from past incidents along with the position of the top of the pipeline for each incident. The profiles indicate that the pressure, depth and diameter of the pipeline affect the size of the crater. The commonly used crater models for gas pipeline ruptures are empirically based.

Figure 2-11 Crater (width and length) of San Bruno incident. Reproduced from (23)

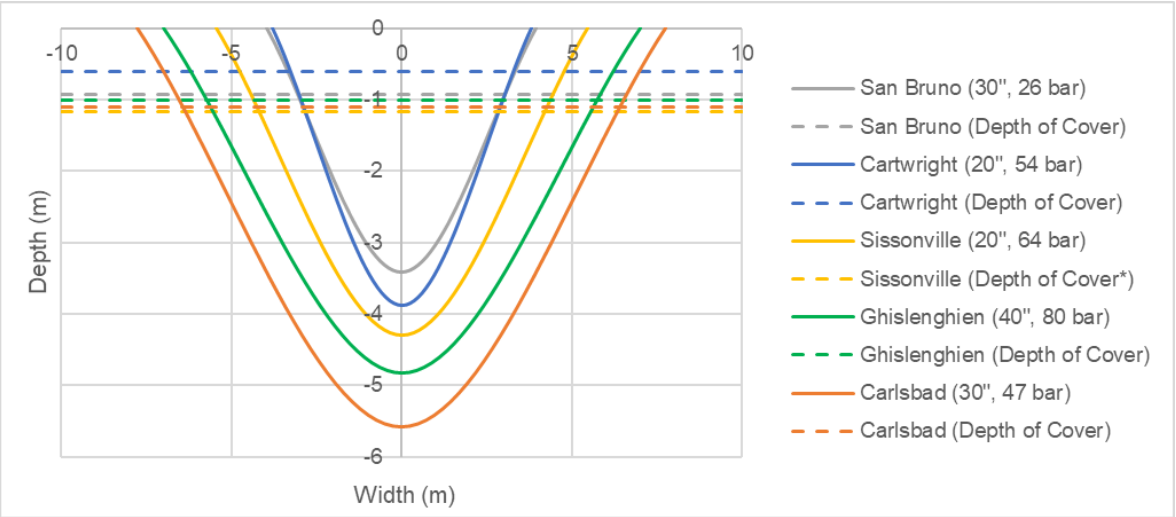

Figure 2-12 Typical cross section (width and depth) profiles from incident data with installed depths of cover

2.3.2. The Gasunie Model

Details of this model are included in NEN 365 (49). This model is empirical based. It was developed by the Hydraulics Laboratory in Delft and is based on a theoretical analysis and on small scale laboratory experiments.

The Gasunie model is based on theory and small scale experimental tests into punctures of a 100 mm pipeline to define equations to predict the depth, width and length of craters. There are two elements to the formation of the crater:

1. the crater formed following the initial explosion
2. the change in the crater due to soil erosion

The model assumes that the shape of the crater is elliptical.

The depth of the crater is based upon the depth of cover over the pipeline plus an additional element which is dependent upon the on the type of soil surrounding the pipeline. The soil type plays a key part in the crater formed, with sandy soil giving rise to the largest sized craters (50). The equations are:

$$D_{cra} = 4.3D + D_c \quad for\ w \leq 0.6 \tag{2-8}$$

$$D_{cra} = \frac{R(w)D}{0.3} + D_c \quad for\ 0.6 < w < 2 \tag{2-9}$$

$$D_{cra} = 2.2D + D_c \quad for\ w \geq 2 \tag{2-10}$$

Where:

w = 0.75, 1.1, 1.75, 2.7 and 5 for very dry sand, sand or dry mixed soil, mixed soil or gravel, humid mixed soil/clay or rock and heavy clay respectively.

R (w) = 0.28 + 0.62(5-w) – 0.07(25-w^2)

D = diameter of pipeline

D_{cra} = depth of the crater

D_c = depth of cover (m)

The crater wall angle is defined as:

$$\alpha = \tan^{-1}(w + 1) \quad \textbf{(2-11)}$$

Where:

α = the angle of the crater wall at the top.

The width of the of the crater is given as:

$$W = 2\sqrt{\frac{D(D_c + \frac{D}{2})}{u_{kr}}\sqrt{\frac{\gamma P}{3\rho(\gamma^2 - 1)}} - (D_c + \frac{D}{2})^2} \quad \textbf{(2-12)}$$

Where:

u_{kr} = 2.54 m s^{-1} and has been determined empirically in (50)

ρ = density of the soil (kg m^{-3}).

γ = heat capacity ratio (1.3 for natural gas)

P = pressure in the pipeline (Pa)

2.3.3. The Pipesafe Crater Model

There is a crater model within the Pipesafe package which includes other consequence models that allows quantitative risk assessments (QRAs) to be undertaken for high pressure gas pipelines (44). The Pipesafe crater model is reportedly a further development of the Gasunie model. The crater model is used to estimate mass flow out of the crater. In addition, the model also includes an adjustment to the radiation emitted due to for presence of soil within the plume.

2.3.4. Simpler Models (SM)

There are simple empirical models, based largely on observations from incidents. One of the main simplifications is that the crater is circular rather than oblong.

SM: Crater Angle

Crater angle is defined by the depth and width of the crater. It can be visualised that the gas emitted from the open pipeline upward with a spray angle given by the crater angle. Given the scatter of data on crater angle, one approach is to apply a uniform crater angle. HSE's model (51) calculated a crater angle of 71° from analysis of past incidents. Assuming a cone shape crater and knowledge of the depth of cover and diameter of the pipeline, the diameter of the cone (and hence width, length and area) can be found.

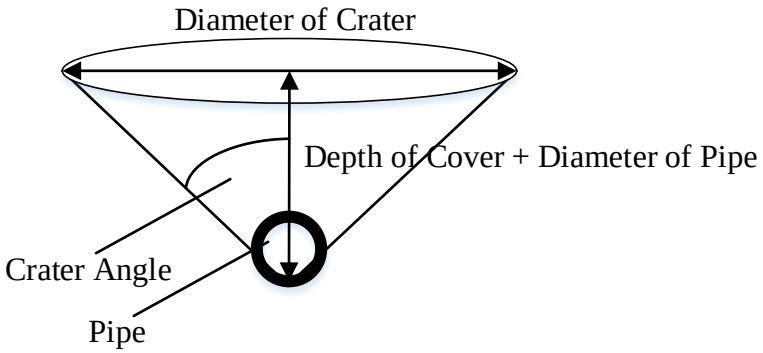

Figure 2-13 Circular crater assuming cone shape geometry

2.3.5. Application of the Gasunie Model to Different Diameter Pipelines

Using the Gasunie method described in Section 2.3.2, calculations have been carried out for different diameter pipelines based on a pressure of 70 bar (70 x 10^5 Pa), depth of cover (D_c) of 0.9 m, soil type of be mixed soil or gravel (w = 1.75) and density of the soil is 2050 kg m^{-3}.

Table 2-3 Crater sizes for different diameter pipelines at 70 bar

Pipeline Diameter (m)	Crater Width (m)	Crater Depth (m)	Wall angle (°)
0.15	2.6	1.3	70
1.2	11.0	3.9	70

As indicated at the start of Section 2.3, the crater affects the gas release from a rupture release due to the impact on the air mass entrainment into the release as described by Cleaver (27). As such larger crater depths or smaller wall angle lead to greater mass entrainment rates.

2.4. Ignition

Ignition sources may contain energy that is capable of igniting certain flammable materials when mixed with air. Ignition sources include heat, electric spark, electrostatics (52). Minimum ignition energies for a range of flammable gases have been experimentally determined. Methane (the main constituent of natural gas) has a higher minimum ignition energy than other alkanes, but in general ignition energies are of the order 0.3 mJ (53).

For a natural gas transmission pipeline release to be ignited, the mixture of gas and air needs to be within the flammable range. In the case of a gas pipeline leak near the crater exit, the mixture is likely to be fuel-rich. Additionally, the presence of soil can further impede ignition, making the mixture less likely to ignite. However, the gas release will be turbulent, which will cause air to be entrained (see Figure 2-10). Ignition of the mixture will lead to combustion of large volumes of gas. In 1985, estimates of ignition probabilities were based on experience from worldwide incidents and were assumed to be 0.5 for ruptures and 0.1 for stable defects (15).

Other more recent sources of ignition probabilities are provided by Centre for Chemical Process Safety (CCPS) and are given in Table 2-4.

Table 2-4 Ignition probabilities for gas pipeline failures. Reproduced from (54)

Data Source	Release type	Ignition probability (0-1)
Worldwide	Leaks	0.1
	Ruptures	0.5
US	Ruptures	0.26
	All sizes	0.16
Europe	Pinholes/cracks	0.02
	Holes	0.03
	Ruptures < 16 inches	0.05
	Ruptures > 16 inches	0.35
	All sizes	0.03

The above data shows a variation in values which reflects the wide range of sources, for example offshore/onshore and different size releases (53).

Models for ignition of vapour clouds are based on the area over which the release occurs. These take into account variables such as the release rate, the number of release sources within the likely cloud area, the time of the release (day or night) and whether the release is in a rural or urban area (55). In the case of a gas pipeline, third party interference is the most common cause of pipeline ruptures (see Section 2.1.1). Nearby ignition sources, such as an excavator, are often present during such unintentional pipeline strikes, potentially serving as immediate ignition points.

As more incidents have occurred, more data has been analysed for the prediction of ignition of gas pipeline releases. Analysis of incident data published in 2008 shows ignition probability correlates with product of pressure and diameter squared (56).

The correlation for ignition probability is given as:

$$Ignition\ Probabilty = 0.0555 + 0.0137.P.D^2; for\ 0 \leq PD^2 \leq 57$$

(2-13)

$$Ignition\ Probabilty = 0.8; for\ PD^2 > 57$$

Where:

P = pressure in the pipeline (bar)

D = diameter of the pipeline (m)

Table 2-5 Igntion probabitlites for different diameter pipelines at 70 bar

Pipeline Diameter (m)	Ignition Probability (0-1)
0.15	0.07
1.2	0.8

No distinction is made between delayed or immediate ignition in equations shown in (2-13). The calculations illustrate that ignition from larger diameter pipelines are more likely to ignite and hence there is an increase likelihood of a fireball for larger diameter pipelines.

2.5. Overpressure

Overpressure can also be generated following ignition of highly turbulent mixtures of gas and air that occur after pipeline rupture. The criteria for assessing the vulnerability of people and the environment are defined in various sources (57), (58). For buildings, values below 30 mbar are cited as being ‘insufficient to cause structural damage or significant window glass hazards’. Research (59) has been carried out for natural gas which has found at 20 m from the rupture location a peak value of ~30 mbar was obtained (see Figure 2-14, black line). Although distances may be greater for larger diameter pipelines, the equivalent thermal radiation flux at the same distance tends to be the predominant hazard. In case for pipeline used for Figure 2-14, the thermal radiation flux is 30-40 kW m^{-2} at 20 m. At this flux, fatalities would occur, and buildings would ignite.

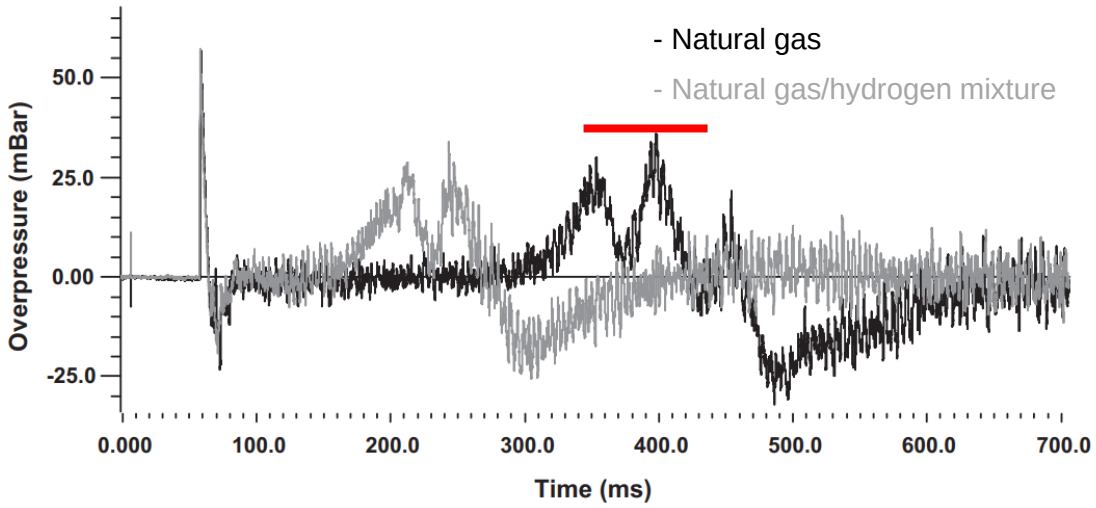

Figure 2-14 Overpressure from a ruptured 150 mm natural gas pipeline (black) compared with a 20% blend of hydrgen and natural gas (59)

A blend of natural gas and hydrogen is referred to in Figure 2-14 and in the introduction, hydrogen was referred to as a potential replacement for natural gas. Initial information indicates for a 100% hydrogen pipeline, delayed ignition of a ruptured pipeline could lead to higher overpressures that need to be accounted for within any risk assessment (60). This scope of this study does not include hydrogen but this is an area where further research is needed.

2.6. Thermal Radiation

Past incidents demonstrate that it is thermal radiation which causes fatalities as opposed to other hazards such as overpressure or missile fragments. For example, the incident in Belgium which included twenty four fatalities (See 1.3.2). Five were fire fighters who were in the process of implementing exclusion zones for the initial leak. These firefighters were on site at the time of the rupture and ignition of the fireball, highlighting the lethal potential of thermal radiation in such events.

2.6.1. Introduction

All objects with a temperature greater than absolute zero emit thermal radiation. The thermal movement of charged particles in matter generate electromagnetic waves which travel at the speed of light.

The relationship between the speed, wavelength and frequency of electromagnetic waves is given as:

$$f = \frac{c}{\lambda} \quad \textbf{(2-14)}$$

Where:

f = frequency (Hz).

c = the speed of light in a vacuum (2.998 x 10^8 m s^{-1}).

λ = wavelength (m).

Electromagnetic waves can be characterised by their wavelength with regions such as gamma rays, x-rays, ultraviolet, infrared, microwave, radio waves and the visible spectrum. The wavelength of the visible spectrum ranges from 400 nm to 700 nm. The electromagnetic waves of thermal radiation lie in the infrared region and have wavelengths of approximately 0.3 to 50 μm, depending on the objects source temperature (see Figure 2-15). In Figure 2-15, the red curve shows the average grey body curve for the liquefied natural gas (LNG) fire (mean emissivity of 0.92) that emit radiation at all wavelengths and the black line shows the actual wavelength emitted of the actual radiation.

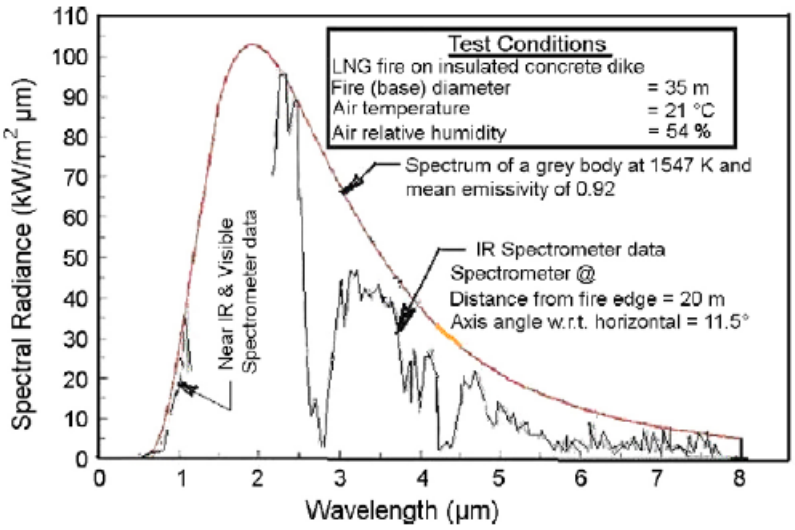

Figure 2-15 Wavelength of radiation from an LNG fire. Reproduced from (61)

It is the by-products of combustion i.e. carbon dioxide, water vapour and carbon particles (i.e. soot) that emit thermal radiation (62). A flame in which the radiation is emitted solely from the gaseous constituents is termed non-luminous and one in which there is soot is termed luminous. In the case of an immediate ignition of high pressure natural gas pipeline leak, a fuel rich mixture will be burnt with limited production of soot.

The strength of the thermal radiation is defined by the emissive power. The total emissive power at which radiation is emitted over all wavelengths may be determined by Stefan-Boltzmann Law:

$$\ddot{q} = \sigma T^4 \quad \textbf{(2-15)}$$

Where:

$\ddot{q}$ = Thermal radiation flux (kW m^{-2}).

σ = Stefan-Boltzmann constant, 5.67 x 10^{-11} kW m^{-2} K^{-4}.

T = source temperature (K).

The Stefan-Boltzmann Law strictly applies only for black bodies. Since the gaseous constituents from which the radiation is emitted is not a black body, non-black body/grey body radiation which includes the emissivity of the surface of the constituents must be considered as shown in Equation (2-16). The emissivity of a surface is defined as its effectiveness in emitting energy as thermal radiation.

$$\ddot{q} = \sigma \varepsilon T^4 \quad \textbf{(2-16)}$$

Where:

ϵ = emissivity.

The calculation for emissivity for a body of hot gas is calculated using a standard method which is a function of the partial pressure and the mean path length. The concept of path length was introduced by Hottel and Sarofim (63) and accounts the geometry of a given scenario. As natural gas fires will not contain limited soot, mean path lengths are relatively short.

Atmospheric transmissivity affects thermal radiation at a receiver, reducing it compared to the source (32). This is due to absorption, related to the number of atmospheric molecules, and scattering, influenced mainly by carbon dioxide and water vapour.

The incident heat flux is therefore a function of flame temperature, emissivity, distance to receiver and view factor. Based on point source models, thermal radiation decreases approximately by the square of the distance from the radiating source; meaning that a receiving object situated 2 m from the source would receive ¼ of the radiation than if it were sited 1 m from the source.

In the case of a pipeline rupture which is immediately ignited, as described in the gas outflow section, there will be a varying thermal radiation level which can be split into two distinct phases; a fireball followed by a jet/crater fire.

2.6.1.1. Fireball Description

For a typical fireball following a pipeline rupture, tonnes of flammable material can ejected over a time frame of 10-30 seconds. In describing a fireball there are three phases; growth, steady burning and burnout. Lee's (38) provides a duration and flame temperatures of each of these phases:

1. Growth - there are 2 phases lasting approximately a second each. In the first phase the fireball grows to half its final value and has a flame temperature of approximately 1600 K based on the presence of yellow-white flames. In the second phase of growth the flame temperature is approximately 1400-1500 K based on the presence of orange/light red flames with 10% of the surface being darker and sooty.
2. Steady burning - The is estimated to last 10 seconds. The flame is spherical and begins to lift into the characteristic mushroom shape. The flame temperature is estimated to be 1400–1500 K.
3. Burnout - The final phase is estimated to last approximately 5 seconds.

Assuming black body radiation (i.e. $\epsilon = 1$), these temperatures (1373 – 1573 K) give source thermal fluxes from 201 kW m^{-2} to 347 kW m^{-2}. Johnson and Prichard's (33) large scale tests quote values of 250-350 kW m^{-2}.

2.6.1.2. Jet/Crater fires

The second phase, a jet/crater fire, will typically begin approximately 30 seconds after the initial rupture. As already described for the gas flow, the same applies for the thermal radiation. Essentially, once a puncture pinhole release is ignited, the jet/crater fire duration will depend upon how quickly and how near to the fracture the pipeline can be isolated. Experimental data on unconfined jet fires for releases greater than 30 kg s^{-1} give rise to fires 65 metres in length and with surface heat fluxes of 350 kW m^{-2} (30). Depending on the duration, fires from jets or craters can also make a substantial contribution to the 'thermal dose' delivered to the surroundings.

2.6.2. Thermal Radiation Data from Fireball Experiments

There are commercial models available that have been validated against experimental data, for example PHAST (64). This software has been used for a 736.6 mm, 32 bar natural gas pipeline with the hazard distance calculated to be 306 m, based on a hazard criterion of 1000 TDU (65). Comparison of the predictions by PHAST against

experimental data is given by Witlox (66). The PHAST model implements the dynamic Martinsen and Marx (67) model for the fireball phase. The predictions by PHAST for a fireball have been compared with butane and propane releases as shown in Figure 2-16 and in this context, the dose is determined by the product of thermal radiation and the duration of exposure, without the use of an exponent.

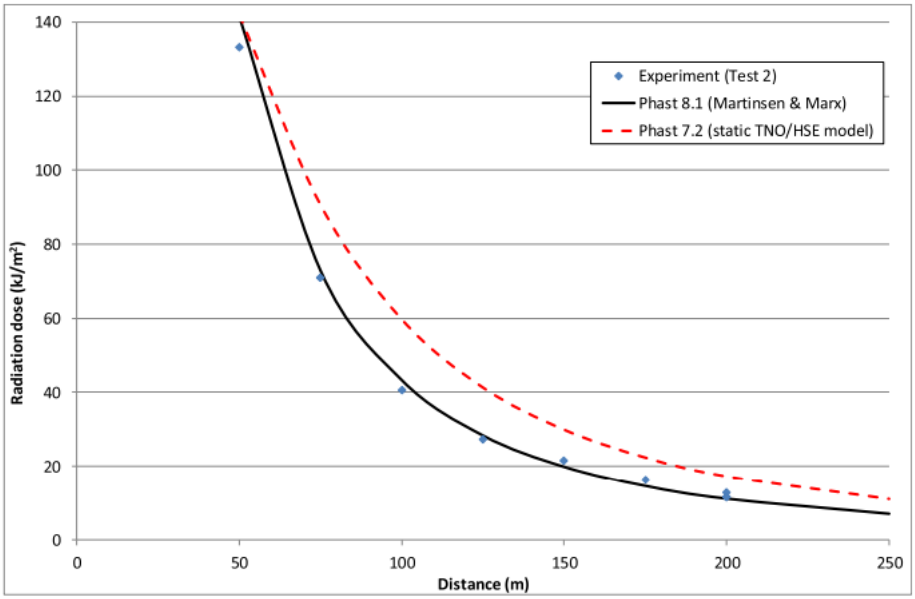

Figure 2-16 Radiation dose predictions for butane fireball experiment. Reproduced from (66)

For an ignited natural gas/methane pipeline release, one large scale experiment has been carried out in China. In this experiment 800 m^3 of LNG (1 m^3 of LNG = 600 m^3 of natural gas) was held within a 430 m test pipeline. The 56 inch (1.422 m) diameter, material grade X80 pipeline was filled to a pressure of 200 bar (20 MPa). The experimental results are shown in Figure 2-17. The peak thermal radiation in the near field (50 m) was 74.1 kW m^{-2}. The diameter of the fireball was nearly 400 m and lasted between 25 and 40 seconds. The conclusions of the work are that all people within 190 m of the pipeline are assumed to become fatalities (68), i.e. those exposed to a thermal radiation level of 30-36 kW m^{-2}.

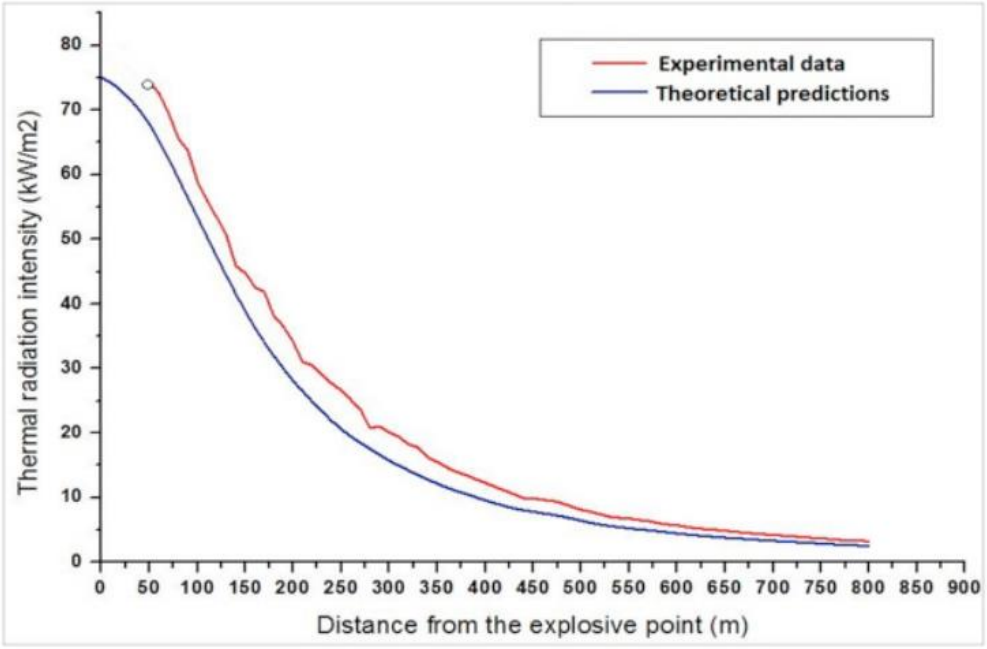

Figure 2-17 Experimental data rom a 200 bar LNG Pipeline Rupture. Reproduced from (68)

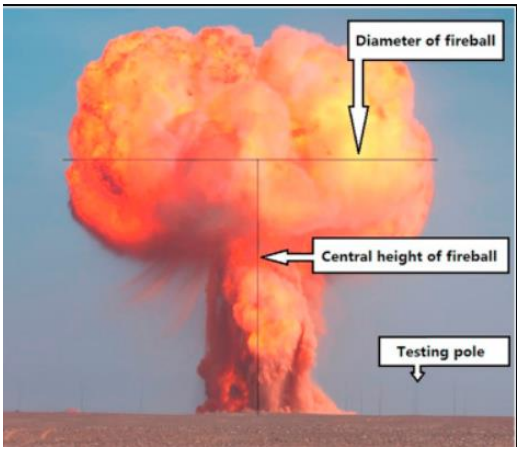

Figure 2-18 Experimental data from a 200 bar LNG Pipeline Rupture. Reproduced from (68)

A further account of thermal radiation data from a pipeline release involves comparing the Pipesafe model predictions with experimental data conducted at a one-sixth scale of a natural gas pipeline, see Figure 2-19 (36).

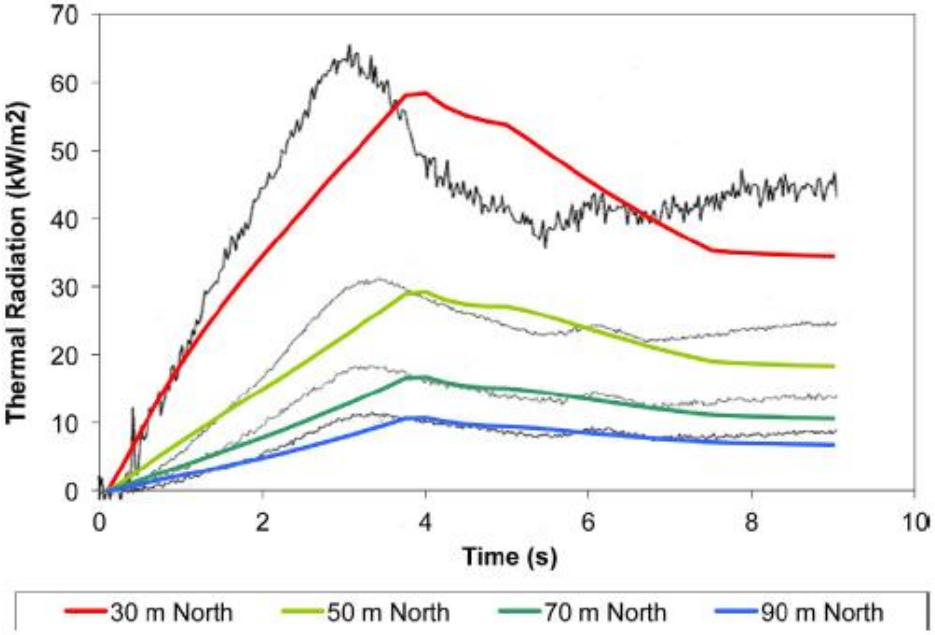

Figure 2-19 Thermal Radiation from a gas pipeline release 1/6 scale (Pressure and diameter not stated). The solid coloured lines are predictions by the model and the black lines are the observations taken from the experiment. Reproduced from (36)

Figure 2-19 shows good agreement between predicted (coloured lines) and measured (black lines) at different distances from the epicentre. A peak radiation level of approximately 60 kW m^{-2} at a distance of 30 m and 30 kW m^{-2} at a distance of 50 m from the source. The measured radiation decreases with distance from the source with the peak occurring approximately 4 seconds after the rupture indicating the timescale for the peak thermal radiation from the fireball phase.

Additional experimental data, also conducted at a 1/6 scale, has been published (59). In these experiments the pressure of the pipeline was carried out with a mixture of natural gas and hydrogen (Test 1) and natural gas (Test 2). The arrangements for both tests were 70 bar, 150 mm diameter pipeline within an uncovered crater, 3.3 m long, 1.7 m wide and 0.5 m deep. In test 2 of the natural gas experiment, where the flame was notably tilted, a peak thermal radiation level of around 55 kW m^{-2} (see Figure 2-20) was observed at a distance of 40 meters from the rupture location. At a distance of 144 mm a peak thermal radiation level of between 7-8 kW m^{-2} (see Figure 2-21) was reached.

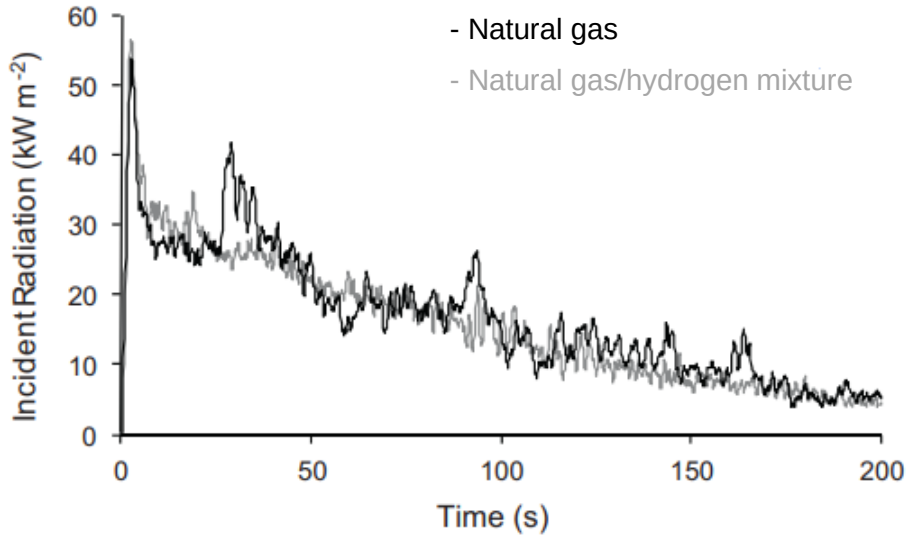

Figure 2-20 Thermal Radiation from a gas pipeline release 1/6 scale (70 bar and 150 mm diamater) – Thermal radiation at a distance of 40 m. Reproduced from (59)

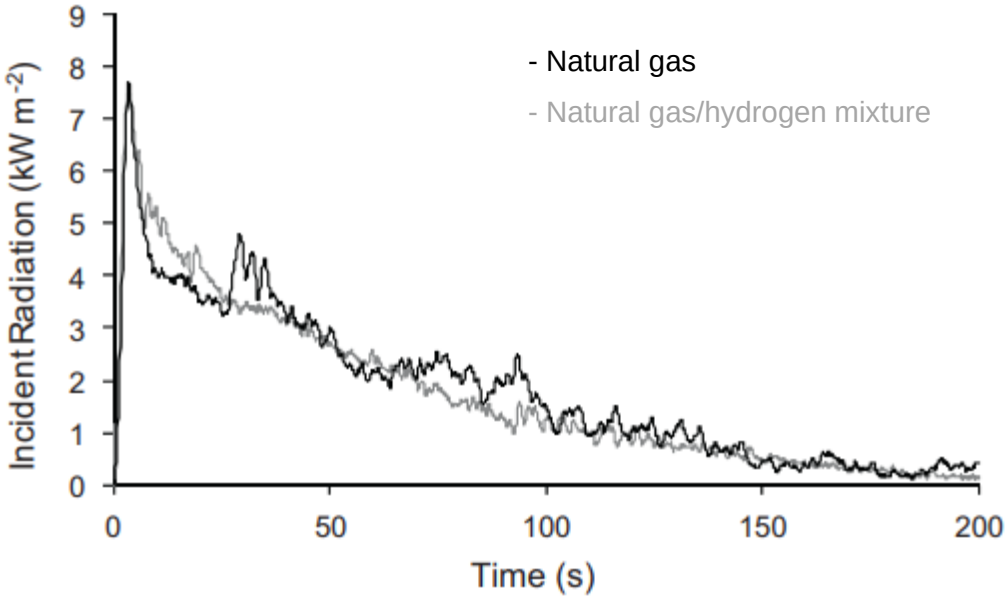

Figure 2-21 Thermal Radiation from a gas pipeline release 1/6 scale (70 bar and 150 mm diamater) – Thermal radiation at a distance of 144 m. Reproduced from (59)

In 1992, full-scale tests were carried out in Canada. During this test, measurements of the incident thermal radiation from both the fireball and the ensuing crater/jet fire were obtained. The tests were co-ordinate by a group of pipeline operators and only limited details of the tests have been made publicly available (31). The two tests involved the deliberate rupture of a 36 inch (914 mm) pipeline at 60 bar. The pipeline was 76 km long. Of the two tests conducted, the first was with a pipeline covered with soil and the

second with the pipeline in a pre formed crater. There were calm conditions for test 1 and a wind of approximately 6 m s^{-1} in test 2. In the tests 240 tonnes of natural gas were released in the first 60 seconds which reduced to 1.5 tonnes per second after 5 minutes in test 1 and 1.8 tonnes per second after 4 minutes and 30 seconds in test 2. In test 1 vegetation was burnt up to 250 m from the test point whereas in the second test this distance was up to 400 m. In the second test, the wind was reported to have had an effect on the vertical fire after 40 seconds. This tilt was noticed to straighten shortly after a valve was closed such that the dominant flow from one pipeline end was directed into the wind (31).

Additional fireball data encompasses BLEVE (Boiling Liquid Expanding Vapor Explosion) tests, usually conducted using either butane or propane. These tests can provide an indication of the expected thermal radiation levels during the fireball stage of a pipeline rupture, aligning with the approach used for validating the PHAST model. Thermal radiation data from a 1.7 tonne BLEVE test is shown in Table 2-6 (69).

Table 2-6 BLEVE Radiation levels. Reproduced from (69)

Distance (m)	Maximum Radiation (kW m^{-2})	
	Upwind	**Crosswind**
50	36.72	47.78
75	20.03	28.13
100	14.03	18.12
125	9.70	11.96
150	8.03	9.51
200	4.38	5.05

Figure 2-22 Fireball produced following rupture of 1.7 tonne LPG vessel. Reproduced from (69)

The Health and Safety Laboratory (HSL) conducted BLEVE experiments and determined that the radiation field is influenced by the wind direction and the quantity of fuel. In crosswind locations, the maximum observed surface emissive power ranged from 278 to 413 kW m^{-2} (69). Other BLEVE models include those from Liho, Shield and Deaves (70).

2.6.3. Models for Prediction of Thermal Radiation Exposure

To predict the thermal radiation received outside the flame envelope, point source, solid flame and empirical models can be used.

Point source models assume all heat flux emanates from a single point whereas the solid flame model assumes the heat flux is emitted from the surface of the flame. For point source models the radiant heat flux received by a receiver:

$$\ddot{q} = \dot{Q}/(4\pi r^2) \quad \textbf{(2-17)}$$

Where:

$\ddot{q}$ = radiant heat flux (kW m^{-2})

r = distance to receiver (m)

$\dot{Q}$ = heat release rate (kW)

Point source models are simple to use and can be used where the receiver is at large distances from the flame.

A solid flame model can be modelled as:

$$\ddot{q} = \tau V_f S \quad \textbf{(2-18)}$$

Where

V_f = the view factor (-)

τ = atmospheric transmissivity (-)

S = average surface emissive power (kW m^{-2}).

The solid flame model is dependent on the flame geometry, the thermal characteristics of the flame and the atmospheric transmissivity. Fire models currently use time averaged flame shapes to estimate the geometries involved (71). The proposed models assume shape of the fireball is either spherical or hemispherical.

A hemispherical shape assumption will yield larger values than a spherical one for the same mass modelled, although it should be noted that as the thermal radiation decreases approximately by the square of the distance from the radiating source, this difference will only likely noticeable in the near field. The solid flame model can be used along with the heat of combustion, radiative fraction of heat of combustion, an estimation of the surface emissive power and an appropriate view factor to estimate thermal hazard distances for given criteria (16).

Empirical fireball durations and diameters take the form of:

$$t_d = \mathrm{a} m_f^b \quad \textbf{(2-19)}$$

$$D_f = \mathrm{c} m_f^d \quad \textbf{(2-20)}$$

Where:

m_f = the mass of material released (kg)

a, b, c and d = constants (-).

Values of ‘a’ range from 5.25 to 6.48 and ‘b’ is most commonly 0.333. Values of ‘c’ range from 0.38 to 5.25 and ‘d’ is commonly 0.333, but values as low as 0.167 have been quoted (72)- (73).

Roberts (32) gives empirical correlations for durations and the thermal radiation received at a distance from the source. The correlation is based on a spherical flame and give the following formula for the radius of flame:

$$R_f = 29 m_f^{\frac{1}{3}} \quad \textbf{(2-21)}$$

Where:

m_f = mass of fuel (based on liquified petroleum gas) in the fireball (kg).

The thermal radiation received at a distance is given as:

$$\ddot{q} = \dot{Q}(fireball)V_f\tau \quad \textbf{(2-22)}$$

Where:

$\dot{Q}$(fireball) = $235P_0^{0.39}$

P_0 = 14.5 bar for propane and 5.2 bar for butane

$$V_f = \frac{R^2 x_f}{\left(R^2 + x_f^2\right)^{\frac{3}{2}}}$$

τ =1 - 0.0565.lnx_f

x_f = distance from the fireball (m)

Other view factor relationships have been derived by Vilchez et al for more complicated cases where obstacles lie partially between the area at harm and the fireball (74).

Wang (68) uses a method of the same form as described in Oil and gas producers (OGP) guidance (41). The method allows the peak thermal radiation to be calculated at a given distance using the equations for the maximum diameter, duration and height of the fireball.

$$D_{f,max} = 6.48m_f^{0.325} \quad \textbf{(2-23)}$$

$$H = 4.35m_f^{0.333} \quad \textbf{(2-24)}$$

$$t_d = 2.60m_f^{0.167} \quad \textbf{(2-25)}$$

Where:

$D_{f,max}$ = maximum diameter of the fireball (m)

m_f = mass of fuel involved

H (m) = height of the fireball from ground level

t_d (s) = duration of the fireball (s)

The distance (X_f) from the fireball to the receiver is:

$$X_f = \sqrt{l_f^2 + H^2} \quad \textbf{(2-26)}$$

Where:

l_f = distance to the point on the ground beneath the fireball.

The view factor (V_f), transmissivity (τ) and surface emissive power (S) are given by:

$$V_f = \left(\frac{D_{f,max}}{2X}\right)^2 \quad \textbf{(2-27)}$$

$$\tau = 2.02\left[RP_w\left(X - \frac{D_{max}}{2}\right)\right]^{-0.09} \quad \textbf{(2-28)}$$

$$S = \frac{\Delta H M F_r}{\pi D_{max}^2 t_d} \quad \textbf{(2-29)}$$

where:

R = relative humidity

P_w = water saturation pressure (1312 Pa)

ΔH = heat of combustion (52 MJ kg^{-1}).

The fraction of heat radiated (F_r) is given by Wang as:

$$F_r = 0.27P^{0.32} \quad \textbf{(2-30)}$$

Where:

P = the pipeline pressure (MPa).

The rational of this relationship is unclear as the value calculated by Wang was 0.7 as values of 0.14 to 0.35 have been quoted (75) and Lees' (32) states extrapolation up to values as high as 6 MPa. The radiation ($\dot{q}$) received by an observer at distance is:

$$\dot{q} = V_f \tau S \quad \textbf{(2-31)}$$

As has been noted in Section 2.5.2, the thermal radiation flux emitted at the source will vary with time. To take account of the differences in thermal radiation emitted (and received) at a given point the concept of thermal dose unit is used to take account of change in thermal radiation and the time of exposure. Therefore using Equation (2-22), a dose can be calculated for a receiver (76). A limitation of a static models is that account is not taken of the transient variation in the source thermal radiation as shown in experimental releases (so is conservative). By taking account of the change in thermal radiation over time, a more accurate representation of the dose can be obtained (see Figure 2-23).

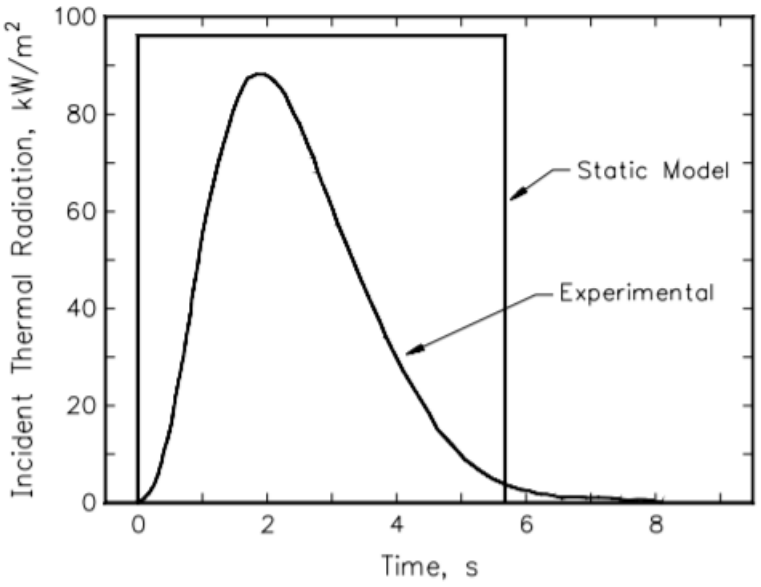

Figure 2-23 Static model compared with experimental data. Reproduced from (67)

To account for this, Marx and Martinsen (67) developed a dynamic model (used in PHAST) using the empirical equations for the fireball diameter and duration.

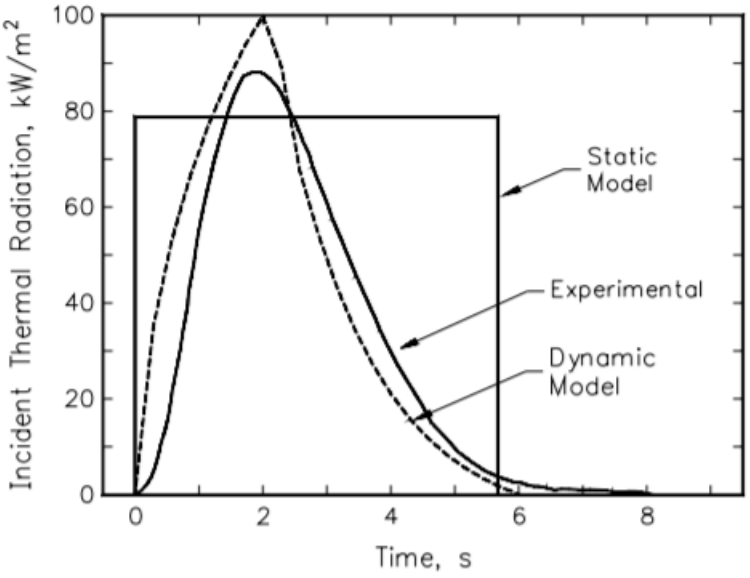

Figure 2-24 Dynamic model compared with experimental data. Reproduced from (67)

This approach could be used to place safety distances around pipelines as the model also calculates the distances for different atmospheric stability categories illustrating the effect of environmental conditions (77). These models have been typically used for fireballs from BLEVEs.

Computational fluid dynamic models have been developed to model the thermal radiation from fireballs. Sellami developed a model and validated it against large scale

BLEVE test data from British Gas. Most commonly the Roberts model, based on releases from LPG fireballs to pipeline releases, has been used. Values of a, b, c and d constants are provided by CCPS, which can be used to derive safety distances for specific heat radiation levels (40).

2.6.4. Application of the Wang Method for Different Diameter Pipelines

The model discussed in Section 2.6.3 for thermal radiation can be used to investigate the effect of pipeline diameter. The mass of gas involved is as calculated in Section 2.2.4. To calculate the distance to 14.7, 25.6 and 40 kW m^{-2}, the following assumptions are made for the values/plots in Table 2-7 and Figure 2-25:

- Pipeline length of 2500 m.
- Gas pressure of 70 bar.
- Density of gas is 60.798 (calculated using the AGA8-92DC method (47)).
- Using values of c = 6.48 and d = 0.325 for Equation (2-20).
- Assuming ΔH_c = 52 kJ kg^{-1}.
- Fraction of heat radiated as 0.3.

Table 2-7 Distance to 14.7, 25.6 and 40 kW m^{-2} for different diameter pipelines at 70 bar

Pipeline Diameter (m)	Mass of gas released in 20 seconds (kg)	Distance to 14.7 kW m^{-2} (m)	Distance to 25.6 kW m^{-2} (m)	Distance to 40 kW m^{-2} (m)
0.15	1139.7	112	78	53
1.2	164122.7	616	450	340

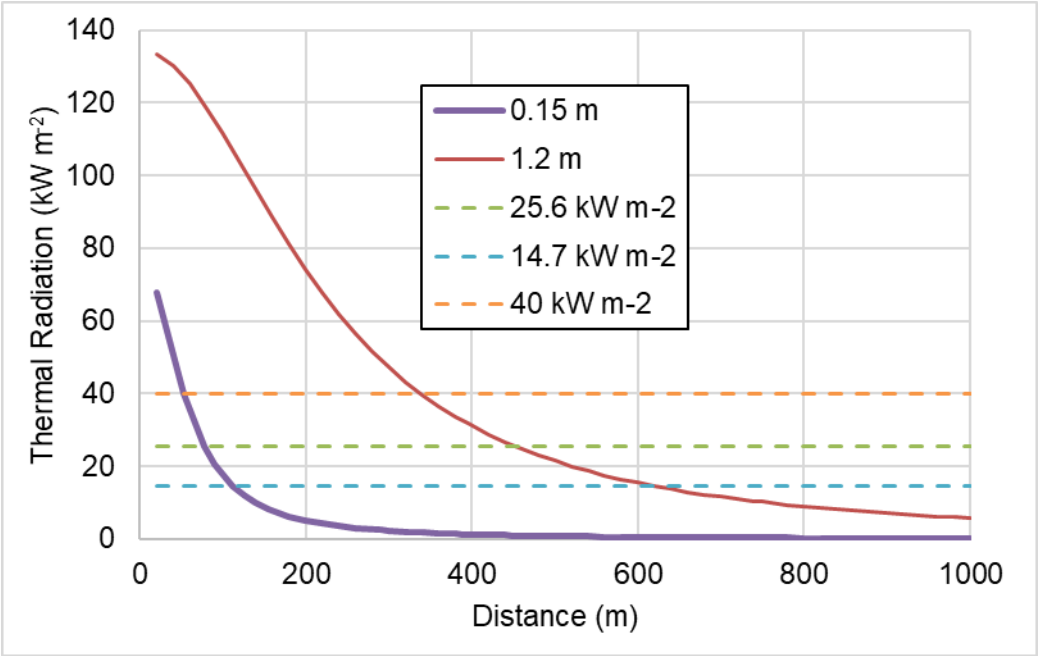

Figure 2-25 Plot of peak thermal radiation against distance for different diameter pipelines compared against 14.7, 25.6 and 40 kW m^{-2}

Based the HSE criteria of 40 kW m^{-2}, Figure 2-25 shows that any houses within 53 m and 340 m would be assumed to ignite for a 0.15 m and 1.2 m diameter pipelines respectively.

2.7. Thermal damage

2.7.1. Introduction

Section 1.3 gave examples of incidents where there were multiple fatalities. Therefore in carrying out any risk assessment account has to be taken both the individual and societal risk. Individual risk is risk of death or serious injury to which specific individuals are exposed. Societal risk is the relationship between frequency of an event and the number of people affected.

The thermal damage sustained by people and the environment will depend upon the duration and intensity of the fire (fireball plus the jet/crater fire). For the fireball phase this is stated to last up to 30 seconds and is a transient thermal radiation flux. For the jet/crater fire, practically this will depend upon the distance of isolation valves from the release and the time taken to activate these valves (as noted in the San Bruno incident (23)) in an emergency. Based on the information in Section 1.3.1, the duration of an incident can vary from 20 minutes to 125 minutes. The purpose of the current research is to investigate the effects of the fireball phase.

The effect of thermal radiation on people has been extensively studied. Specifically Rew and Hockey (78) have investigated the physiological changes (such as an increase in pulse rate, body core temperature and sweating), the level of thermal radiation that causes pain on the skin and the effects of inhalation of hot gases on the respiratory system.

Damage to skin is commonly defined as 1st, 2nd and 3rd degree burns. 1st degree burns are where damage is caused to the epidermis (the top layer) of the skin, 2nd degree burns are where damage is caused both the epidermis and dermis (lower layer of skin. Finally 3rd degree burns are where damage is caused beyond the dermis to deeper tissues (79). Humans are regularly exposed to thermal radiation from the sun which on a clear day can reach ~1 kW m^{-2}. Harm caused by greater heat fluxes are shown in Table 2-8.

Table 2-8 Heat flux consequences. Apdated version by Phylaktou reproduced from (80)

Thermal flux (kW m^{-2})	Consequences
170	Maximum flux measured in a post flashover compartment.
80	Thermal protective performance test for personal protective.
52	Fibreboard ignites at 5 seconds.
37.5	Sufficient to cause damage to process equipment (steel structures).
29	Wood ignites, given time (without a pilot light or a spark).
20	Typical beginning of flashover at floor level of a residential room.
16	Human skin: Sudden pain and 2nd degree burn blisters after 5 seconds.
12.5	Wood produces ignitable volatiles by pyrolysis (with a pilot or a spark) – Limit for determining separation distances between buildings.
10.4	Human skin: Pain after 3 seconds, second degree burn blisters after 9 seconds.
6.4	Human skin: Second degree burn blisters after 18 seconds.
4.5	Human skin: Second degree burn blisters after 30 seconds. Tenability limit for protected personnel.
2.5	Human skin: burns after prolonged exposure, radiant flux exposure typically encountered during firefighting. Tenability limit for unprotected people exposure.
1.4	Sunlight, sunburns potentially within 30 minutes. Sunburn is NOT a thermal burn. It is cause by DNA damage due to ultraviolet radiation.

Table 2-8 implies an associated duration before the harm is realised for exposure that is sustained at the specified level. Research has been carried out to determine the thermal radiation and duration of exposure (i.e. thermal dose) required for different harm criteria. The concept of thermal dose for fatalities is based on data from nuclear explosions and Eisenberg (81) states the effects of thermal radiation are generally proportional to $\dot{q}^{4/3}$t. The relationship for thermal dose is given as:

$$L = \ddot{q}^{\frac{4}{3}} t \qquad \textbf{(2-32)}$$

Where:

L = Thermal dose units (TDU) ((kW m^{-2})$^{4/3}$ s)

q̈ = Thermal radiation flux (kW m^{-2})

t = Time (s)

Equation (2-32) is based on data from 20 KT, 1 MT and 20 MT nuclear tests and is shown in Table 2-9 (81). A plot of thermal dose to the 4/3 exponent ($ï^{4/3}t$) against fatality criteria for the 3 tests is shown in Figure 2-26 i.e. the 4/3 exponent gives the same thermal dose for each of the different magnitude tests/harm criteria. However for other harm criteria, the probability of the specified injury (1st and 2nd degree burns) and associated thermal dose units is stated as being dependent upon a 1.15 exponent as opposed to 4/3 as shown in Figure 2-27.

Table 2-9 Harm criteria and associated dosage from nuclear tests

Probability of fatality (%)	Duration (s)	Radiation intensity (kW m^{-2})	Dosage ($ï^{4/3}t$)
1	1.43	14.0	1099 x 10^4
1	10.1	33.1	1073 x 10^4
1	45.2	10.2	1000 x 10^4
50	1.43	263.6	2417 x 10^4
50	10.1	58.0	2264 x 10^4
50	45.2	18.5	2210 x 10^4
100	1.43	586.0	7008 x 10^4
100	10.1	128.0	6546 x 10^4
100	45.2	39.8	6149 x 10^4

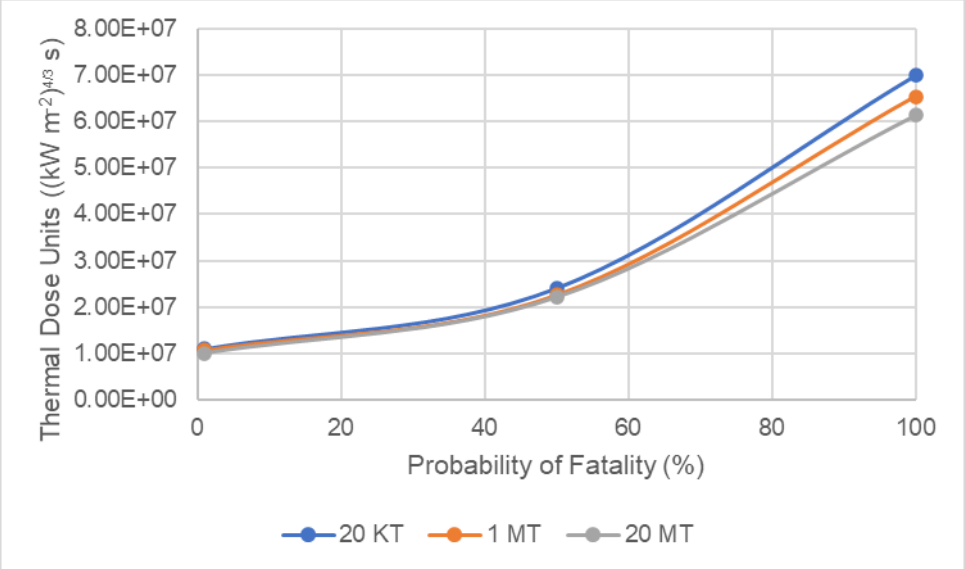

Figure 2-26 Relationship between thermal dose unit and probability of a fatality for the three different nuclear tests. Derived from (81)

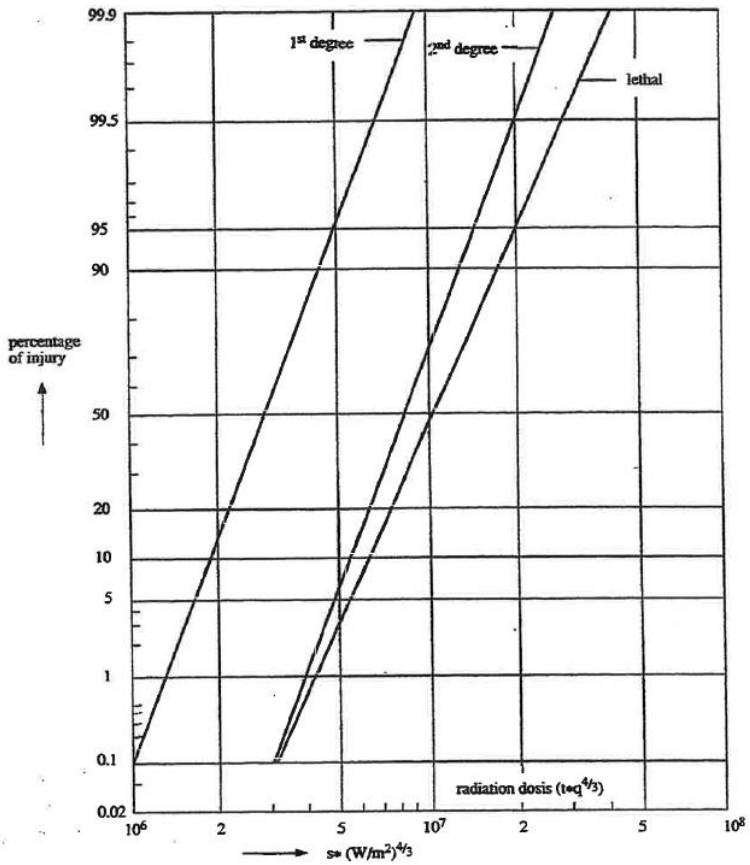

Figure 2-27 Relationship between thermal radiation dose and probability of injury. Reproduced from (57)

An important consideration is that nuclear events emit thermal radiation in the ultra violet (UV) region as opposed to hydrocarbon fires which emit thermal radiation in the infrared region. A dose from a UV source needs to be 2.23 times greater than one from an infrared source to inflict the same harm (78), (82). There are other factors such as escape speed, human response, availability of shelter, advances in healthcare and type of clothing can affect whether a fatality since the nuclear experiments were carried out. Currently, there are different thermal dose exposures quoted for different harm criteria. Using the 4/3 exponent relationship, there are the following ranges for different harm criteria:

- 111 to 120 $(kW\ m^{-2})^{4/3}$ s for pain (see Figure 2-28).
- 107 to 242 $(kW\ m^{-2})^{4/3}$ s for blister formation (see Figure 2-29)
- 830 to 1133 $(kW\ m^{-2})^{4/3}$ s for 2nd degree burns (see Figure 2-29)
- 655 to 720 $(kW\ m^{-2})^{4/3}$ s for significant injuries (see Figure 2-36)
- 1060 to 1230 $(kW\ m^{-2})^{4/3}$ s for 1% fatality (see Figure 2-36)
- 4070 to 4630 $(kW\ m^{-2})^{4/3}$ s for 50% fatality (see Figure 2-36)
- 5813 to 6541 $(kW\ m^{-2})^{4/3}$ s for 100% fatality (see Figure 2-36)

This lowest thermal dose values calculated above vary by at approximately 10% with a 4/3 exponent relationship.

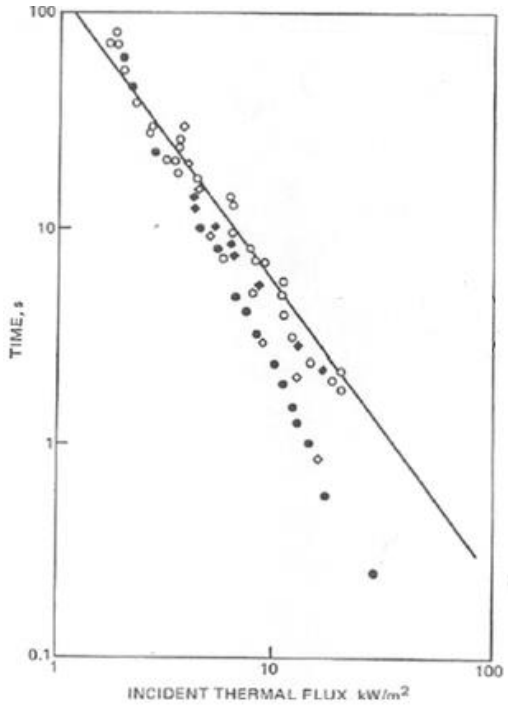

Figure 2-28 Relationship for pain for different thermal fluxes (83)

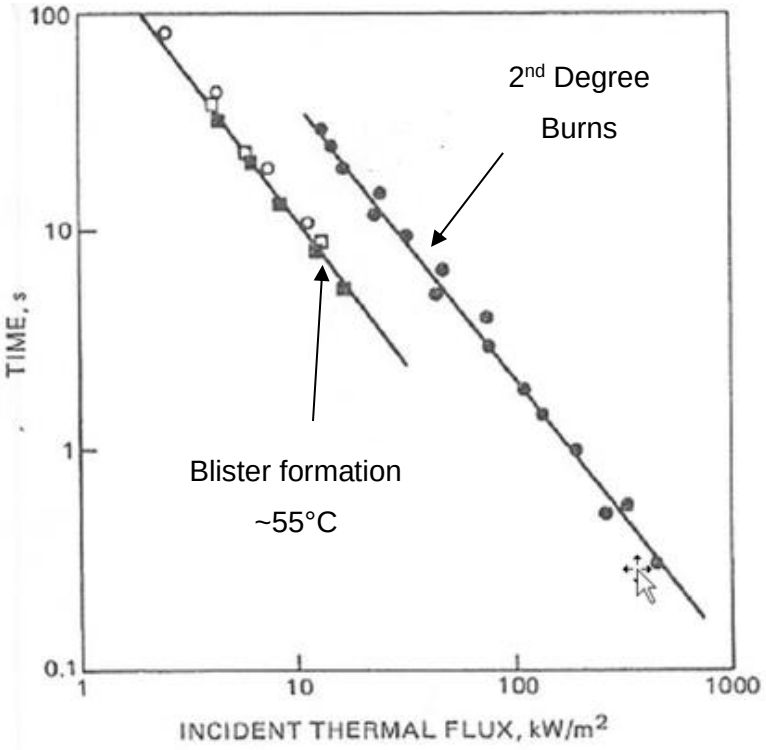

Figure 2-29 Relationship for blister formation and 2nd degree burns for different thermal fluxes and durations (83)

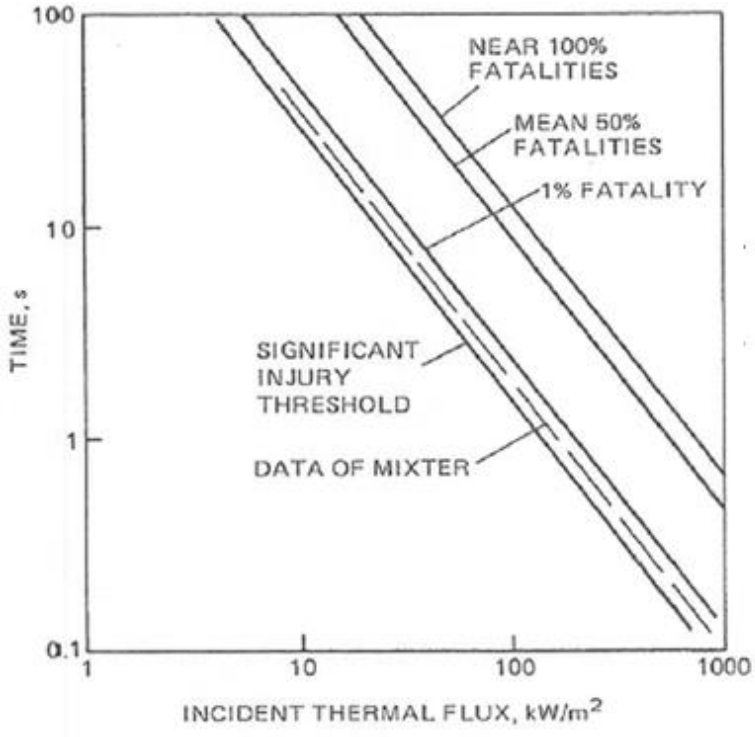

Figure 2-30 Relationship for significant injuries and 1%, 50% and 100% fatalitiles for different thermal fluxes and durations (83)

2.7.2. Human Vulnerability

A list of fatalities following a pipeline rupture is given in Table 2-10. As already indicated, a single pipeline release can cause multiple fatalities and therefore an estimate of the societal risk is needed for any pipeline.

Table 2-10 Fatalities following Natural Gas Pipeline Releases. Reproduced from (84)

	Date	Location	No. of Fatalities
1.	March 1, 1965	Montreal, Quebec, Canada	28
2.	March 4, 1965	Natchitoches, Louisiana, USA	17
3.	April 6, 1968	Richmond, Indiana, USA	41
4.	August 16, 1970	Osaka, Japan	79
5.	October 21, 1971	Clarkston, Scotland, UK	21
6.	February 2, 1973	Eagle Grove, Iowa, USA	14
7.	January 10, 1976	Fremont, Nebraska, USA	20
8.	November 1, 1978	Colonia Benito Juarez, Mexico	52
9.	August 16, 1980	Shizuoka, Japan	15
10.	April 22, 1992	Guadajalara, Mexico	252
11.	November 21, 1996	San Juan, Puerto Rico	33
12.	August 19, 2000	Carlsbad, New Mexico, USA	12
13.	March 16, 2004	Arkhangelsk, Russia	58
14.	July 30, 2004	Ghislenghein, Belgium	24
15.	September 12, 2011	Nairobi, Kenya	100
16.	August 6, 2013	Rosario, Argentina	21
17.	June 28, 2014	Andhra Pradesh, India	18
18.	July 31, 2014	Kaohsiung, Taiwan	30

The variability in the numbers of casualties in Table 2-10 highlights why using incident data to make changes to fatality criterion has to be treated with caution. Three studies have been commissioned by the HSE (85) in the UK to determine criteria for vulnerable and average populations. The first study determined that 1000 TDU was a reasonable criterion for an average population with a standard level of clothing. The second project defined the LD_{50} criterion which was the basis for the SLOD criterion for an average population which specified a level of 1800 TDU. However, the research found that

there was a strong dependence on the age of the population exposed, for example, the elderly have thinner skin and so for the same area of burn the likelihood of fatality is greater for older people. Based on this criterion the HSE were using a dose of 500 kW m^{-2} for vulnerable populations at the time the HSE published the third report in 2000 (85).

Vulnerable populations are defined as those who may not respond effectively to evacuation procedures in an emergency. In addition to the elderly, this includes children. Where skin depths are lower the chances of 1st and 2nd degree burns increase and additionally, the survival from operations needed to heal such injuries are also less likely for vulnerable populations. The HSE reports cite the original methodologies by Eisenberg et al for the effects of thermal radiation on people. Other approaches include comparing the total surface body area which receives a partial burn against a mortality chart (57).

Table 2-11 Comparsion of criteria for thermal dose. Reproduced from (85)

Source	**Dosage (kW m^{-2})$^{4/3}$s for probability of fatality**	
	1% Dangerous Dose	**50% (SLOD)**
Eisenberg et al (1975)	960	2380
Tsao and Perry (1979)	420	1050
HSE Kinsmann (1991)	1000	1800
TNO Green Book	520	-
API 1990 at 1 min exposure	700	-

Using the harm criteria, a duration of exposure to a 6 kW m^{-2} can be calculated using the 4/3 exponent as given in Table 2-12.

Table 2-12 Thermal dose consequences (Adapted from (86))

Level of Exposure (TDU) (kW m^{-2})$^{4/3}$ s		**Equivalent duration for 6 kW m^{-2} exposure (s)**		**Consequences**
Mean	**Range**	**Mean**	**Range**	
92	86-103	8.4	7.9-9.5	Pain
105	80-130	9.6	7.3-11.9	Threshold first degree burn
290	240-350	26.6	22.0-32.1	Threshold second degree burn
1000	870-2600	91.7	79.8-238.5	Threshold third degree burn

Table 2-12 shows that pain will be caused for events of around 10 seconds at 6 kW m^{-2}. If the thermal flux is 12 kW m^{-2} this reduces to approximately 3 seconds. It must be noted that levels below 1 kW m^{-2} for people must be screened out as values more than 1000 or 500 TDU are possible although humans will be able to withstand levels for infinite period (85). Comparisons with fatalities arising from previous incidents has found that the dosage criteria overpredicts the actual number of fatalities (82) which supports the need for further investigation into the criteria.

The values presented in Table 2-12 are derived from steady-state fluxes. However, since fireballs produce a transient thermal flux, it is essential to consider the variation in thermal radiation flux. Assuming the radiation from a fireball at a given location increases by 10 kW m^{-2} per second and reaches a maximum of 70 kW m^{-2} and then falls at the same rate, the cumulative dose received by an individual at such a location will be shown in Table 2-13.

Table 2-13 Thermal dose from a theoretical fireball

Time	Radiation (kW m^{-2})	Dose in Time Interval ((kW m^{-2})$^{4/3}$ s)	Cumulative Dose ((kW m^{-2})$^{4/3}$ s)
0	0	0	0
1	10	22	22
2	20	54	76
3	30	93	169
4	40	137	306
5	50	184	490
6	60	235	725
7	70	288	1013
8	60	235	1248
9	50	184	1433
10	40	137	1569
11	30	93	1663
12	20	54	1717
13	10	22	1738
14	0	0	1738

In Section 2.7.1, different exponents for the thermal dose were proposed for different harm criteria. Although there are variations in the thermal dose criteria outlined in Section 2.7.1, Hockey and Rew have examined these differences. Hockey and Rew (82) concluded while there is some conservatism with the 4/3 exponent, it is still deemed appropriate given the significant harm caused by full-thickness burns. To investigate these limits for humans as part of this study is not practical. Nevertheless, considering that humans spend the majority of their time indoors (17) the criteria for

shielding provided by buildings becomes a crucial factor in determining whether a fatality occurs or not. This is discussed further under Sections 2.7.3 to 2.7.5.

2.7.3. Physical Damage

To understand the effects of thermal radiation on both the built and natural environments, it is essential to first determine the level and duration of thermal radiation exposure at a specific distance. Various criteria are used to assess ignition in solid materials. These criteria consider factors such as the material's temperature, critical mass loss rate, or incident thermal radiation level. The HSE (18) states a thermal radiation threshold of the use >40 kW m^{-2} for 100% fatalities. or situations where individuals might attempt to escape from a building, the range is set between <25.6 kW m^{-2} and >14.7 kW m^{-2}. A value <14.7 kW m^{-2} is regarded as a level at which a building is not expected to ignite.

Thermal radiation can exert an influence on the surrounding environment, impacting structures, plants, and vegetation. For example an ignited release from a 44 bar gas pipeline in 2011 caused damage to a small area (100 m^2) of forest and an ignited rupture release at Edison in 1994 cause thermal damage to apartment blocks within 170-300 m of the rupture site (87).

In the built and natural environment, various factors influence whether materials or vegetation undergo pyrolysis in the presence of a fire. These variables are not exclusive to ignited pipeline releases and have been extensively studied. Factors include fuel arrangement, moisture levels, material thickness, chemical composition, orientation, prevailing weather conditions, wind and topography (88), (89).

Wood has been a subject of numerous studies (88) examining constant thermal flux, and findings indicate that moisture levels significantly impact the likelihood of ignition. Combustion tends to occur more readily in dry wood, emphasizing the importance of low moisture content for ignition. Water has a high latent heat of vaporisation, so considerable thermal radiation is needed to dry out a substance.

Larger fuel loads necessitate a higher amount of thermal radiation to ignite the entire area. Conversely, if the arrangement of the fire load restricts the circulation of air, it becomes challenging for the fire to propagate.

Strong winds enhance the availability of oxygen and can preheat fuel ahead of the fire front. Nevertheless, high wind speeds can also escalate fire temperatures by fanning the flames, causing the fire front to travel more rapidly and consume less fuel (90), (91).

Topography plays a role in influencing the climate around a fire and can expedite the spread of the fire, particularly if it is moving uphill (92).

Earlier studies have employed steady-state thermal radiation to examine the ignition of solids. The continuous exposure of a solid to sustained radiation can elevate its temperature to a point where pyrolysis initiates. Over time, the pyrolysis layer progresses through the solid (moving away from the radiation source), leaving behind a char layer, while hot volatile gases ascend. The rate of this decomposition is idealised by an Arrhenius type reaction (89). In the context of volatile production, two key terms are "piloted ignition" and "spontaneous ignition". Piloted and spontaneous ignition of solids both require decomposition of the solid such that volatiles are driven off at sufficient rate to mix with air.

If a separate pilot flame is applied to a volatile gas, which causes a flash of flame, this is known as the flashpoint. If the flame were to be sustained under a pilot flame, this is known as the firepoint. For wood, the lowest reported value for an indefinite exposure at which volatiles ignite under a pilot flame is 12.5 kW m^{-2} (88). In the piloted ignition case, the required temperature of the volatiles for ignition is lower, as the additional energy to ignite the mixture is provided by an electric arc (spark) or a small flame itself (89).

Spontaneous ignition, or autoignition, occurs when a flame appears due to thermal radiation without an external ignition source like a pilot light. As solids undergo pyrolysis, they release volatile gases that mix with air, forming a combustible mixture. This mixture can ignite when it reaches a critical temperature or is exposed to a certain level of heat flux (88). The temperature of the solid required for this phenomena to occur is 300-500°C (89).

Numerous variables contribute to the production of volatiles, encompassing the type of solid (whether thermally thin or thick), physical and thermal properties of the material (density, orientation, specific heat capacity, thermal conductivity), ambient conditions (such as oxygen concentration and air flow rate), heating methods, and the impact of glowing combustion.

This can be simplified to 3 steps (89):

1. The time to raise the solid to a sufficient temperature to achieve pyrolysis and generate fuel.
2. The time needed for the flammable fuel to mix with air.
3. The time needed for the flammable mixture to proceed to flaming combustion (with or without the presence of a pilot).

Of these steps, the first step is the most significant (89), i.e. the time to raise the temperature of the solid to the ignition temperature (pilot or spontaneous).

Thermally thin materials are those in which the temperature of the solid is assumed to be constant throughout, while thermally thick materials exhibit a temperature gradient through the material. In practical terms, most elements near a gas pipeline fire are considered thermally thick, such as other gas pipeline equipment and buildings. However, it's important to note that if delamination of a material occurs, as in the case of multiple layers of paint, a delaminated layer could be considered thermally thin.

If a simple conduction model is assumed for radiation onto to a solid, then information on solids can be derived from the thermal properties. Thermally thin materials are defined by their Biot number. The Biot number is ratio of internal and external resistance to heat conduction (88). The Biot Number is given by the formula:

$$\mathrm{Bi} = \frac{h l_t}{k} \qquad \textbf{(2-33)}$$

Where:

l_t = thickness (m)

h = convective heat transfer coefficient (kW m^{-2} K^{-1})

k = thermal conductivity (kW m^{-1} K^{-1})

Where the Biot number is less than 0.1, the material is considered to be thermally thin. Above 0.1, the material is considered to be thermally thick and consideration of temperature gradients within the material are required (e.g. thermal inertia of the material). The use of the Biot number for thermally thin materials provides a straightforward correlation, but it's crucial to consider the experimental conditions when evaluating the ignition of materials. Other factors to be taken into account are density (see Figure 2-31), different materials (see Figure 2-32 to Figure 2-34) and effects of draughts (see Figure 2-35). The graphs show based on steady state exposure:

- As density increases, the time to ignition increases (see Figure 2-31).
- The time to ignition varies for different types of woods and vinyl fabrics varies as the materials will have different thermal conductivity and specific heat capacity values as well as densities (see Figure 2-32 to Figure 2-34).
- Figure 2-35 shows how different experimental conditions can affect the time to ignition.

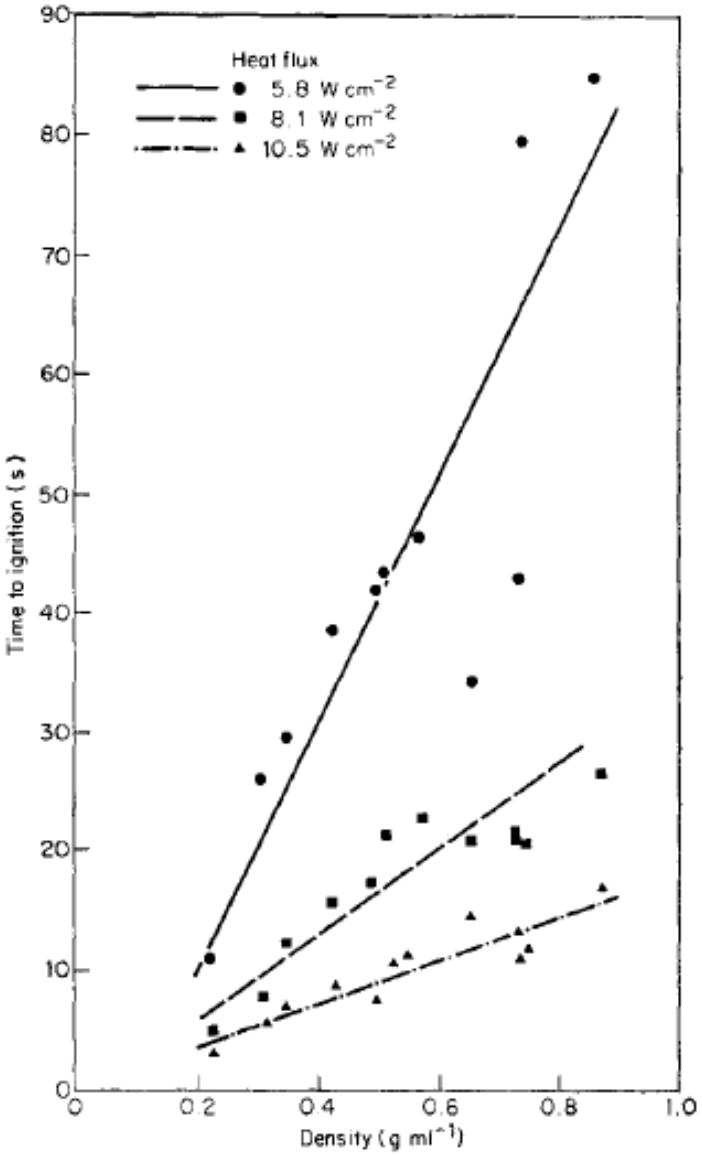

Figure 2-31 Piloted ignition of Cellulosic Materials (93)

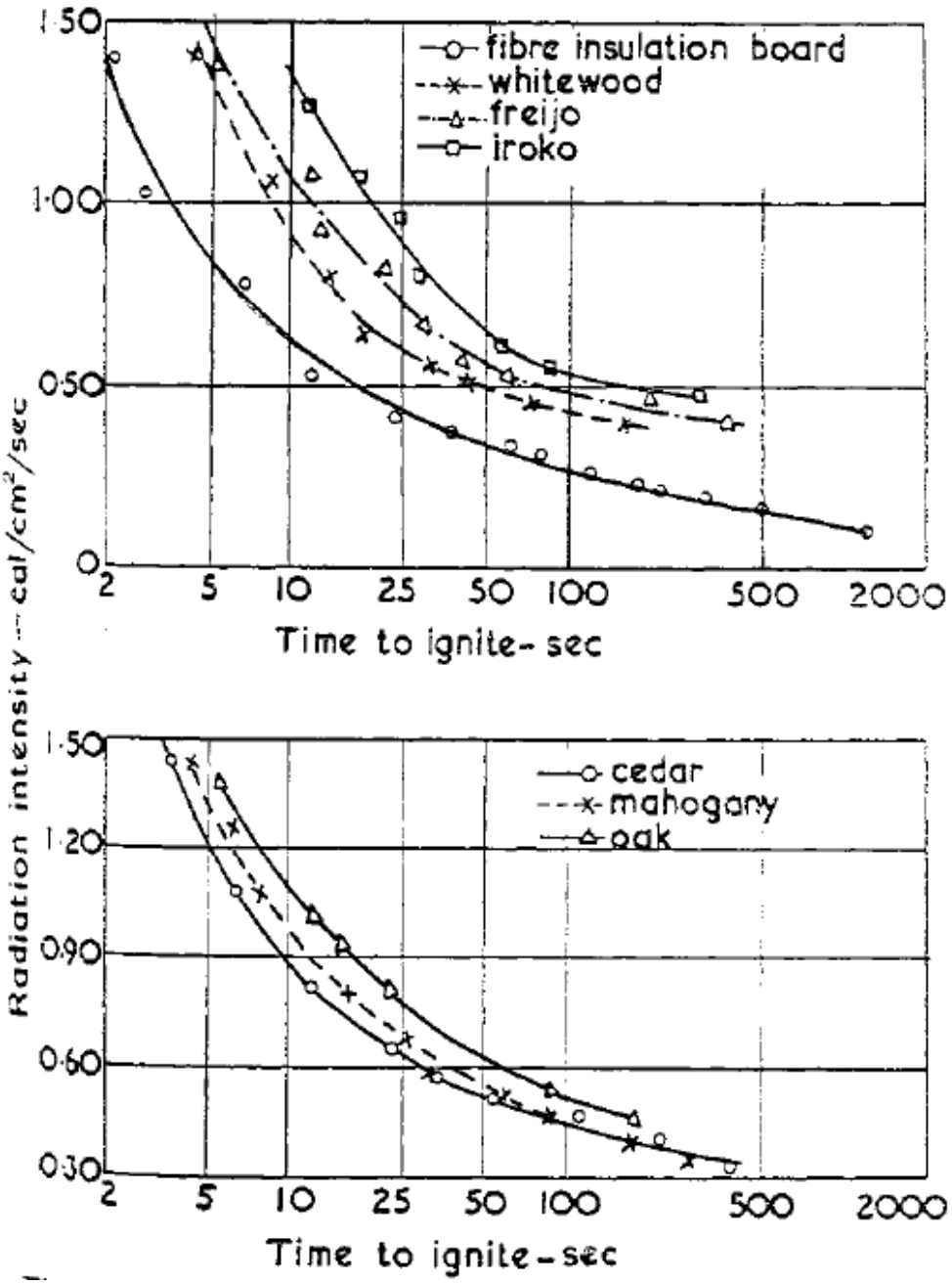

Figure 2-32 Piloted ignition of Wood Based Materials (94)

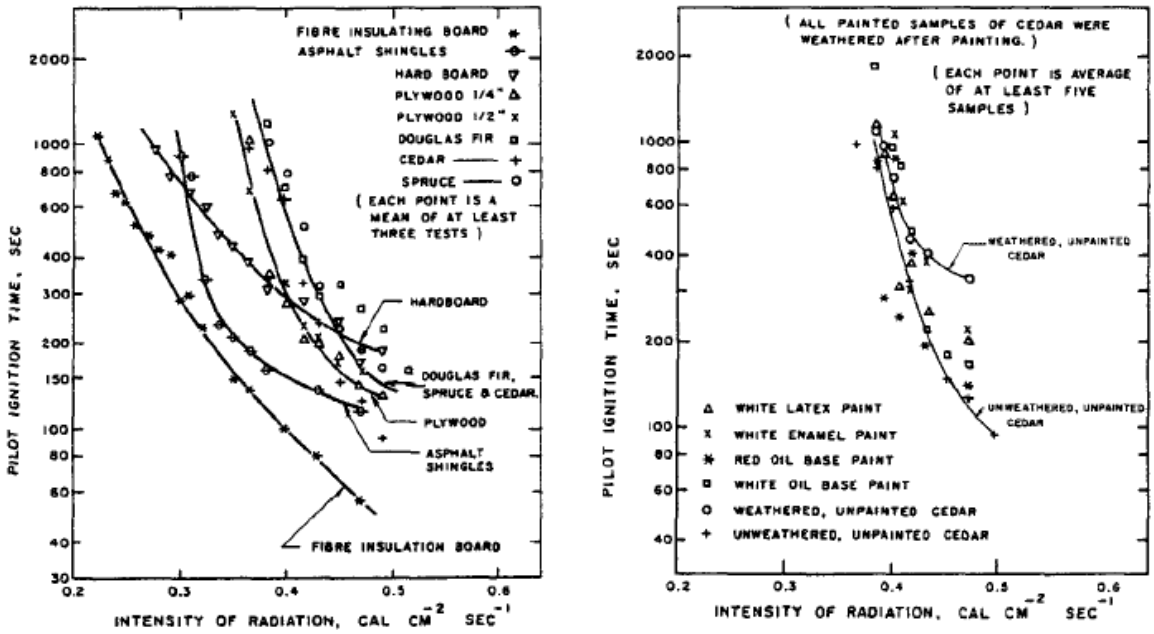

Figure 2-33 Piloted ignition of Wood Based Materials (95)

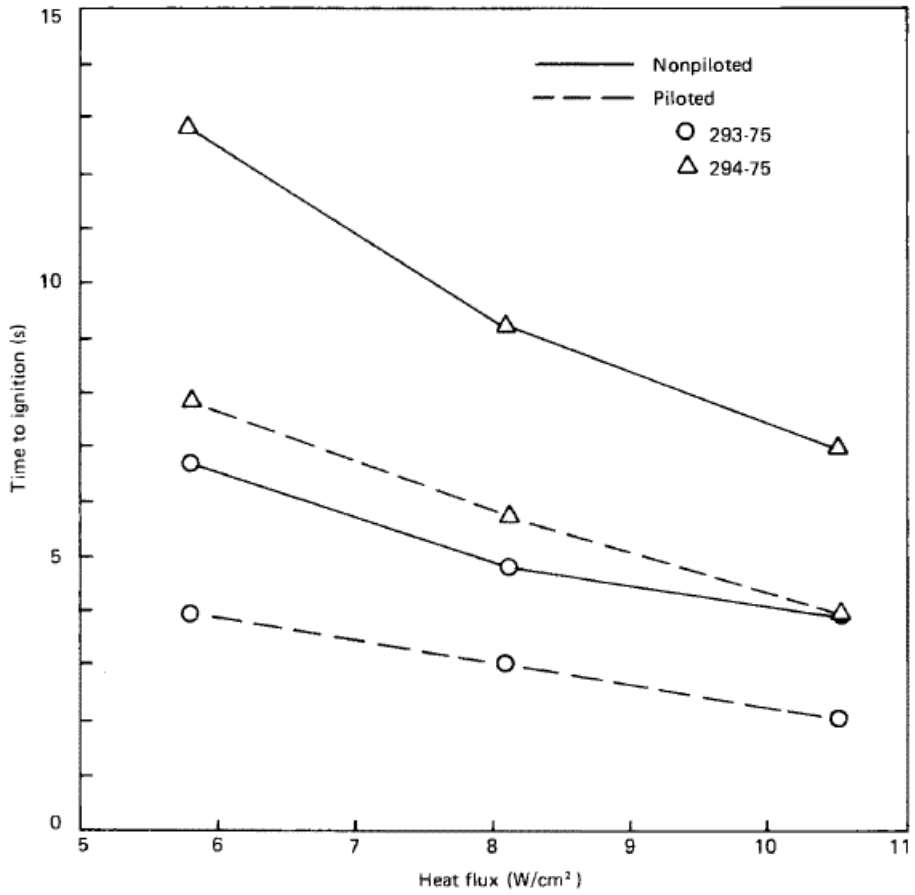

Figure 2-34 Piloted and spontaneous ignition of expanded vinyl fabrics (96)

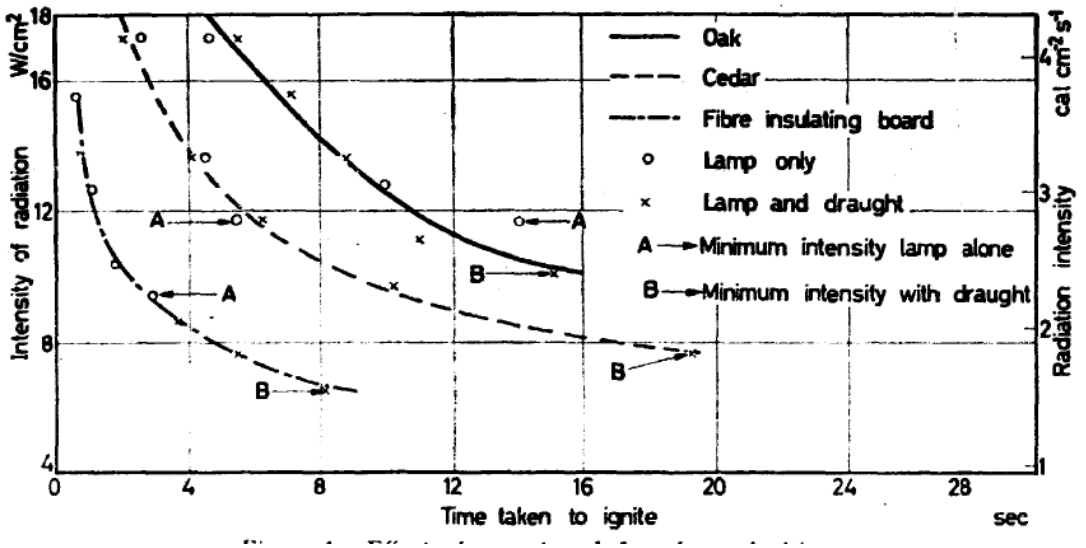

Figure 2-35 Piloted ignition of Wood Based Materials (97)

2.7.4. Natural Environment

Pipeline operators generally lay pipelines in rural areas surrounded by vegetation. Different plant species surrounding these pipelines have varied moisture content and fire resistance. For example, juniper trees, with their thin bark and lack of defensive mechanisms, are particularly vulnerable to fires (98).

For vegetation, fire resistance is dependent on bark thickness, other vegetative insulation, above ground re-sprouting, underground roots and stems (99).

A thick bark insulates and protects the cellular plant tissue from heat damage.

Leaf sheaths provide some protection, for example grasses have cells which promote growth (meristems) at the leaf base so are protected from damage.

Soil is a good insulator therefore buds underground are well protected. Plants can survive fires by re-sprouting stems and roots positioned beneath the ground.

To assess whether damage to the environment is significant, in the UK COMAH reports use environmental damage classifications provided within the Chemical and Downstream Oil Industries Forum (CDOIF) guidance on risk tolerability. Damage to environmental receptors is depends on the area and the duration of harm (100). Different areas are depending on the sensitivity of the receptor.

Area thresholds for land and water receptors are those greater than 0.5 hectares or 5-10% (whichever is the lessor) is a threshold, although the area is greater for less sensitive receptors 2-10 hectares.

Based on the incidents referred to Section 1.3 the damaged areas are not likely to be in excess of these values, particularly as it is unlikely that a pipeline would be routed through a sensitive environmental areas.

Damage to the environment has been previously used in investigations. In the Zarzalico incident (101), thermal damage caused to pine needles 90 m from the fireball was used to estimate the thermal radiation produced by the fire. The fireball occurred following a car collision with a 21 tonne LNG tanker. Based on the damage to the pine needles, the thermal radiation level was estimated to be 55 kW m^{-2}. Hence, damage resulting from any fireball in the far field could furnish an incident investigator with evidence to confirm the sequence of events following a pipeline rupture.

A number of studies on the damage to the environment has been carried with respect to forest fires damage (102). In particular, studies have shown that pine needles can endure a temperature of 57°C for 5 minutes. However, exposure beyond 60°C leads to irreversible damage to the needles (103).

2.7.5. Built Environment

Although 14.7 kW m^{-2} is the minimum level quoted by the HSE, IGEM/TD/2 refers to the use of the piloted ignition value for wood. Section 2.7.3 referred to a level of 12.5 kW m^{-2}. For the purposes of this research comparison is being made to 14.7 kW m^{-2} level.

However, there are incidents where nearby buildings have not ignited following a fireball incident, for example the 2004 Belgium incident, see Figure 2-36.

Figure 2-36 Photos of fires from eyewitnesses. Reproduced from (26)

The incident in Belgium occurred as a result of a latent defect on the pipeline failing while the gas pressure in the pipeline was being increased. After the failure, a gas plume was observed following a puncture. Subsequently, while firefighters were present, the puncture ruptured, releasing gas that ignited, leading to a fireball and subsequent crater fire. At the time of the leak, three zones were being classified around the leak to determine the hazardous areas (26) during the emergency response.

Zone 1 was the forbidden zone and is defined as the zone with a high chance of mortality which may be entered only in highly exceptional circumstances following appropriate risk assessment and with the required protective clothing. Zone 1 is defined as 10 kW m^{-2} after 30 secs or the house burning distance.

Zone 2 was an area which may be entered only by the fire services wearing required protective clothing and paying attention to their own safety. Zone 2 is defined as 3 kW m^{-2} after 30 secs.

Zone 3 was the isolation zone where only the emergency services may enter from outside, although anyone already within this zone may stay there. People evacuated from inner zones must at least be taken outside this zone.

Zone 1 for this incident (based on pipeline diameter of 1000 mm and pressure of 80 bar) was defined as 210 m. Figure 2-37 shows this was slightly larger in one direction for this incident and slightly less in another direction. Figure 2-38 shows damage to wooden pallets just outside the building in a location which is relatively close to the building. However, Figure 2-39 and Figure 2-40 show evidence unaffected material within the Zone 1 hazard zone. Figure 2-41 shows no damage inside the building.

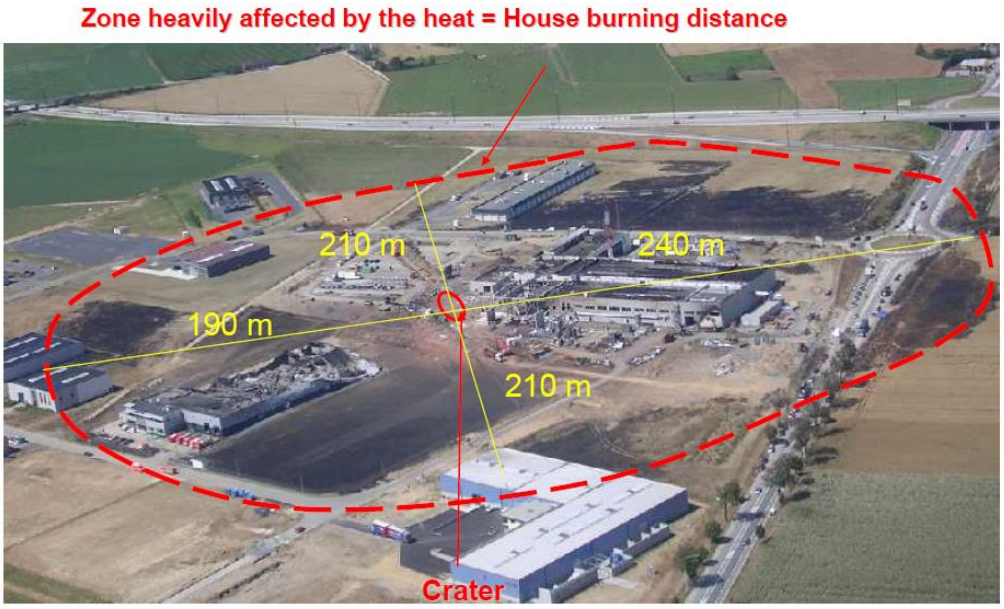

Figure 2-37 Brunt area after pipeline incident at Belgium. Reproduced from (26)

Figure 2-38 Damage caused to wooden pallets. Reproduced from (26)

Figure 2-39 Damage to the building located to the west of the pipeline rupture.

Reproduced from (26)

Figure 2-40 Shielding effects to the west of the pipeline rupture

Reproduced from (26)

Figure 2-41 Damage inside a building 130 m from the crater. Reproduced from (26)

Zone 2 for this incident was defined as 710 m. Observations from this incident relevant for this hazard range are shown in Figure 2-42 to Figure 2-45.

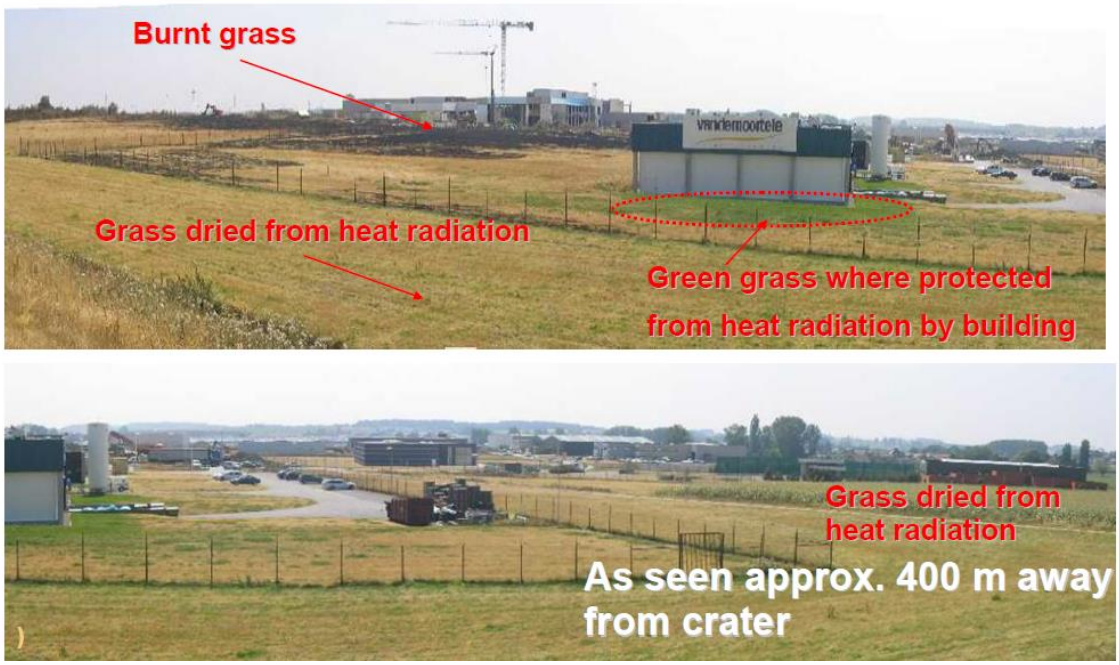

Figure 2-42 Different damage caused to grass due to shielding. Reproduced from (26)

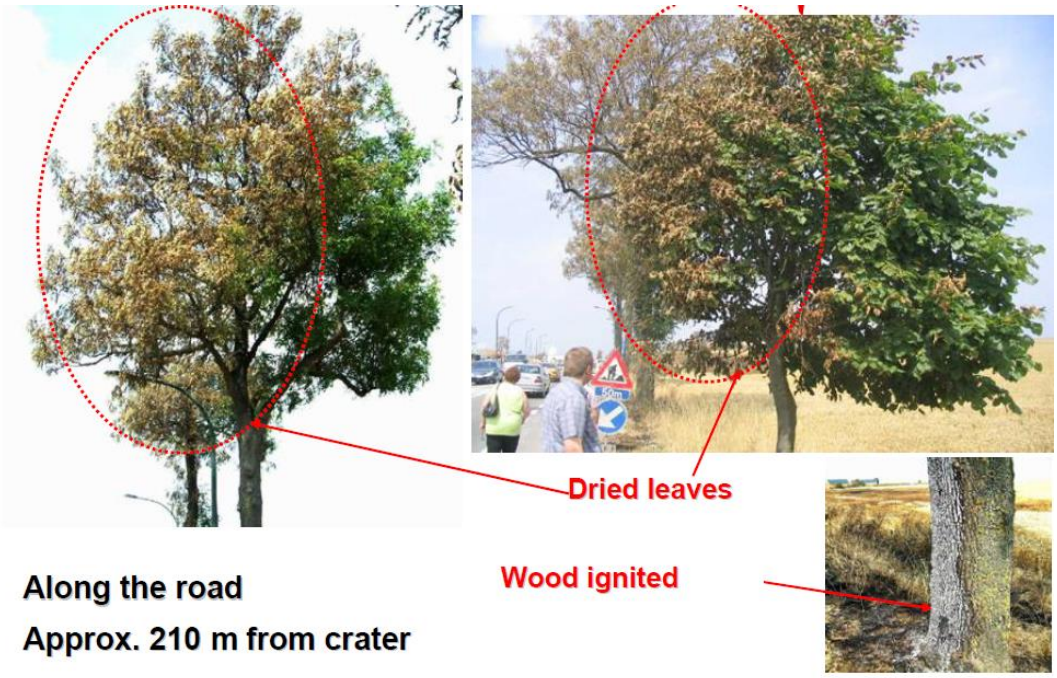

Figure 2-43 Damage caused to trees. Reproduced from (26)

Figure 2-44 Damage caused to a van. Reproduced from (26)

Figure 2-45 Damage caused to street lighting. Reproduced from (26)

Important observations from this incident include the use of shielding effects to estimate the dimensions of the fireball. Additionally, charring on trees is typically limited to the side facing the fireball/crater fire, and grass can exhibit burning, drying, or remain undamaged depending on whether it is shielded from the fireball/crater fire.

In this incident, there was a fireball followed by a crater fire. Beyond the distance at which the house burning occurs (i.e., beyond zone 1), it would be pertinent to investigate whether the damage was caused by the fireball, the crater fire, or a combination of both. For example the thermal radiation at 340 m would have been greater than 3 kW m^{-2} but lower than 10 kW m^{-2}, both of which are level than the idefinite exposure levels for most materials.

For this pipeline diamter and pressure the distance to 40 kW m^{-2} using the Wang method in Section 2.6.3 is 290 m. However, there was limited damage inside a building 130 m from the rupture but based on the current HSE criteria, anyone inside this building would likely have been considered to be a fatality. This inidcates the HSE criteria may be conservative and supports research into understanding igntion of buildings exposed to thermal radiation from fireballs.

2.7.6. Predicting Ignition

2.7.6.1. Steady State Thermal Radiation Exposure

There are thermal fluxes documented in the literature that are used for predicting ignition at constant exposure (18). For piloted ignition:

$$A_1 = (\ddot{q}_i - \ddot{q}_P)t^{\frac{2}{3}} \quad \textbf{(2-34)}$$

Where:

A_1 = constant

$\ddot{q}_i$ = incident thermal flux (kW m^{-2})

$\ddot{q}_P$ = critical thermal flux (kW m^{-2})

t = time (s)

For spontaneous ignition:

$$B_1 = (\ddot{q}_i - \ddot{q}_s)t^{\frac{4}{5}} \quad \textbf{(2-35)}$$

Where:

B_1 = constant

$\ddot{q}_i$ = incident thermal flux (kW m^{-2})

$\ddot{q}_s$ = critical thermal flux (kW m^{-2})

t = time (s)

Based on experimental results for the above equations, the results for American whitewood are:

- A_1 = 118.4 kJ m^{-2} s$^{-1/3}$
- $\dot{q}_P$ = 14.7 kW m^{-2} (The value used by the HSE)
- B_1 = 167.6 kJ m^{-2} s$^{-1/5}$
- $\dot{q}_s$ = 25.6 kW m^{-2}

It is important to understand that these heat flux values are conservative estimates, representing the minimum flux needed for wood ignition over an extended period. These equations are based on Lawson's (94) work from 1952. Subsequent work by Lawson (104) found that density also affected the time to ignition.

2.7.6.2. Variable Thermal Radiation Exposure

Most of the research referenced so far has focused on the application of a constant heat flux and the corresponding duration it takes for ignition or the time required to reach a critical temperature or mass loss rate.

One study has investigated the auto-ignition of woods under variable heat fluxes (105). Different types of woods were tested with different rates of increasing heat flux until target heat flux values of 20 kW m^{-2} and 40 kW m^{-2} were reached. It was found the time to ignition for took longer when the thermal flux was raised from 0 to 40 kW m^{-2} compared increasing the heat flux at the same rate but only to 20 kW m^{-2}. This suggests a critical dependence when the heat flux falls within the range of 20 and 40 kW m^{-2}. The rate of heat flux used was 1 kW m^{-2} s^{-1} i.e. it takes at least 40 seconds at the highest heat flux to reach 40 kW m^{-2}.

In contrast to a real pipeline release (see Section 2.4.2) where the heat flux measures around 60 kW m^{-2} at 30 m from the release and is reached in approximately 3 seconds, this study is not directly comparable to the thermal radiation produced by a fireball.

Another study (106) offers correlations for predicting the time of ignition for both thermally thick (Equation (2-36)) and thin (Equation (2-37)) samples (106). The correlations have been theoretically determined and the correlation for thermally thick materials has been compared with experimental data.

$$t_i\text{-}t_c = \left(\frac{2C}{\dot{H}_c}\right)^{\frac{2}{3}} \quad \textbf{(2-36)}$$

$$t_i\text{-}t_c = \left(\frac{2Cl_t}{\dot{H}_c}\right)^{\frac{1}{2}} \quad \textbf{(2-37)}$$

Where:

t_i = time to ignition (s)

t_c = time to reach critical heat flux (s)

C = heat and storage transfer properties of the solid (J cm^{-3})

l_t = sample thickness (m)

$\dot{H}_c$ = rate of change of heat flux (following attainment of critical heat flux level) (W cm^{-2} s^{-1})

The TNO Green Book (57) describes the concept of critical radiation for various materials, emphasizing that these values differ among materials. The book includes a heat balance equation incorporating elements of both radiation and convective heat transfer to define critical radiation intensities for two damage criteria. The level 1 damage criteria is defined as breakage or failure of elements without surfaces actually burning. The level 2 damage criteria is defined as discolouration or deformation of the surface of materials without initiation of fire.

Critical radiation intensities for different materials and damage criteria given in The Green Book are shown in Table 2-14.

Table 2-14 Critical Radiation Intensities for Different Materials

Material	Critical Radiation Intensity (kW m^{-2})	
	Damage Level 1	Damage Level 2
Wood	15	2
Synthetic materials	15	2
Glass	4	N/A
Steel	100	25

The TNO Green Book (57) suggests the values can be used above for indefinite periods (i.e. more than half an hour), but for shorter periods a more refined approach may be required.

2.7.7. Summary

Criteria for the ignition of materials in the built environment rely on fixed thermal radiation fluxes, with little or no consideration given to the duration of the exposure. Hence, further research is warranted to deepen our understanding of the effects of thermal radiation fluxes on the built environment.

CHAPTER 3

EXPERIMENTAL SET UP AND MEASUREMENT TECHNIQUES

The Spadeadam Testing and Research Centre has been used carry out a number of fracture propagation and BLEVE tests whereby data on thermal radiation levels and gas outflow rates has been measured. The facilities at Spadeadam and how the data was obtained from the tests are described in Section 3.1.

The cone calorimeter based in the University of Leeds laboratory has been suitably modified and used to study the behaviour of material samples to transient heat fluxes replicating as far as possible the pulse heat flux observed in the large scale tests. The revised setup of the cone calorimeter is described in Section 3.2.

3.1. Large scale Fracture Propagation Tests

3.1.1. DNV Spadeadam Testing and Research Centre

The DNV research facility is located on an active Ministry of Defence (MOD) site at Spadeadam in Cumbria. The Spadeadam research and test site is one of the world's leading full-scale major hazard test facilities, occupying some 50 hectares of land in a remote part of northern England. The sheer size and remoteness of the facility means that appropriate exclusion zones may be enforced, thus allowing full-scale tests such as vapour cloud explosions, rapid crack propagation, BLEVE's, confined vented explosions etc. to be undertaken.

The site is supported by an experienced team expert in large scale fire, explosion and blast testing. The site has previously carried out fracture propagation tests (107).

The Spadeadam site was used to carry out two large scale fracture propagation rupture tests.

Figure 3-1 DNV GL Major Hazard Research and Testing Site at Spadeadam

3.1.2. Fracture Propagation Test Facilities

To carry out the tests, the fracture propagation facility at the Spadeadam Test Site was used. The set-up (shown simply in Figure 3-2) consisted of two 48 inch (1219 mm) diameter pipe reservoirs each with a length of approximately 165 m. The reservoirs were spaced with a gap between the reservoir ends of approximately 130 m where the test section comprising of eleven pipe lengths was be installed. The length of reservoir on each end of the test section simulated an infinitely long pipeline thus enabling the gas decompression from the test section to replicate actual pipeline conditions without experiencing any pressure reflections during the fracture event. The outer end of each of the reservoirs was terminated with a dome end and fitted with connections to a 12 inch nominal bore (323 mm) diameter gas recirculation loop.

The gas recirculation loop was constructed from 12 inch nominal bore (323 mm) diameter, steel pipe (material grade X65) and connected the reservoirs at each end through 12 inch (300 mm) diameter full bore isolation ball valves. The recirculation loop incorporated a set of fan units providing a circulation velocity of nominally 0.5 m s^{-1} in the 48 inch (1219 mm) diameter test pipe to ensure that a homogeneous gas mixture was achieved throughout the test rig. A tube type heat exchanger was also installed in the recirculation loop and was used to cool the test fluid to the required test temperature. A heat exchanger (supplied with an ethylene glycol/water mixture and circulated through two refrigeration units) was used to control the temperature of the gas. To reduce any heat loss or heat gain throughout the system, the flow loop,

reservoirs and test section were completely insulated with spray applied polyurethane foam with sufficient thickness (see Figure 3-3).

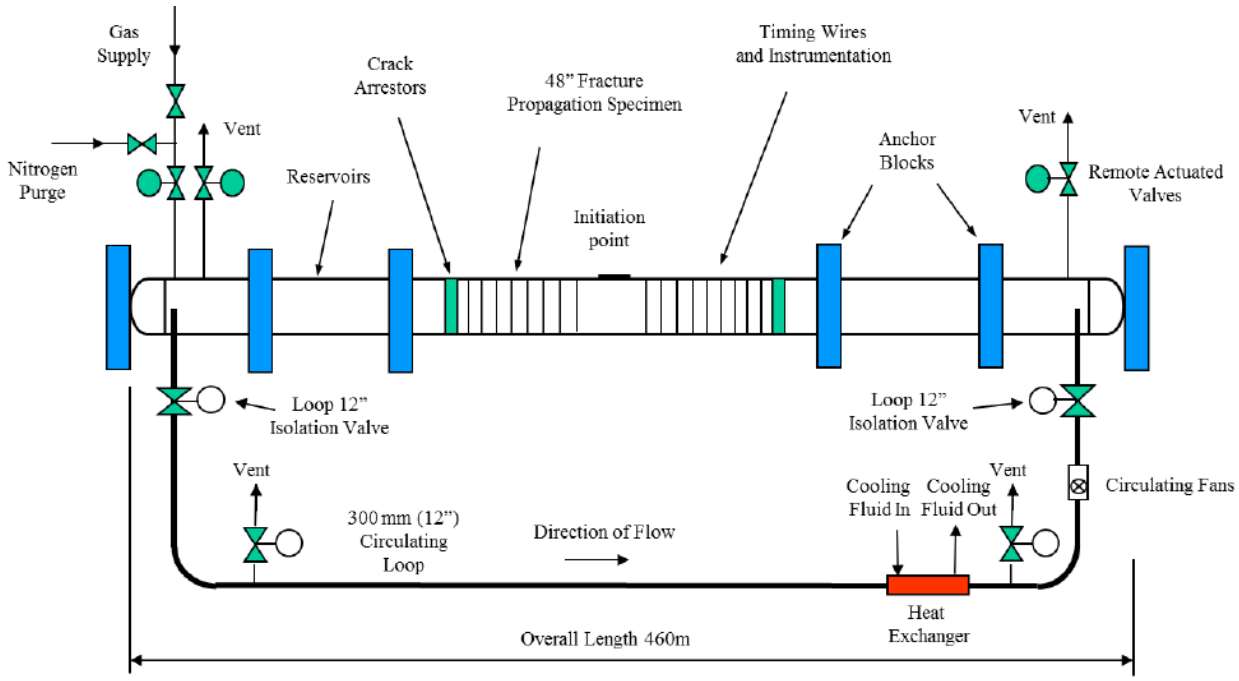

Figure 3-2 Simplified diagram of test setup

Figure 3-3 Installation of insulated recirculating loop

The circulating loop incorporated injection for precisely metering various test gases (propane, butane, pentane, hexane and carbon dioxide) into the rig which contained a base natural gas content derived from an LNG source which provided the methane, ethane and nitrogen components of the test gas. This set-up facilitated continuous monitoring and controlling the gas composition. The gas filling procedure ensured that

throughout the filling process the gas mixture remained gaseous and did not enter the phase envelope where liquids could be formed. This was confirmed by gas sampling and monitoring of the test rig pressure and temperature throughout the filling process and confirming the state of the mixture using DNV's thermodynamic software GASVLE (108). The circulation of the test gas ensured compositional uniformity throughout the test rig and by taking gas samples from close to the top and bottom of the test pipe it was confirmed that there was no gas stratification.

To prevent reservoir movement during a test, both reservoirs were installed within large concrete anchors (see Figure 3-4). Four anchors were equally spaced along each reservoir to resist any bending forces applied during the test and one at each end supported by steel piles. The reservoirs were also protected at their inner ends by crack arrestors (Figure 3-5), in the event that the fracture failed to arrest within the test section.

Figure 3-4 Photograph shownng the top of concrete anchors installed around the reservoir

Figure 3-5 Photograph showning a crack arrestor installed on the reservoir section

The test section was constructed from pipe lengths ranging from 11.4 m to 11.6 m and were instrumented by DNV prior to welding. For each pipe length the longitudinal seam weld was located 10˚ from the bottom dead centre and for consecutive pipe lengths the seam weld was located alternately to the north then the south of pipe bottom dead centre. The seam welds were positioned at the bottom of the test section to minimise the chance of the fracture initiated on the top of the pipe coinciding with any of the test pipe seam welds. The welding of the test pipe girth welds was performed in accordance with welding Standards. Non Destructive Testing (NDT) of the butt welds consisted of 100% radiography, ultrasonic examination and magnetic particle inspection, and any unacceptable defects were repaired to a qualified procedure.

The pipes in the test section were referenced as 1E to 5E in the easterly direction and similarly 1W to 5W in the westerly direction.

The test was initiated using a 1 m long explosive cutting charge in the centre of the initiation pipe.

The test facility was instrumented with pressure transducers and thermocouples to measure the gas pressure, test pipe wall temperature and gas temperature prior to initiation of the test. Timing wires and pressure transmitters were used to measure the crack growth and gas decompression during the test. Bi-axial strain gauges were also installed to measure the circumferential and longitudinal strain to provide a

measurement of the strain field in front of the fracture on each pipe. Normal and High-Speed Video cameras were also deployed.

On completion of the test section construction the test facility was hydrostatically pressure tested to 170 bar. The test pressure was held for 2 hours and during this period the pressure dropped less than 1 bar. Following the hydrostatic test the test section was insulated using 50 mm of polyurethane foam.

After the fan casing had been installed, the test rig was pressurised pneumatically (using nitrogen) to enable the fan casing flanged joints to be checked for gas tightness using leak detection fluid. The fan casing flanged joints were the only connections broken post hydrostatic pressure test. The fan casing was subjected to a separate pneumatic pressure test prior to connection to the test rig. The test section was subsequently pneumatically pressure tested using nitrogen and all accessible connections checked for gas tightness using leak detection fluid. Prior to testing the test section, instrument and cable locations were covered with a layer of sand padding and then backfilled with indigenous clay type soil so that the top of the test pipes was 0.9 m below ground level. A schematic of the test facility is shown in Figure 3-6.

A photo of the eastern end of the test section before being backfilled is shown in Figure 3-8.

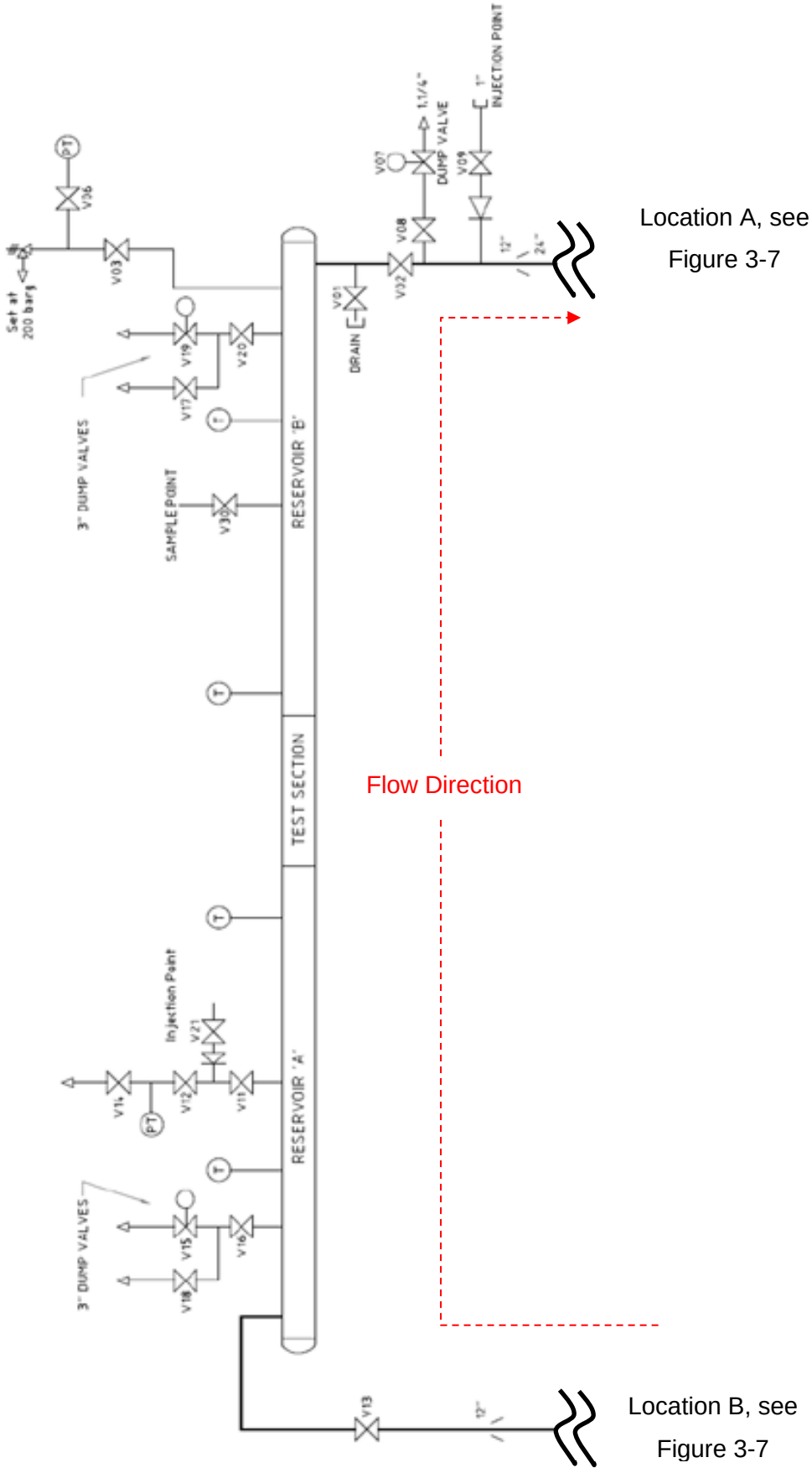

Figure 3-6 Schematic of test loop (see also Figure 3-7). Not to scale

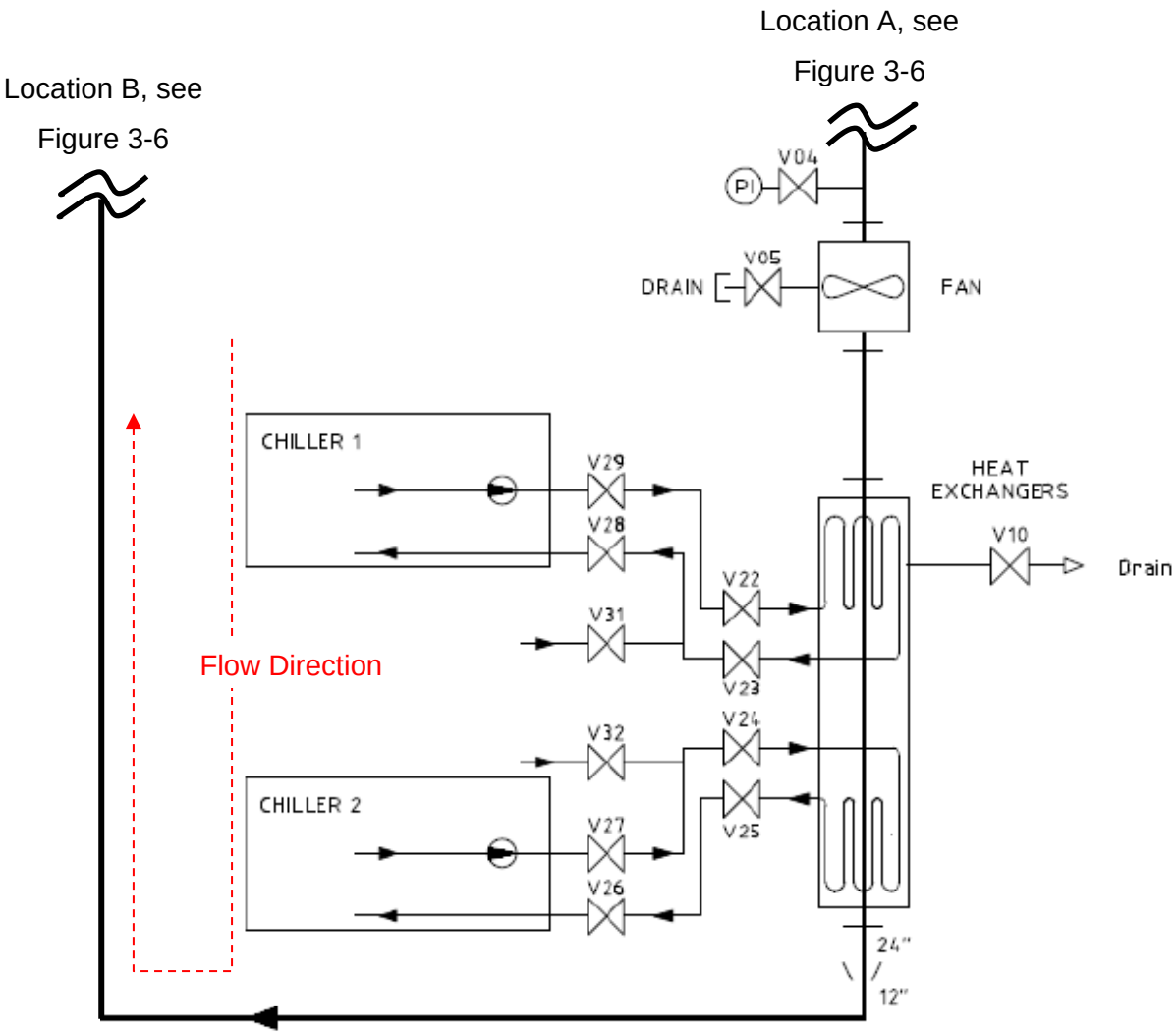

Figure 3-7 Schematic of test loop (see also Figure 3-6). Not to scale

Figure 3-8 Eastern test section before being backfilled

3.1.2.1. Procedure

The following procedure was completed by the DNV Spadeadam site team. After completion of all construction and pressure testing activities the instrumentation was connected to two forward recording suites located close to the test rig (one for each side) where the data logging systems were installed. Each forward recording suite was reinforced with heavy steel cladding and bunkered with earth mounds to protect them from impact damage from the subsequent test. After confirmation that all instruments were operational the pipes were then backfilled to a depth of 0.9 m from the top of the test pipes with indigenous clay type soil. The backfill was carefully compacted with a bulldozer, without risking damage to the test section instrumentation, to achieve as closely as possible the restraint conditions typical of a buried pipeline.

To ensure that at no point during filling did the gas enter the two phase envelope, a calculated mass of each gas was measured into the test rig at the appropriate stage in the fill procedure. To determine that the actual and theoretical compositions were in agreement before the next stage of filling progressed, the gas mixture within the test rig was sampled and analysed using a gas chromatograph.

The fracture was initiated using an explosive linear shaped charge positioned on the pipeline top-dead-centre, mid length along the initiation pipe. The length of this charge was 1 m and was significantly longer than the predicted critical through-wall crack length of the test section material to ensure the crack would propagate. A pre-test trial was carried out to prove the size of the explosive charge to ensure a through-wall cut.

Although there was a high probability that ignition of the test gas on initiation would occur, ignition sources such as roman candles were also deployed at both a high and low level to ensure ignition did occur.

The operation and control of the test facility was achieved using a combination of manual and remotely actuated valves. The pressure and temperature sensors installed on the reservoirs were continuously monitored to provide information on the gas pressure and temperature during filling prior to the test using an imc SPARTAN data acquisition system located in forward recording suites, where logging of all scientific instrumentation took place. The control room was a blast proof building approximately 400 m west of the test area. The test pressure (134 bar) was measured using a calibrated dead weight gauge.

The test gas required cooling due to the increased temperature generated by compressing the test gas into the test rig and the heat energy generated by the fan units while circulating the test gas during mixing. To achieve the test temperature the

test gas was circulated using the test loop fan units through the shell of the heat exchanger and test rig while a cold ethylene glycol/water mix was circulated through the heat exchanger tubes. Once the test temperature was achieved on the day of the test the circulating fans and refrigeration units were stopped and the heat exchanger drained of glycol to protect against the risk of damage and any subsequent spillage. The two 12 inch (300 mm) isolation valves at each end of the circulating loop were closed prior to test initiation to isolate the loop contents and prevent it from decompressing into the test rig during the fracture propagation.

Each test reservoir incorporated a 3 inch (75 mm) diameter actuated blow down valve that could be operated remotely from the control room. These valves were required as emergency vents. The 12 inch nominal bore (323 mm) circulation loop was fitted with a 1.1/4 inch (32 mm) actuated vent valve to allow the circulating loop contents to be vented post-test before personnel were permitted to approach and make the area safe.

Once all pre-test checks were complete and camera views set, the explosive charge was fitted to the initiation pipe and test conditions confirmed. The fracture propagation test was then initiated by firing the explosive charge.

3.1.2.2. Instrumentation

Figure 3-9 details the layout of the instrumentation installed on the fracture propagation test section to measure the fracture speed, gas decompression behaviour and strain field. Table 3-1 detail the axial location of all the instrumentation deployed on the test section.

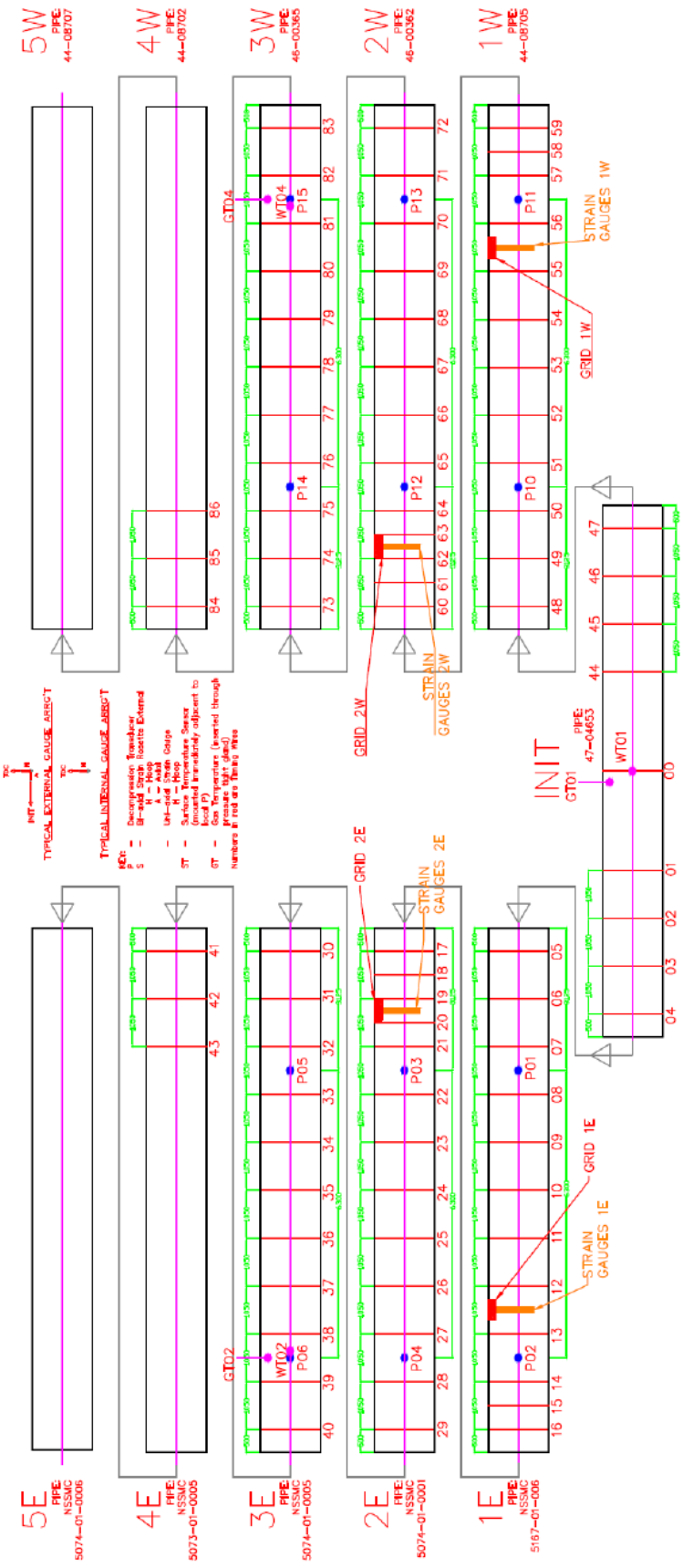

Figure 3-9 Instrumentation layout on test section

Table 3-1 Location of instrumentation on eastern section

Location	Axial distance from centre line from INIT (m)	Location	Axial distance from centre line from INIT (m)
WT01	0.00	TW24	23.05
TW01	2.15	TW25	24.10
GT01	1.15	TW26	25.15
TW02	3.19	TW27	26.20
TW03	4.24	P04	26.73
TW04	5.29	TW28	27.25
WELD Init/1E	5.79	TW29	28.30
TW05	6.28	WELD 2E/3E	28.73
TW06	7.33	TW30	29.22
TW07	8.38	TW31	30.27
P01	8.91	TW32	31.32
TW08	9.43	P05	31.86
TW09	10.47	TW33	32.37
TW10	11.51	TW34	33.42
TW11	12.56	TW35	34.47
TW12	13.61	TW36	35.52
Grid 1E Front	13.96	TW37	36.57
E1_S01 to S08	14.19	TW38	37.62
TW13	14.66	WT02	37.94
P02	15.21	P06	38.15
TW14	15.70	GT02	38.42
TW15	16.23	TW39	38.68
TW16	16.75	TW40	39.73
WELD 1E/2E	17.31	WELD 3E/$£	40.25
TW17	17.81	TW41	40.73
TW18	18.33	TW42	41.78
TW19	18.85	TW43	42.83
Grid 2E Front	18.90	WELD 4E/5E	51.78
E2_S01 to S08	19.12	WELD 5E/Res.E	63.31
TW20	19.38	Gas sampling Point	68.83
TW21	19.91	P07	69.38
P03	20.41	P08	99.38
TW22	20.95	P09/WT03	139.38
TW23	22.00	GT03	226.05

Key

TW = timing wire, GRID =Scribed Grid, S = Strain Gauge, P = Pressure gauge, WT = Wall temperature, GT = Gas temperature.

Highlighted section are items located on the reservoir.

Table 3-2 Location of instrumentation on western section

Location	Axial distance from centre line (m)	Location	Axial distance from centre line (m)
TW44	-2.15	TW69	-25.21
TW45	-2.20	TW70	-26.27
TW46	-4.25	P13	-26.80
TW47	-5.30	TW71	-27.32
WELD Init/1W	-5.79	TW72	-28.37
TW48	-6.29	WELD 2W/3W	-28.90
TW49	-7.34	TW73	-29.40
TW50	-8.39	TW74	-30.45
P10	-8.93	TW75	-31.50
TW51	-9.44	P14	-32.03
TW52	-10.50	TW76	-32.55
TW53	-11.54	TW77	-33.61
TW54	-12.59	TW78	-34.66
TW61	-13.37	TW79	-35.70
TW55	-13.64	TW80	-36.75
Grid 1W Front	-14.01	TW81	-37.81
W1_S01 to S08	-14.24	WT04	-38.15
TW56	-14.69	P15	-38.32
P11	-15.23	GT04	-38.58
TW57	-15.74	TW82	-38.86
TW58	-16.27	TW83	-39.91
TW59	-16.79	WELD 3W/4W	-40.44
WELD 1W/2W	-17.36	TW84	-40.94
TW60	-17.86	TW85	-41.99
TW62	-18.91	TW86	-43.04
Grid 2W Front	-18.95	WELD 4W/5W	-52.02
W2_S01 to S08	-19.17	WELD 5W/Sec. W	-63.62
TW63	-19.44	WELD Sec. W/Res. W	-66.57
TW64	-19.96	GT05	-71.02
P12	-20.51	P16	-71.37
TW65	-21.01	P17	-103.01
TW66	-22.06	P18/WT05	-143.01
TW67	-23.11	GT06	-226.28
TW68	-24.16		

Key

TW = timing wire, GRID =Scribed Grid, S = Strain Gauge, P = Pressure gauge, WT = Wall temperature, GT = Gas temperature.

Highlighted section are items located on the reservoir.

3.1.2.3. Co-ordinate System

The co-ordinate system used to describe the location of instrumentation on the test arrangement is based on an origin of top dead centre on the middle of the initiation pipe. The X-axis is taken to be along the top dead centre of the pipe in an easterly direction (negative values for westerly direction).

The circumferential location of instruments fitted to the pipes is given as the angle from top dead centre (TDC) to the north or south side.

The data acquisition systems used for the test were started at the time that a break-wire was broken by the explosive charge and this provides a 'time zero' (T0) for the logging systems.

3.1.2.4. Gas decompression

The decompression of the test gas was measured at 18 locations on the fracture propagation test facility with 0-250 bar WIKA S-11 Series Pressure Transducers. These transducers are based upon a fully active four arm Wheatstone bridge, the whole instrument having a quoted accuracy of ±0.2% of full scale range. The transducers have a silicone oil filled diaphragm to allow a measurement flush to the pipe wall to be made. Prior to installation into the test rig, each transducer was calibrated using a pressure standard traceable to national standards. These transducers have been demonstrated to give a maximum response rate in excess of 17 bar m^{-1} s^{-1} calculated over a 10 bar decrease in applied pressure.

The test section had 12 decompression transmitters located along its length with two on each of the test pipes 1E, 2E, 3E, 1W, 2W and 3W. A further three decompression transmitters were located on each test reservoir. On the test section, the transmitters were located at 90° from the top of the pipe to the north side and on the test reservoirs they were positioned on the top dead centre of the pipes. These instruments were fitted to threaded bosses welded through the pipe wall to ensure the transducer diaphragms were flush with the inner surface.

The data from these instruments were logged at a rate of 50 kHz on a transient recorder and also on a backup data recorder. A number of pressure levels have been selected and, at each transmitter location, the time that the pressure has decayed to each of these levels has been identified. This enables the speed of travel of each pressure level between successive transmitters to be determined and a plot to be derived of pressure level against the velocity for that pressure level.

3.1.2.5. Test Rig Pressure

The gas pressure measurements prior to test initiation were taken at two locations; one on each test reservoir close to the reservoir dome end. The type of measuring device used was a Druck pressure transmitter type PTX 610 series with a gauge pressure range of 0 to 400 bar and a quoted accuracy of ±0.08% of full scale range. These were directly mounted onto a valve on a ½ inch (12.7 mm) boss on top of the east reservoir and directly to a valve on a ½ inch (12.7 mm) boss on top of the 12 inch nominal bore (323 mm) circulating loop connection at the west end. The two tests were both carried out at 134 bar.

The pressure transducers were calibrated for static pressure measurement traceable to national standards prior to the commencement of the experimental programme.

Gas pressure measurements were logged on the imc SPARTAN data acquisition system at a rate of 10 Hz in the forward recording suites during pressurisation and during the experiment.

3.1.2.6. Gas Temperature

Fluid temperature measurements were made at six locations: one in each of pipes INIT, 3E and 3W, one in the east reservoir close to the domed end and two in the west reservoir (one at the front, near the decompression transducer and one at the rear near the domed end). The type of instrument used was a 6 mm diameter, stainless steel sheathed, mineral insulated Type 'A' platinum resistance thermometer and were inserted approximately 100 mm into the bore of the pipe through pressure retaining glands. The measuring range of these thermometers was -100 °C to +100 °C with an accuracy of better than ±0.3 °C.

The thermometers installed in the test section were installed at 90° to the top of the pipe on the north side. Those installed on the reservoirs were installed on the top-dead-centre of the pipe.

The fluid temperature measurements were logged on the imc SPARTAN data acquisition system at a rate of 10 Hz in the forward recording suites during pressurisation and during the experiment.

Figure 3-10 Test loop with chillers installed prior to test

3.1.2.7. Wall Temperature

The pipeline wall temperature measurements were made at three locations on the test section on pipes INIT, 3E and 3W and at a further 1 location on each reservoir, near to the domed end. Type 'A' platinum resistance thermometers were used, with each being bonded to the pipe wall and then sealed with a neoprene rubber and aluminium foil coating to insulate the thermometer from the surrounding environment and provide protection against moisture. The measuring range of these thermometers was -100 °C to +100 °C with an accuracy of better than ±0.3 °C.

The pipeline wall temperature measurements were logged on an imc SPARTAN data acquisition system in the control room from the time of test rig pressurisation to test completion.

3.1.2.8. Strain Measurements

The strain measurements on the exterior of the pipe wall were made using 32 bi-axial strain gauge rosettes at 8 locations on each of test pipes 1E, 2E, 1W and 2W. The strain gauge rosettes on each of these pipes were located at a single axial location. The rosettes were located at circumferential positions of 10, 20 and 45 degrees to the north and 10, 20, 45, 90 and 135 degrees to the south of TDC at each axial location.

In addition to the external strain gauge rosettes, single axis strain gauges were installed internally at matching locations to each of the external rosettes. Each of the internal single-axis gauges was oriented to measure strain in the hoop direction. The connecting cables for the internal gauges were passed through the pipe wall using a high pressure feed-through assembly.

The external bi-axial rosette at each of the 8 locations on each pipe is numbered S01 to S08 prefixed with the pipe number. Each gauge at the location is then suffixed with an “H” or “A” designation corresponding to the Hoop and Axial oriented gauges respectively. This nomenclature is further suffixed by an “E” or and “I” corresponding to External and Internal respectively.

Electric resistance strain gauges, manufactured by HBM were used and had a measuring range of up to 30,000 micro-strain. The gauges were chemically bonded to the external and internal surfaces of the test section pipes and then protected by a silicone based sealant. Each gauge was connected to a full bridge completion unit located on the pipe to reduce the potential for noise in the signals.

The strain data recorded was accurate to within ±10% of the reading.

3.1.2.9. Fracture Arrival Time

The time of arrival of the fracture in each direction from the centre of the test section was determined using timing wires fitted around the external surface of the pipe. The wires were waterproofed and coated to protect them against mechanical and environmental damage. There were a total of 86 timing wires installed on the test section. Wires were generally spaced at 1.05 m intervals except either side of weld 1E/2E and weld 1W/2W where the pipe wall thickness changed.

An additional eight timing wires were fitted to the initiation pipe at 0.5 m, 1.55 m, 2.6 m and 3.65 m from each end of the pipe.

The time each timing wire broke during the test was determined using the voltage-time data. The accuracy on the time each wire broke is better than ±0.2 ms based nominally on the decay time for the electrical circuitry to discharge to earth after a breakage. The data was logged at a rate of 50 kHz on a National Instruments Compact DAQ system.

3.1.2.10. Gas Composition

The test rig had sample points located close to the east end of the test section, these sample points enabled gas samples to be taken from the top, bottom and middle of the test pipe. The gas samples were taken into a gas sampling cylinder through a heated sample tube to avoid condensing any of the heavier components due to the Joule

Thompson effect arising from the drop in pressure compounded by the sub-zero temperature of the test gas. The collected samples were then analysed using a gas chromatograph calibrated against a certified gas mixture with a composition matching the proposed test gas. The unit was calibrated every morning during gas filling and prior to analysing the test day samples.

3.1.2.11. Thermal Radiation

To measure thermal flux experimentally, radiometers are available which use a sensor which is connected to a heat sink. As the sensor and heat sink are at different temperatures, a transfer of heat will take place which is a function of the net flux being absorbed. These form a differential thermoelectric circuit, providing an electromagnetic field (EMF) between the two output leads which is directly proportional to the incident thermal radiation.

The thermal radiation resulting from the subsequent fireball was measured using an array of Medtherm wide angle radiometers (total field of view of 150˚) distributed around the test area. In the north-south direction (nominally crosswind from the prevailing wind direction), radiometers were placed at distances of 200 m and 500 m north of the initiation point. On the east-west axis, radiometers were placed at 200 m and 500 m west of the initiation point and distances of 200 m, 500 m, 750 m and 1000 m east of the initiation point. A diagram showing the locations and nomenclature for the radiometers is shown in Figure 3-11. The radiometers have a response time of 1 s and an accuracy of ±5% and were calibrated prior to testing in a black body furnace over five different heat fluxes. A photograph of a radiometer set up is shown in Figure 3-12.

The wide-angle radiometers, manufactured by Medtherm Corporation, have a total field of view of 150°. Each Medtherm radiometer is fitted with a calcium fluoride window that transmits light in the wavelength range 0.3 to 11.5μm and employs a Schmidt-Boelter thermopile to measure incident thermal radiation. Incident thermal radiation is absorbed at the sensor surface and transferred to an integral heat sink that remains at a temperature below that of the sensor surface. The difference in temperature between two points along the path of the heat flow from the sensor to the sink is proportional to the heat being transferred, and is, therefore, proportional to the incident thermal radiation. Medtherm radiometers have thermocouple junctions fitted at two such points. These form a differential thermoelectric circuit, providing an EMF between the two output leads which is directly proportional to the incident thermal radiation. The radiometers will be aimed at the nominal predicted centre of the fireball.

Each of the thermal radiation measurements will be recorded at a rate of at least 2 Hz on an imc SPARTAN data acquisition device.

The thermal radiation measurements were logged on the imc SPARTAN data acquisition system at a rate of 10 Hz in the forward recording suites during pressurisation and during the experiment.

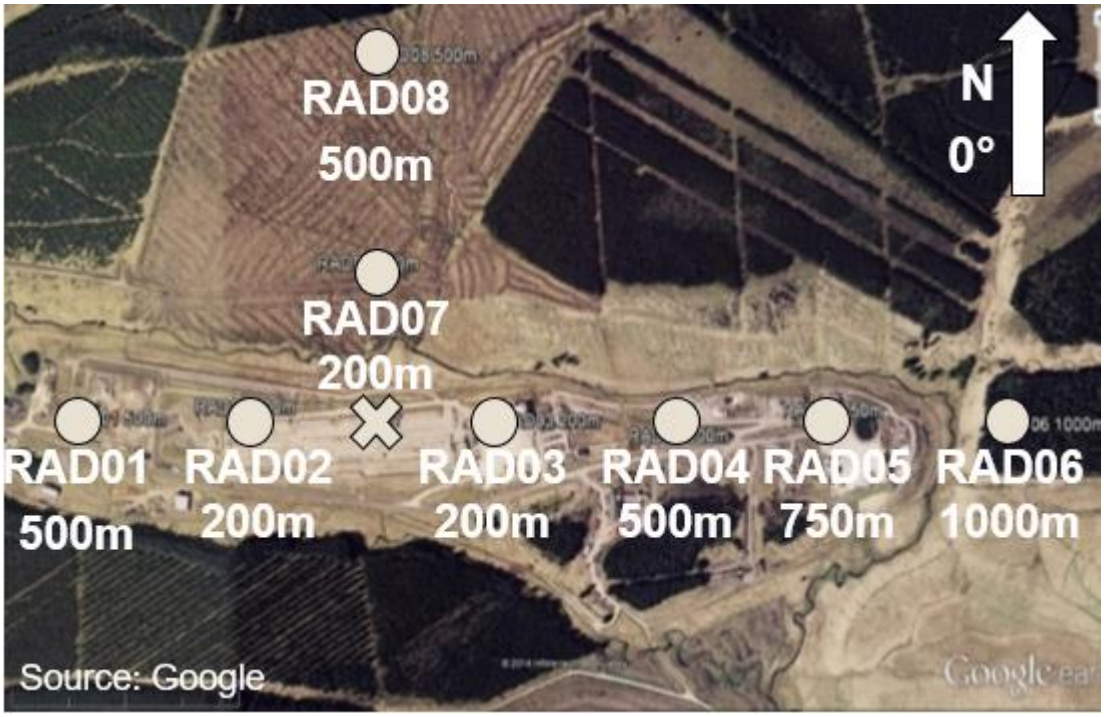

Figure 3-11 Radiometer locations.

Figure 3-12 Radiometer Sensor Setup

3.1.2.12. Free field Overpressure

The free-field overpressure produced during the first test was measured at 8 locations on the test area using PCB 113B21 high frequency response pressure transducers. The transducers had a resonant frequency of greater than 500 kHz and a non-linearity quoted by the manufacturer of <0.1% full scale range (~14 bar (200 psi)).

The transducers were fitted to aerodynamic discs and mounted vertically side on to the anticipated direction of the pressure wave at a local height of nominally 1.25 m. Each of these sensors is calibrated onsite annually for dynamic response. The locations of the free field overpressure sensors are shown in Figure 3-13. A photograph of a mounted overpressure transducer is shown in Figure 3-14.

The data from these instruments were logged at a rate of 50 kHz on a transient recorder and also on a backup data recorder.

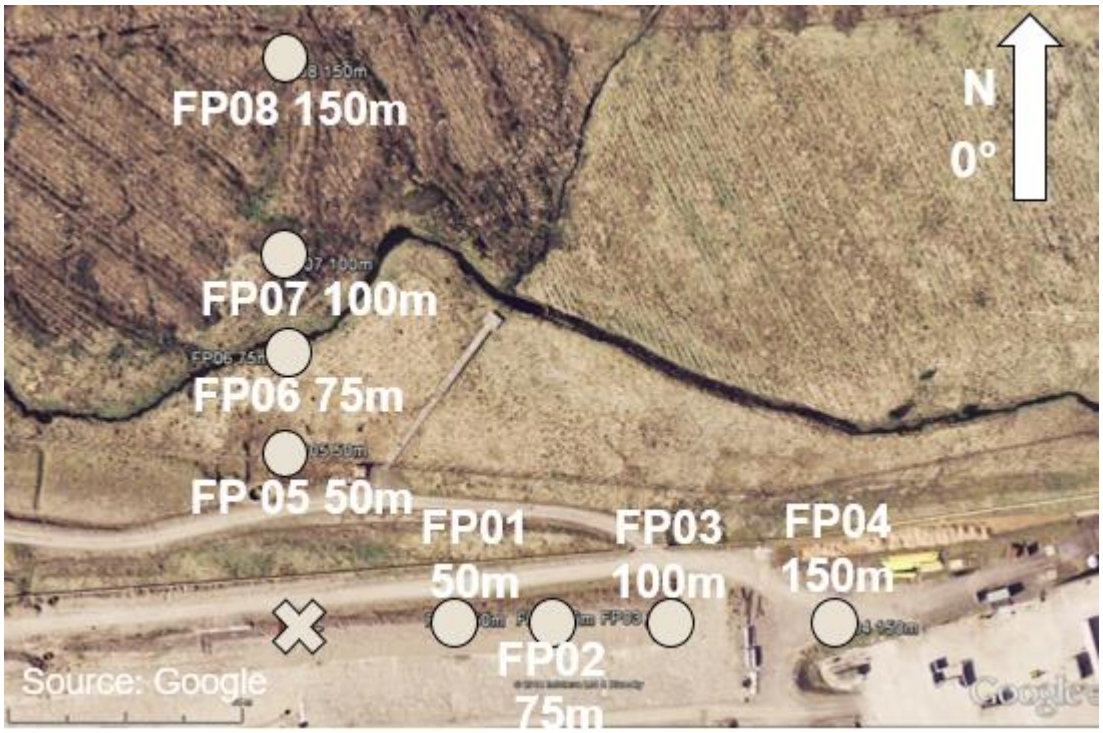

Figure 3-13 Overpressure locations

Figure 3-14 Overpressure Sensor Setup

3.1.2.13. Atmospheric Conditions

The wind speed and direction was monitored at one location close to the control room (approximately 450m to the west of the initiation point) and logged prior to and during the test on an imc SPARTAN data acquisition system. The measurements were made using two Gill WindSonic sonic anemometers providing wind speed and direction from a single instrument. One instrument was placed at 5 m from the local ground level while the other was placed at 10 m from the local ground level. Both instruments were oriented such that a wind direction travelling from Ordnance Survey Great Britain (OSGB) Grid North was reported as a wind bearing of 0°, 270° indicating a wind travelling from due west of the instrument.

The atmospheric condition measurements were logged on the imc SPARTAN data acquisition system at a rate of 10 Hz in the forward recording suites during pressurisation and during the experiment.

3.1.2.14. Video Records

To record the test video cameras and high-speed video cameras were deployed at elevated positions to provide near field views of the test (see Figure 3-15).

Figure 3-15 Near Field Camera locations

Far field camera locations for tests 1 and 2 were also employed by the author and these locations are given in Figure 3-16.

Figure 3-16 Far field video camera locations

Measurement of fireball sizes from camera images can be made using knowledge of the focal length. The focal length (49) of camera is defined by:

$$\frac{1}{f_l} = \frac{1}{s'} + \frac{1}{s} \qquad \textbf{(3-1)}$$

Where:

f_l = focal length

s = distance from lens to object

s' = distance from lens to image

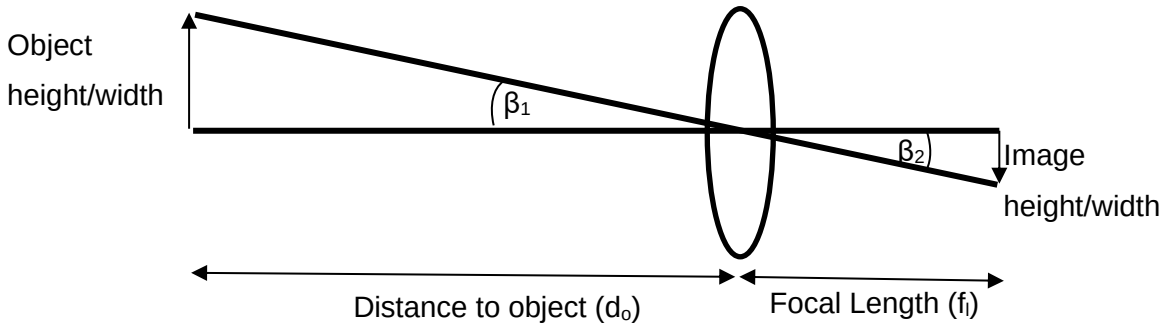

Figure 3-17 Schematic of focal length and object distance

Using the focal length and similar triangles, a relationship between object height/width and image height width can be obtained as β_1 is equal to β_2. Therefore:

$$\tan(\beta) = \frac{Object\ height/width}{d_o} = \frac{Image\ height/width}{f_l} \quad \textbf{(3-2)}$$

Can be rearranged to:

$$\text{Object height/width} = \frac{Image\ height/width}{f_l}\, x\ d_o \quad \textbf{(3-3)}$$

In practice, the distance to the fireball would be the value used, but for this experimental work, the known value is the distance to the point of initiation. It's important to acknowledge that factors such as wind and release dynamics could impact the fireball's position. Consequently, the calculated fireball diameter would be overestimated. For instance, with an actual fireball diameter of 200 m and a 1 km distance from the fireball, this overprediction would be 10%. Notably, if the wind or the fireball is situated farther from the point of measurement, the margin of error would decrease. The image height can be calculated by using the sensor size of the camera, the total number of length/width pixels and number of length/width pixels taken up by the image.

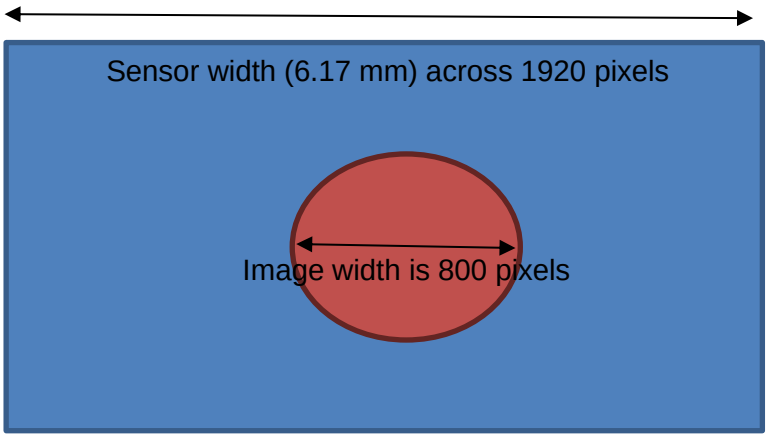

Figure 3-18 Example of object width calculation based on image size

Using the values given in Figure 3-18, gives an image width of 2.57 mm (800/1920 x 6.17). Assuming a focal length of 4.5 mm and distance to object of 1 km, gives an object width of 0.57 km or 570 m.

3.1.2.15. Experimental Error

The accuracy of equipment used for the large scale experiments has been listed in the preceding sections. In summary:

- Pressure transducers measuring the decompression had an error of +/-0.2%.
- Pressure transducers measuring the rig pressure had an error of +/-0.08%.
- Strain gauge measurement were subject to an error ±10%.
- The radiometers had an error of ±10%.
- Pressure transducers measuring the free field overpressure had a quoted error of <0.1%.

3.2. Modelling Transient Heat Flux Tests at Laboratory Scale

Using the thermal radiation results from the large scale tests, the cone calorimeter at the University of Leeds was adapted to expose samples to the equivalent thermal radiation exposure at laboratory scale, so that conditions and tested quickly providing additional data to supplement the large scale tests and investigate additional scenarios.

3.2.1. University of Leeds Cone Calorimeter

The University of Leeds cone calorimeter is the standardised version, purchased from FTT (Fire Testing Technology Ltd.).

The standard cone calorimeter, is a popular bench scale tool in fire flammability testing of materials (109). It utilises a truncated conical radiant heater (electrical coil) to apply a controlled heat flux, typically from 0 to 100 kW m^{-2}, to a standardized sample size,

usually 100 mm x 100 mm (5 to 50 mm thick) mounted at a fixed distance below the heater. The standard calorimeter's key features include, measuring critical heat fluxes for ignition, the time to ignition when exposed to fixed heat flux, the heat release rate, which is determined by analysing oxygen consumption during combustion, monitoring the mass loss rate during burning using a load cell. It also quantifies smoke production via optical systems, allowing for analysis of smoke yield and obscuration. The time to ignition is measured using an electric spark or pilot flame. Additionally, the calorimeter conducts gas analysis, examining the combustion by-products and efficiency.

Figure 3-19 is produced by the manufacturer FTT showing the main components of the standard cone calorimeter.

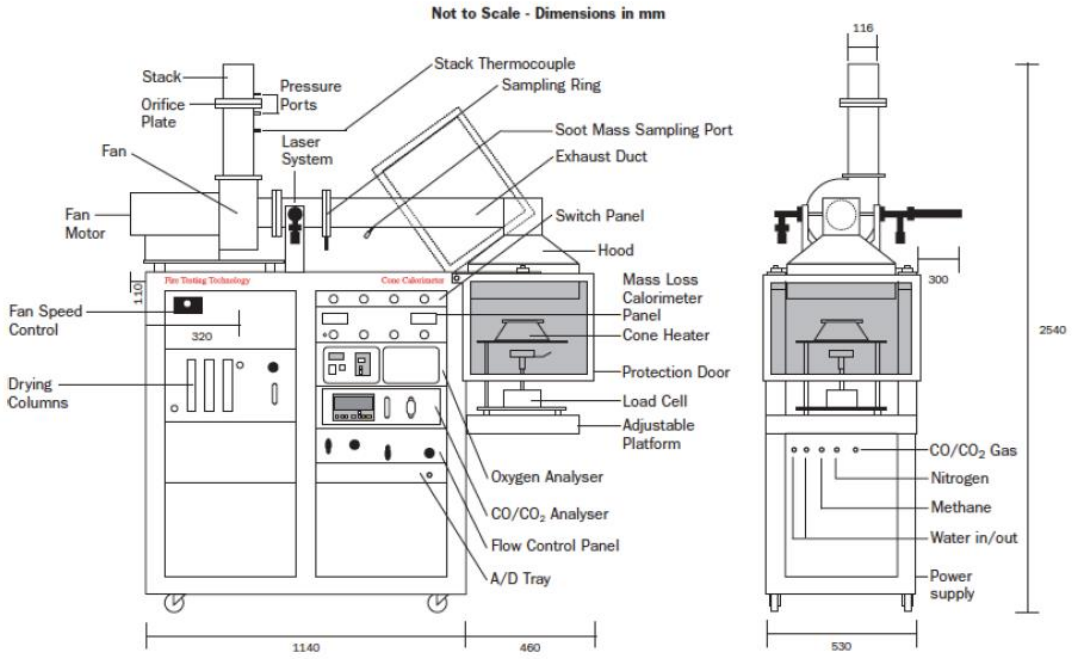

/

Figure 3-19 Schematic of a standard FTT cone calorimeter. Reproduced from (110)

3.2.2. Adapted Cone Calorimeter

For this research the standard cone calorimeter setup was significantly modified and only a fraction of the potential measurements were used. The objective of the modified set up was to reproduce as closely as possible the transient heat flux profile experienced by the ground targets in the large scale tests. A typical heat flux exposure measured by the heat flux meter at ground level at 200 m from the epicentre of the rupture is shown Figure 3-20.

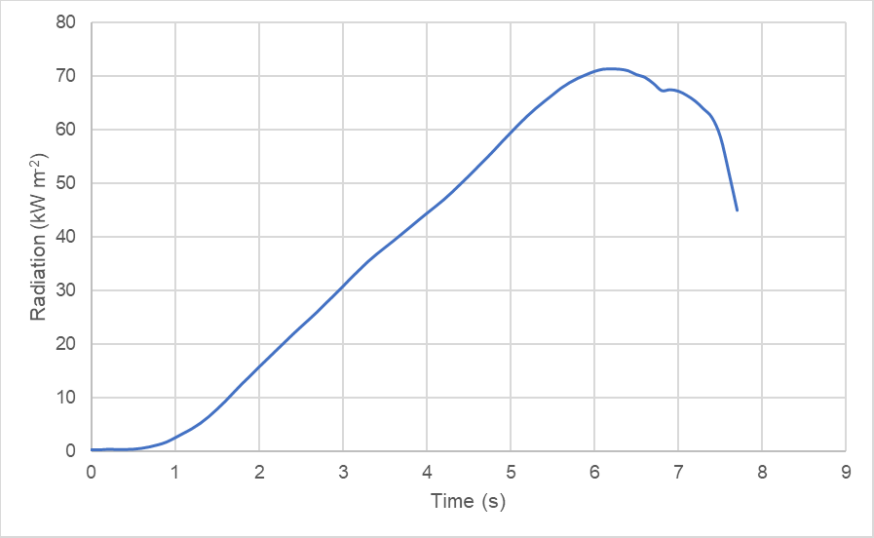

Figure 3-20 Experimental heat flux measured during the large scale test at 200 m (RAD02)

The maximum heat flux recorded in the large scale tests was approximately 70 kW m^{-2} in approximately 6 seconds from the rupture. The incident heat flux then fell back to a few kW m^{-2} in another 6 seconds approximately. At the setting of 930°C, the cone calorimeter emits a constant 70 kW m^{-2} on a sample located 12.5 mm below the heating element. So, the cone calorimeter is capable of producing the maximum value of heat flux observed in the large scale tests. In order to reproduce the increasing exposure from the growing fireball and the subsequent decay, the cone calorimeter fixed position sample holder (see Figure 3-21) was replaced with a vertical actuator. An actuator is a device that produces motion by converting energy and signals into the system.

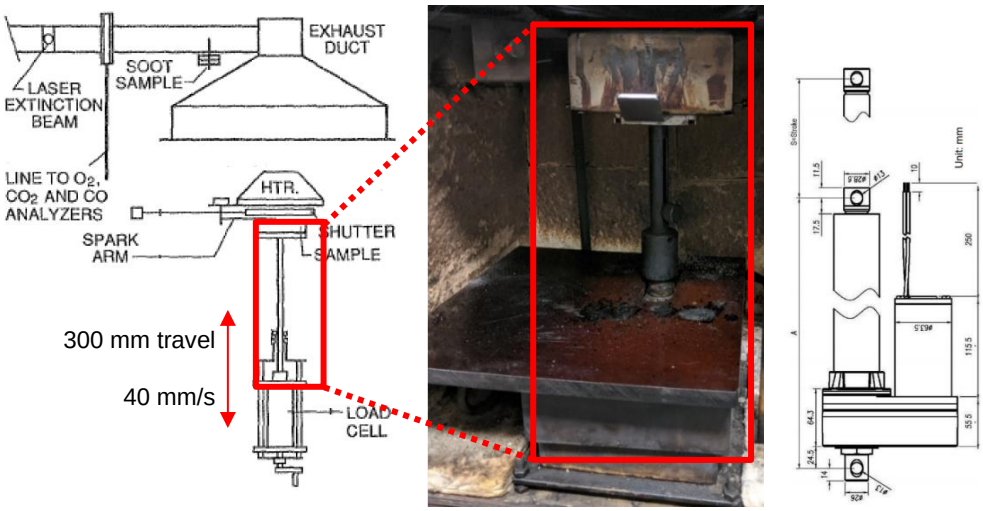

Figure 3-21 Schematic of a standard setup with the load cell element that was replaced with an actuator for the laboratory scale experiments

To determine what specification of actuator was required, the coaxial, parallel squares of different edge length view factor (111) was used to provide an estimate a distance at which the heat flux was small to determine the required length of travel from the cone calorimeter (see Figure 3-22).

Definitions: A = a/c; B = b/a; X = A(1 + B); Y = A(1-B)

Governing equation:

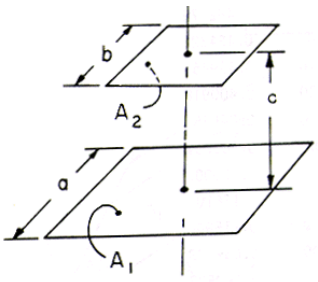

$$F_{1-2} = \frac{1}{\pi A^2}\left\{\ln\frac{\left[A^2\left(1+B^2\right)+2\right]^2}{\left(Y^2+2\right)\left(X^2+2\right)}\right.$$
$$+\left(Y^2+4\right)^{1/2}\left[Y\tan^{-1}\frac{Y}{\left(Y^2+4\right)^{1/2}}-X\tan^{-1}\frac{X}{\left(Y^2+4\right)^{1/2}}\right]$$
$$\left.+\left(X^2+4\right)^{1/2}\left[X\tan^{-1}\frac{X}{\left(X^2+4\right)^{1/2}}-Y\tan^{-1}\frac{Y}{\left(X^2+4\right)^{1/2}}\right]\right\}$$

For A < 0.2 :

$$F_{1-2} = \frac{(AB)^2}{\pi}$$

Figure 3-22 Diagram of view factor and formulae used to determine the laboratory scale setup. Reproduced from (111)

Using values of 0.2 m (diameter of the cone) and 0.1 m (sample length) for a and b respectively the view factor and thermal flux were calculated at different distances from the cone (assumed cone temperature of 930°C and emissivity of 1). Using equation (3-4), at 250 mm the view factor was of 0.041 and thermal radiation flux was 4 kW m^{-2} (i.e. a small heat flux).

$$\ddot{q} = V_f \sigma \varepsilon T^4 \qquad \textbf{(3-4)}$$

The specification of the actuator was selected based on the travel distance of 250 mm and speed of 40 mm s^{-1} (based on a travel time of 6 seconds). The RS PRO Electric Linear Actuator, 24V dc was purchased which was capable of a 305 mm stroke with

variable travel speed of up to 67 mm s^{-1}. It was installed on the cone calorimeter (see Figure 3-23) by University of Leeds' laboratory team so the sample holder was located 252.5 mm from the heating element at its furthest and 12.5 mm at its closest (see Figure 3-24).

Figure 3-23 Photo of the revised setup with the load cell element replaced with an actuator for the laboratory scale experiments

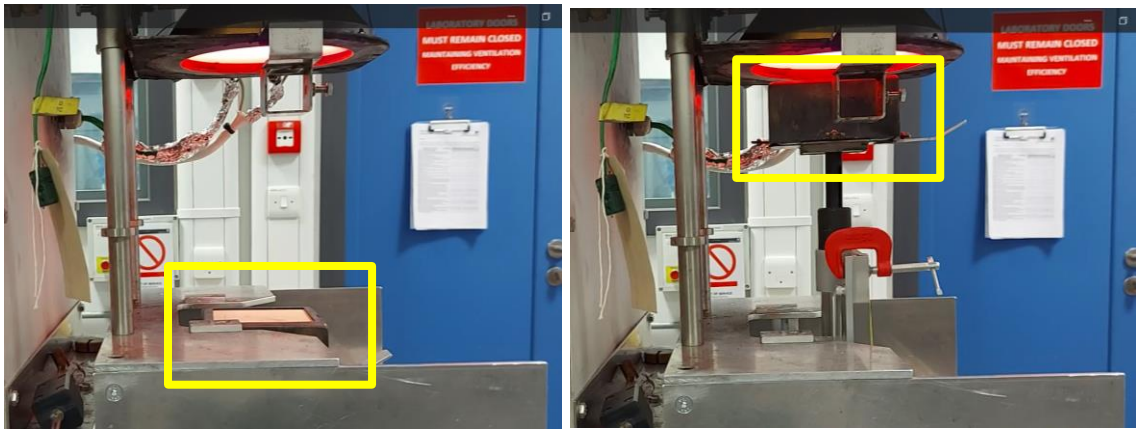

Figure 3-24 Photo of the revised setup with the sample at the base on the left and at the top on the right 6 seconds later

3.2.3. Thermal Radiation Curves for Adapted Cone Calorimeter

For each set of experiments, the setup was calibrated. The basis for the calibration was that at a temperature setting of 630°C, the thermal radiation was 25 kW m^{-2} at a distance of 12.5 mm from the cone as described in the FTT manual (110). Therefore

different temperatures settings lower than 930°C enable equivalent thermal radiation doses at greater distances from the fireball to be represented by the laboratory scale setup. The cone calorimeter is provided with a water-cooled heat flux meter. The heat flux meter can be used to measure the thermal radiation at different points away from the cone for different temperature settings on the cone calorimeter (see Figure 3-25).

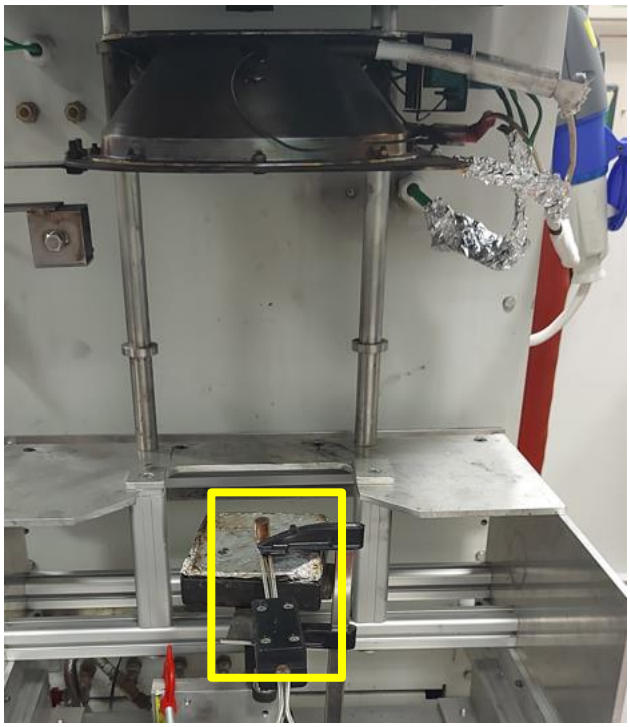

Figure 3-25 Photo showing how a radiometer was used to determine the thermal radiation at fixed positions.

At a distance of 12.5 mm from the cone, the product of the view factor and emissivity using the formula (see Equation (3-5)) given in the FTT manual (110) for a temperature setting of 630°C and thermal flux of 25 kW m^{-2} was 0.67. Similar values were also obtained for higher temperature settings.

$$\varepsilon V_f = \frac{\ddot{q}}{\sigma T^4} \qquad \textbf{(3-5)}$$

The FTT manual states that the product of the view factor and emissivity is required to lie between 0.65 and 0.85. Using the calculated product (0.67) and Equation (3-5), the predicted and observed peak thermal radiation fluxes for different temperature settings at a distance of 12.5 mm from the cone are shown in Figure 3-26.

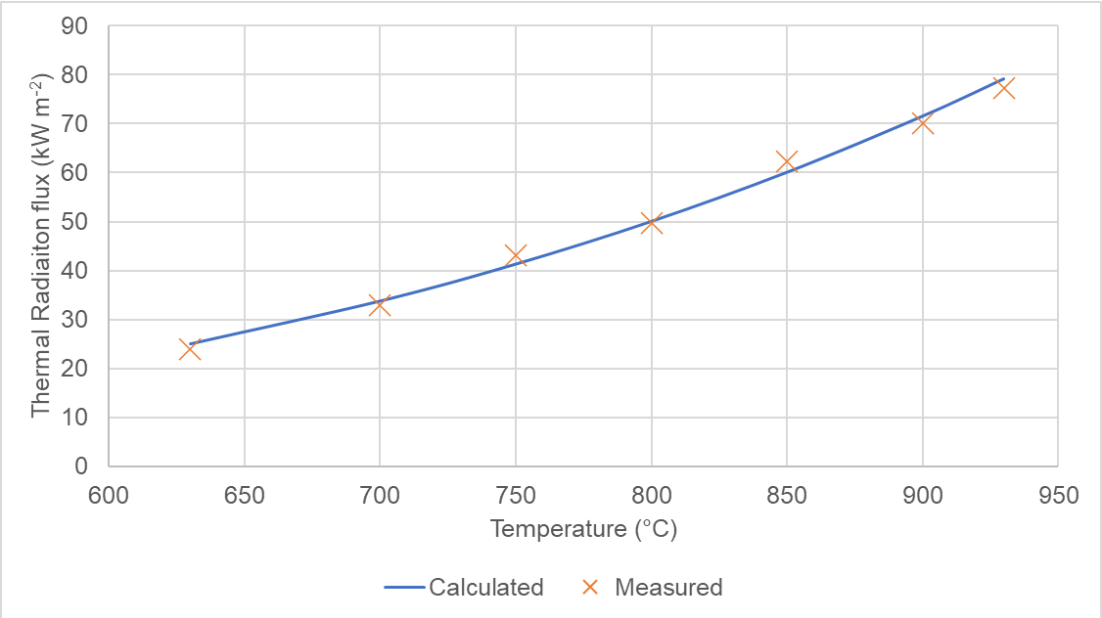

Figure 3-26 Comparison of calculated and peak thermal radiations fluxes for different temperature settings at 12.5 mm from the cone calorimeter

To validate that the laboratory scale setup samples received comparable thermal radiation fluxes at different distances from the cone, a plot of distance from the cone against measured thermal radiation fluxes with equivalent large scale experimental data readings is shown in Figure 3-27. The laboratory and large scale readings in Figure 3-27 have been evaluated in Figure 3-28. The coefficient of determination for all temperatures is in excess of 0.9 demonstrating the laboratory accurately replicates the large scale test data.

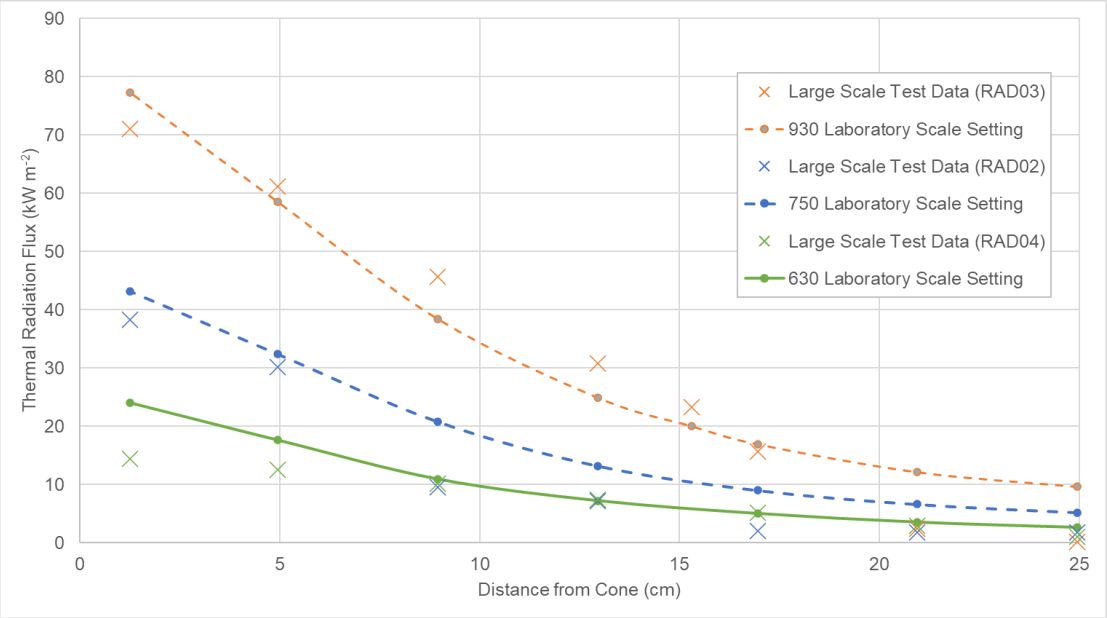

Figure 3-27 Comparison of measured laboratory scale thermal radiations fluxes at different distances from the cone, with equivalent large scale test data

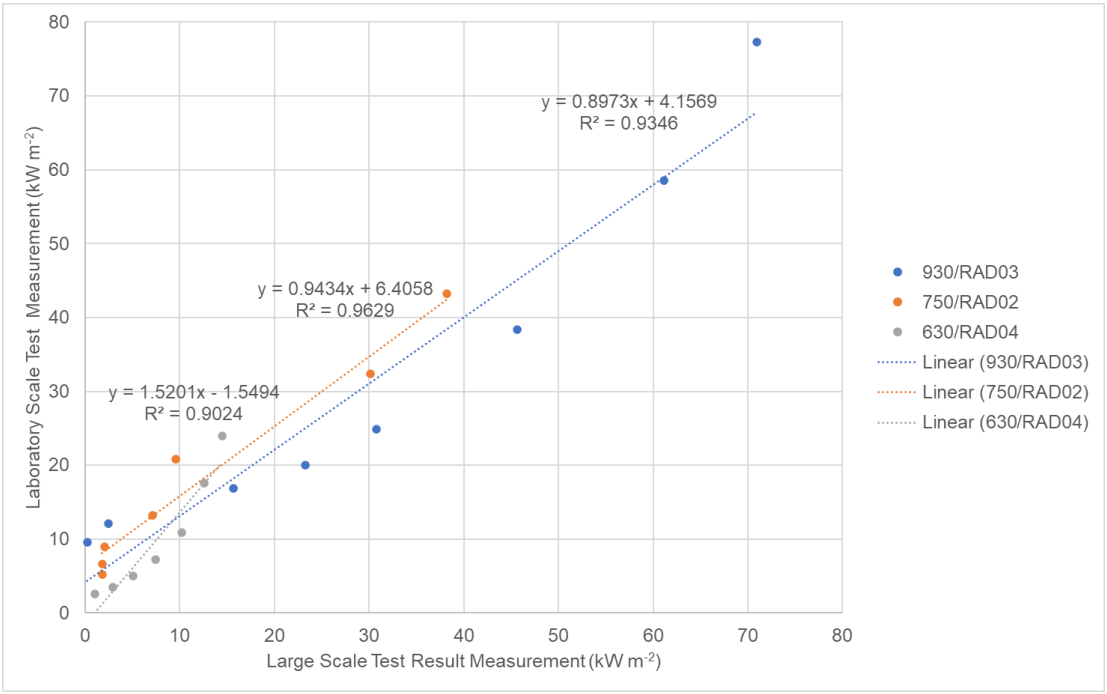

Figure 3-28 Evaluation of measured laboratory scale thermal radiations fluxes for different temperature settings against large test data

The thermal dose exposure was calculated by multiplying the thermal radiation by the time of exposure (carried out at least 1 second time steps to account for the change in thermal radiation). For the calculation of thermal dose, the mid point between two thermal radiation readings was used as shown in Figure 3-29.

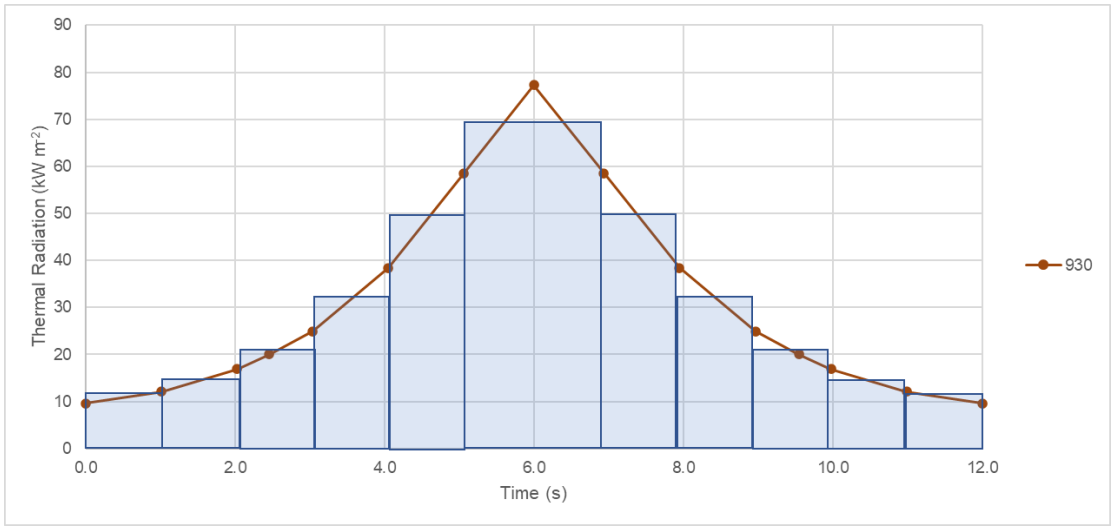

Figure 3-29 Method used to calculate thermal dose from the laboratory scale experiments, example shown for a temperature setting of 930°C

The cumulative thermal dose at the 930°C temperature setting used was compared with the cumulative thermal dose the large scale test data using the radiometer which

recorded the highest heat flux (see Figure 3-30). The radiometer which recorded the highest heat flux was RAD03 with a maximum around 70 kW m^{-2}. The coefficient of determination from this graph shown in Figure 3-30 is 0.97, demonstrating that the laboratory scale accurately replicates the large scale test data for exposure to thermal radiation flux over a time period at the highest recorded heat fluxes.

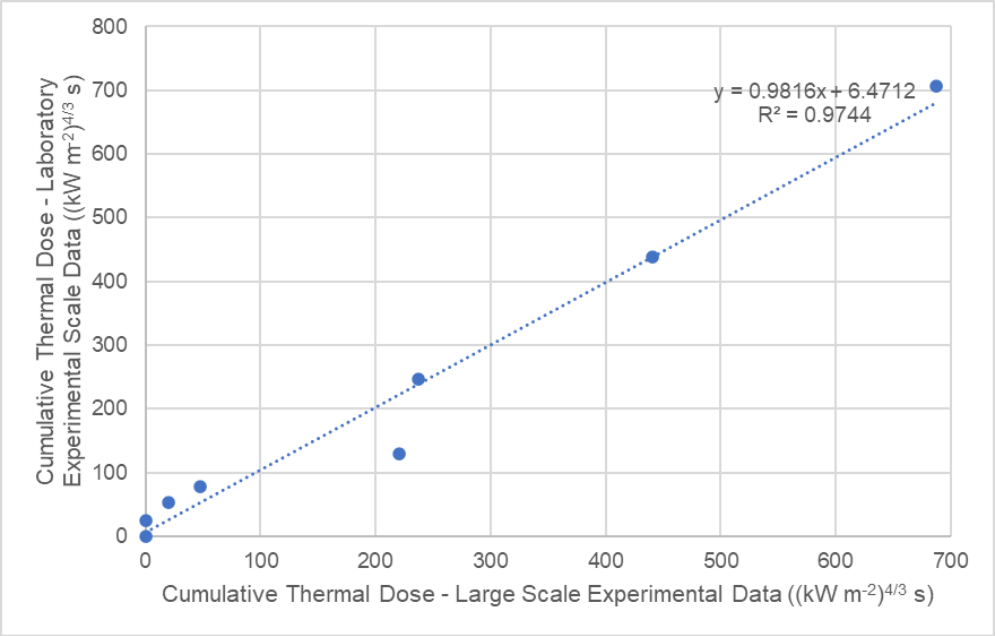

Figure 3-30 Cumulative thermal dose – Laboratory (930°C) vs large scale (RAD03) thermal dose data over a time period of 6 seconds

3.2.4. Materials Tested

The materials tested using the laboratory scale equipment generally focused on thermally thin items. Primarily the mass loss rate and evidence of the damage sustained (including ignition) was recorded for all tests. Materials which underwent transient tests included paper, cardboard, polyethylene sheets (0.2 mm, 0.5 mm and 1 mm thick), plastic drainpipe (black), Perspex, foam, grass, cotton, painted plywood (grey and yellow) and polystyrene.

To compare transient thermal doses with the laboratory scale setup, steady-state tests were conducted using 1 mm, 0.5 mm, and 0.2 mm polyethylene sheets, along with cardboard and paper.

3.2.5. Mass Measurements

Samples were weighed before and after tests. For the laboratory scale tests, a set of Criacr Digital Pocket Scales were used. The scales were capable of measuring up to 500 grams, had a precision of 0.01 grams and were calibrated using known masses

between 2 and 200 grams. The formula used to determine the reading from the scales is given in Figure 3-31.

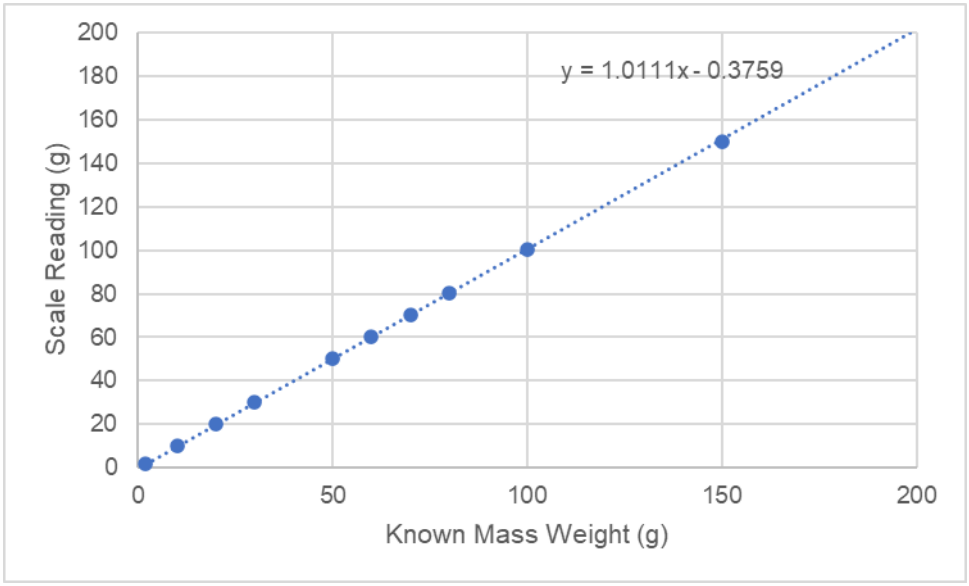

Figure 3-31 Calibrated Scale Equation

3.2.6. Thickness Measurements

Thickness of samples was measured using a set of callipers. For the laboratory scale tests, a set of digital Vernier callipers. The callipers were capable of measuring distance up to 150 mm, had a precision of 0.01 mm and were calibrated following purchase (see Figure 3-32). The formula used to determine the reading from the callipers is given in Figure 3-33.

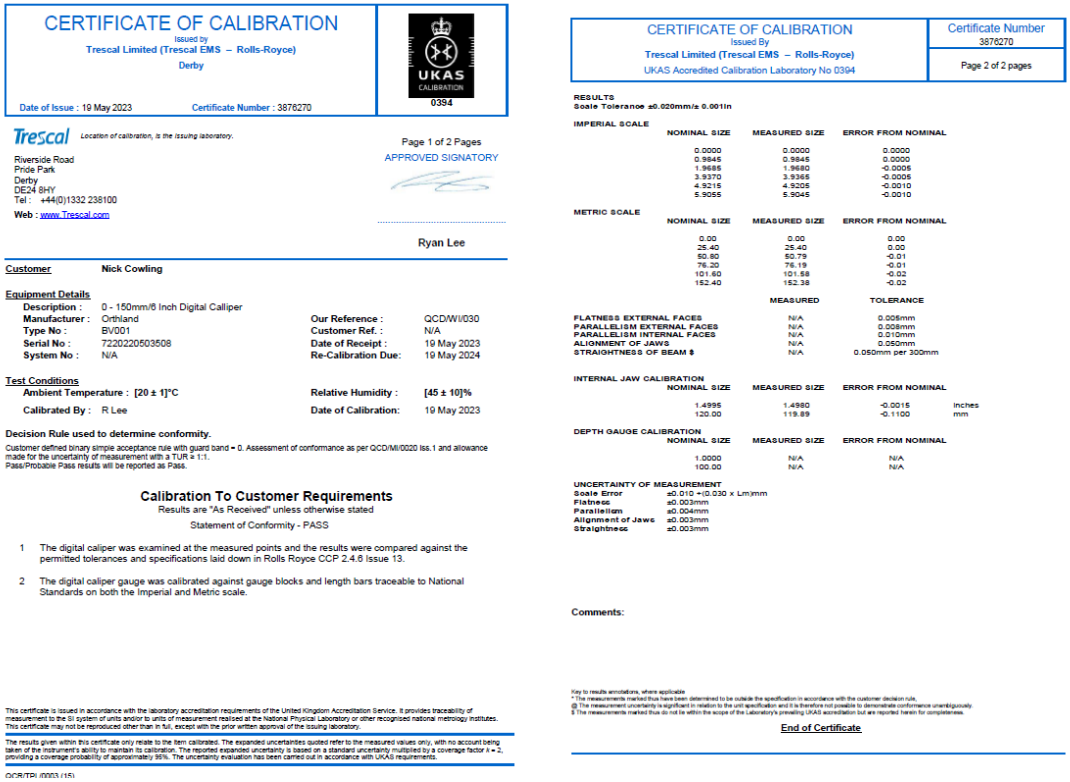

CERTIFICATE OF CALIBRATION
Issued by
Trescal Limited (Trescal EMS – Rolls-Royce)
Derby

UKAS CALIBRATION 0394

Date of Issue : 19 May 2023 Certificate Number : 3876270

Trescal Location of calibration, is the issuing laboratory.

Riverside Road
Pride Park
Derby
DE24 8HY
Tel : +44(0)1332 238100
Web : www.Trescal.com

Page 1 of 2 Pages
APPROVED SIGNATORY

Ryan Lee

Customer Nick Cowling

Equipment Details

Description :	0 - 150mm/6 Inch Digital Calliper		
Manufacturer :	Orthland	Our Reference :	QCD/WI/030
Type No :	BV001	Customer Ref. :	N/A
Serial No :	7220220503508	Date of Receipt :	19 May 2023
System No :	N/A	Re-Calibration Due:	19 May 2024

Test Conditions

Ambient Temperature :	[20 ± 1]°C	Relative Humidity :	[45 ± 10]%
Calibrated By :	R Lee	Date of Calibration:	19 May 2023

Decision Rule used to determine conformity.

Customer defined binary simple acceptance rule with guard band = 0. Assessment of conformance as per QCD/MI/0020 Iss.1 and allowance made for the uncertainty of measurement with a TUR ≥ 1:1.
Pass/Probable Pass results will be reported as Pass.

Calibration To Customer Requirements
Results are "As Received" unless otherwise stated
Statement of Conformity - PASS

1 The digital caliper was examined at the measured points and the results were compared against the permitted tolerances and specifications laid down in Rolls Royce CCP 2.4.6 Issue 13.

2 The digital caliper gauge was calibrated against gauge blocks and length bars traceable to National Standards on both the Imperial and Metric scale.

This certificate is issued in accordance with the laboratory accreditation requirements of the United Kingdom Accreditation Service. It provides traceability of measurement to the SI system of units and/or to units of measurement realised at the National Physical Laboratory or other recognised national metrology institutes. This certificate may not be reproduced other than in full, except with the prior written approval of the issuing laboratory.

The results given within this certificate only relate to the item calibrated. The expanded uncertainties quoted refer to the measured values only, with no account being taken of the instrument's ability to maintain its calibration. The reported expanded uncertainty is based on a standard uncertainty multiplied by a coverage factor k = 2, providing a coverage probability of approximately 95%. The uncertainty evaluation has been carried out in accordance with UKAS requirements.

QCR/TPL/0003 (15)

CERTIFICATE OF CALIBRATION
Issued By
Trescal Limited (Trescal EMS – Rolls-Royce)
UKAS Accredited Calibration Laboratory No 0394

Certificate Number 3876270
Page 2 of 2 pages

RESULTS
Scale Tolerance ±0.020mm/± 0.001in

IMPERIAL SCALE

NOMINAL SIZE	MEASURED SIZE	ERROR FROM NOMINAL
0.0000	0.0000	0.0000
0.9845	0.9845	0.0000
1.9685	1.9680	-0.0005
3.9370	3.9365	-0.0005
4.9215	4.9205	-0.0010
5.9055	5.9045	-0.0010

METRIC SCALE

NOMINAL SIZE	MEASURED SIZE	ERROR FROM NOMINAL
0.00	0.00	0.00
25.40	25.40	0.00
50.80	50.79	-0.01
76.20	76.19	-0.01
101.60	101.58	-0.02
152.40	152.38	-0.02

	MEASURED	TOLERANCE
FLATNESS EXTERNAL FACES	N/A	0.005mm
PARALLELISM EXTERNAL FACES	N/A	0.005mm
PARALLELISM INTERNAL FACES	N/A	0.010mm
ALIGNMENT OF JAWS	N/A	0.050mm
STRAIGHTNESS OF BEAM $	N/A	0.050mm per 300mm

INTERNAL JAW CALIBRATION

NOMINAL SIZE	MEASURED SIZE	ERROR FROM NOMINAL	
1.4995	1.4980	-0.0015	Inches
120.00	119.89	-0.1100	mm

DEPTH GAUGE CALIBRATION

NOMINAL SIZE	MEASURED SIZE	ERROR FROM NOMINAL
1.0000	N/A	N/A
100.00	N/A	N/A

UNCERTAINTY OF MEASUREMENT

Scale Error	±0.010 +(0.030 x Lm)mm
Flatness	±0.003mm
Parallelism	±0.004mm
Alignment of Jaws	±0.003mm
Straightness	±0.003mm

Comments:

Key to results annotations, where applicable
* The measurements marked thus have been determined to be outside the specification in accordance with the customer decision rule.
@ The measurement uncertainty is significant in relation to the unit specification and it is therefore not possible to demonstrate conformance unambiguously.
$ The measurements marked thus do not lie within the scope of the Laboratory's prevailing UKAS accreditation but are reported herein for completeness.

End of Certificate

Figure 3-32 Calliper Calibration Certificate

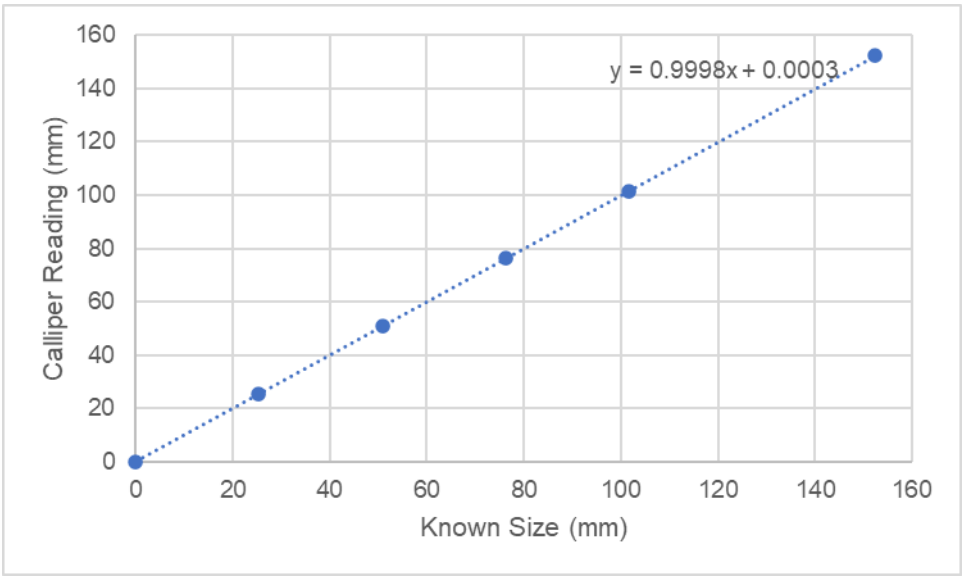

Figure 3-33 Calibrated Scale Equation

3.2.7. Density Measurements

The density of the samples was calculated from measurements of the weight and size of the samples. The density used in the analysis is based on the average density of all samples for each material. Importantly for cardboard, measurements were taken of the top layer after separation from the corrugated element (see Figure 3-34).

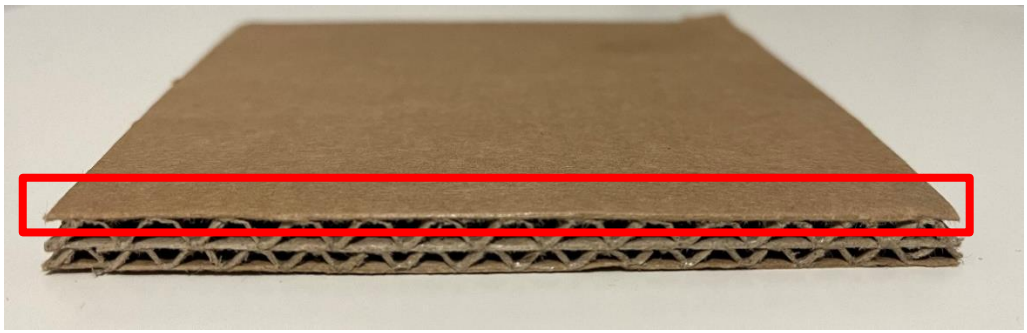

(a)

(b)

Figure 3-34 Separation of card to undertake measurements to calculate density (a) prior to separation and (b) after separation

3.2.8. Video Records

All tests were recorded with a Canon Power shot SX610 HS, high definition, camera which also served as a time stamp. The camera was positioned on a tripod for the tests.

3.2.9. Temperature Measurements

Some tests were recorded with a Testo 883 thermal imaging camera. The thermal imaging measures infrared radiation using a thermal sensor and converts data received into a digital signal. The camara is calibrated against national standard at different temperatures.

3.2.10. Repeatability of the Laboratory Scale Setup Tests

Samples of paper were used with adjustments made to the experimental setup to investigate the sensitivity of changes to the cone calorimeter temperature setting, opening/closing the hood and having the pump on or off.

The results show that the hood had limited effect on the experiments and the fan reduced the likelihood of ignition, see Table 3-3.

Table 3-3 Repeatibility of Tests

Temperature Setting	Hood Open/Closed	Fan On/Off	Ignition (Yes/No)
700	Open	Off	No x 3
750	Open	Off	Yes after 7.3, 7.1 and 6.9 seconds.
750	Closed	Off	Yes after 7.5, 7.2 and 7.0 seconds.
750	Closed	On	No x 3
750	Open	On	No x 3
760	Closed	On	No x 3
760	Open	On	No x 3
770	Closed	On	No x 3
770	Open	On	No x 3
800	Closed	On	No x 3
800	Open	On	No x 3

3.2.11. Experimental Error

The accuracy of measurements in the laboratory scale tests is as follows:

- The cone colorimeter is capable of thermal radiation reading to 0.1 kW m^{-2} and whilst readings fluctuate at higher thermal radiation is estimated to be ±5%.
- Scales were found to have an error of ±1%.
- Video records were used to determine the accuracy of observations and were made with to ±0.01 seconds.
- Thermal imaging camera measurements were recorded to a quoted accuracy of ±2% (mv), ±2°C.

Ultimately, despite a delay between placing the sample holder and activating the lift, when the lift reached its lowest position with the highest temperature setting, the thermal radiation did not exceed 10 kW m^{-2}, remaining below a critical value for ignition based on the Lawson and Simms (94) experiments.

CHAPTER 4

LARGE SCALE TEST RESULTS

Two large scale short duration rupture tests were carried out in 2015 at DNV's Spadeadam test site. During the second test there was a failure of a network switch in the East forward recording suite which led to the failure of the SPARTAN logger. Therefore only data from the west recording suite was recovered in the second test.

4.1. Depressurisation

The depressurisation of the pipeline following initiation of the fracture is illustrated in Figure 4-1. The results have been compared with a calculation of the gas outflow using the method given in the TNO Yellow Book (see Equation (2-7) in Section 2.2.3). The delay between the east and west profiles is likely due to the material differences of test sections used during the test.

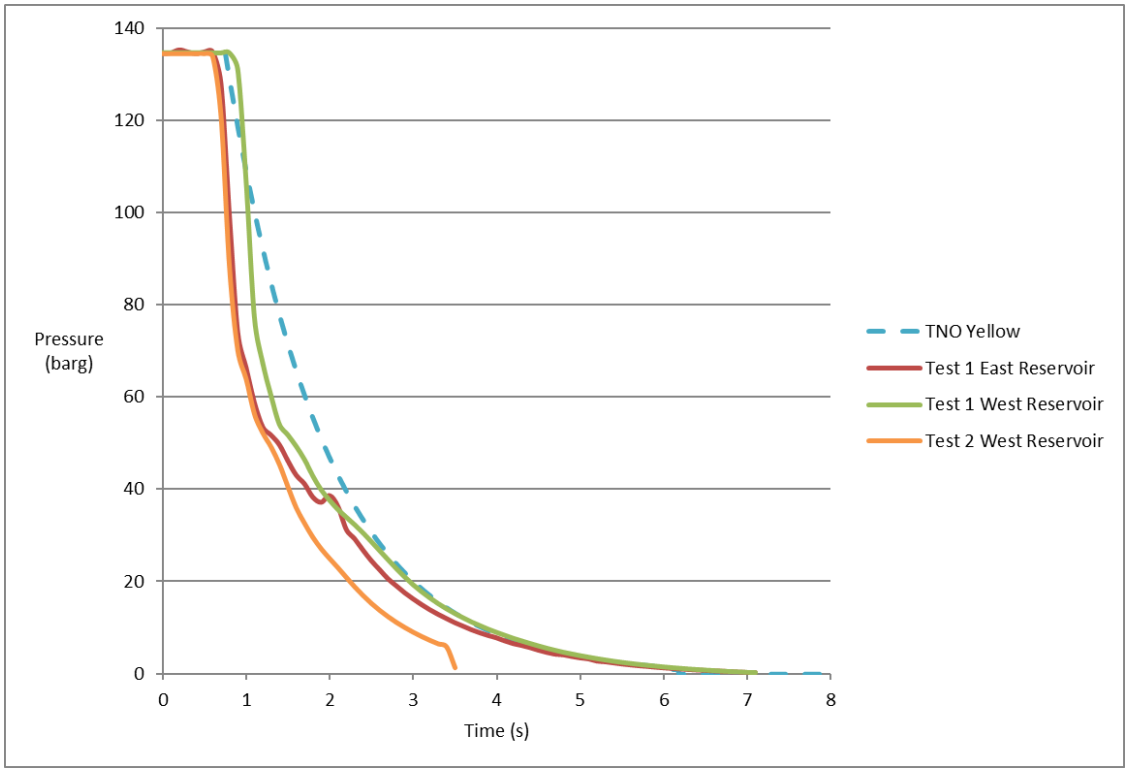

Figure 4-1 Comparison of test decompression data against TNO Yellow Book (46) prediction

In order to calculate the outflow rate and generate the blue curve in Figure 4-1, using the TNO Yellow Book, it was assumed that a portion of the material was instantly released from the ruptured section and that there was flow from both ends of the

pipeline (see Figure 2-9). Even with the changes, the TNO Yellow Book unpredicts the outflow rate for the full bore rupture event. This underprediction is greater for test 2 whereby the ruptured section was longer. Three seconds after the start of the outflow, the TNO Yellow Book prediction more closely matches the observed results. This is postulated to be the point at which outflow more closely matches outflow from two ends of a pipeline.

It was assumed that gas was instantaneously released prior to ignition in the calculation due to the speed at which the fracture propagates along the length of the pipeline. Propagating fractures initially run along the top of the pipeline due to the contained energy of the pressurised gases (see Figure 4-2). When the material of the pipeline has sufficient strength to prevent the fracture from propagating, the fracture runs down the side of the pipeline and 'arrests' i.e. stops (see Figure 4-3). In the first test the fracture took ~0.1 ms to arrest and 0.3 ms to arrest in the second test. As the fracture speed would be the same, this supports that the fracture length on test 2 was longer.

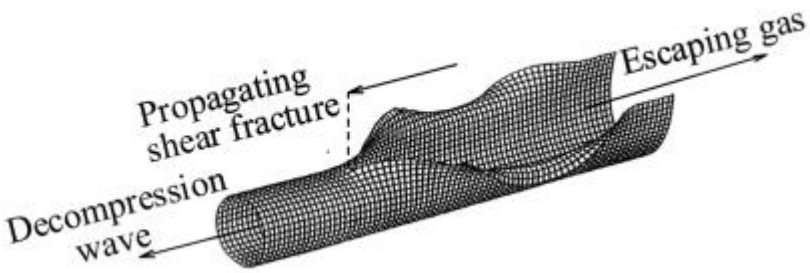

Figure 4-2 Illustration of fracture propagating along pipeline (112)

Figure 4-3 Illustration of arrested fracture, with red circle showing point of arrest (113)

One key difference between the 2 tests is that crater length in test 2 was larger than test 1 i.e. the fracture length was larger and hence the underprediction was greater in test 2. This occurred due material properties of the pipeline selected for the tests which were also being investigated but are outside the scope of this research. Whilst this may be an area for future study, as indicated in Section 2.3, pipeline operators design pipelines such that a fracture is arrested within acceptable lengths (3).

With respect to the TNO Yellow Book formula for gas outflow, overall, at initial (high) pressure there is general scattering of the data, before a phase of underprediction, until 40 bar, when there is agreement within 10% of values (see Figure 4-4) for test 1. So generally the TNO Yellow book is useful in providing an estimate of the gas outflow. To conduct a more comprehensive analysis, additional tests, which can be expensive, would be necessary.

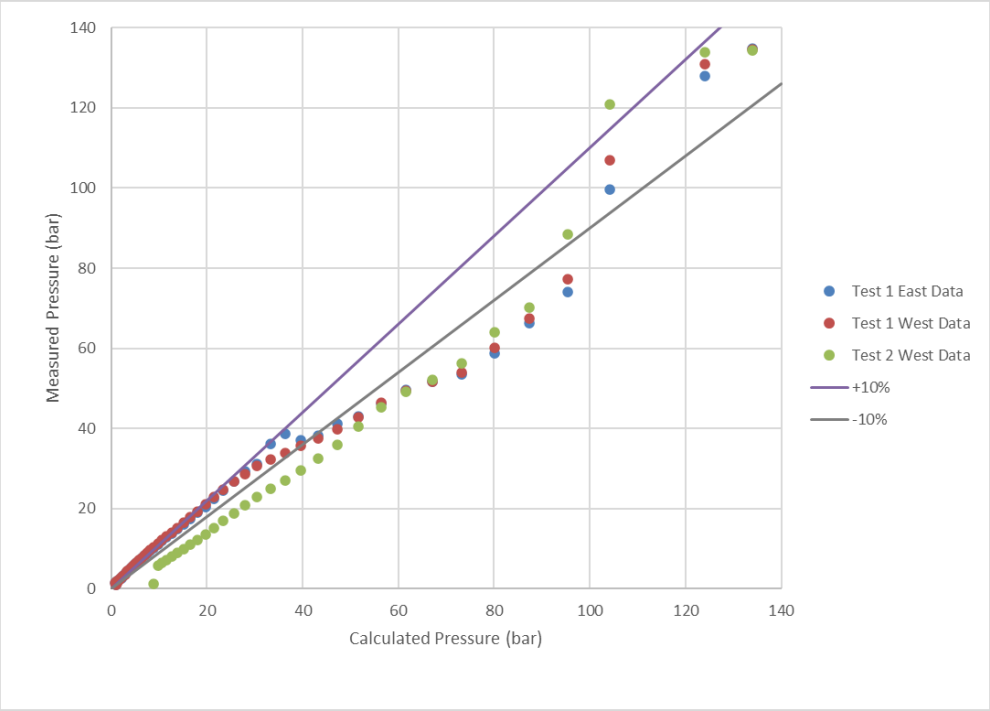

Figure 4-4 Comparison of test decompression data against TNO yellow book prediction

4.2. Thermal Radiation Flux

Thermal radiation readings from test 1 are shown in Figure 4-5 and readings from test 2 are shown in Figure 4-6. In the first test, data was recorded from all locations where radiometers were located. However, the signal from the radiometer located 200 metres to the north was lost before the peak signal was reached. Photographs of the fireball from test 1 and test 2 is shown in Figure 4-7 and Figure 4-8 respectively. The wind conditions for each test are shown in Figure 4-9.

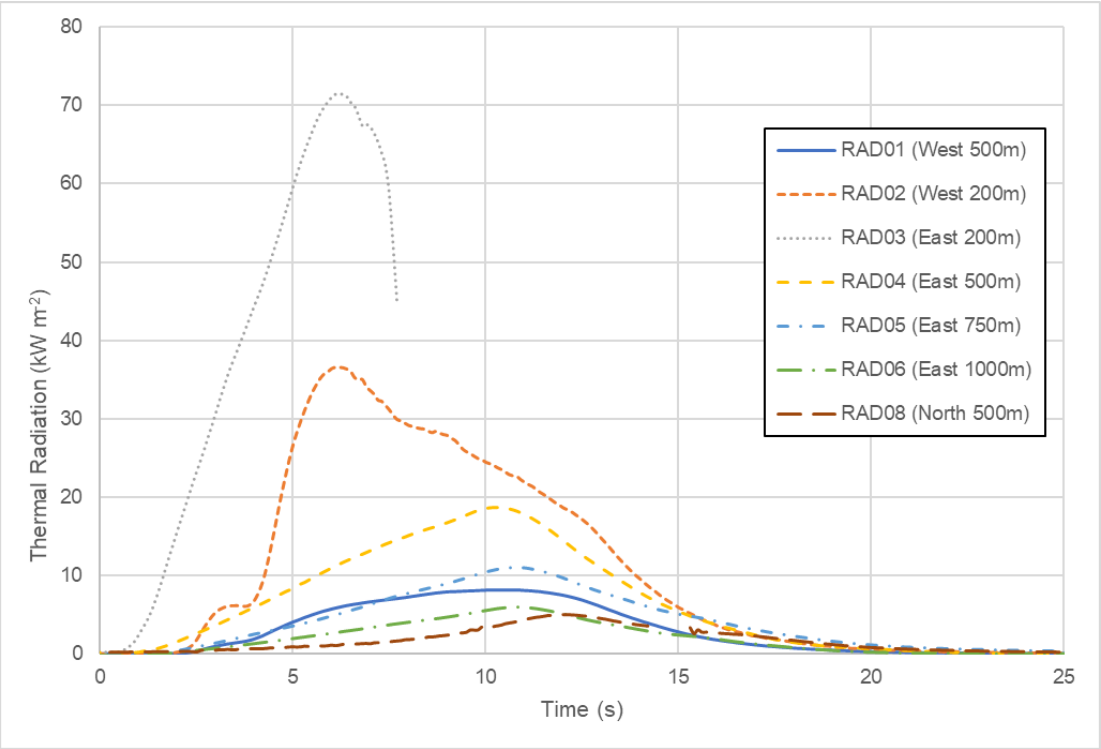

Figure 4-5 Thermal radiation – Test 1

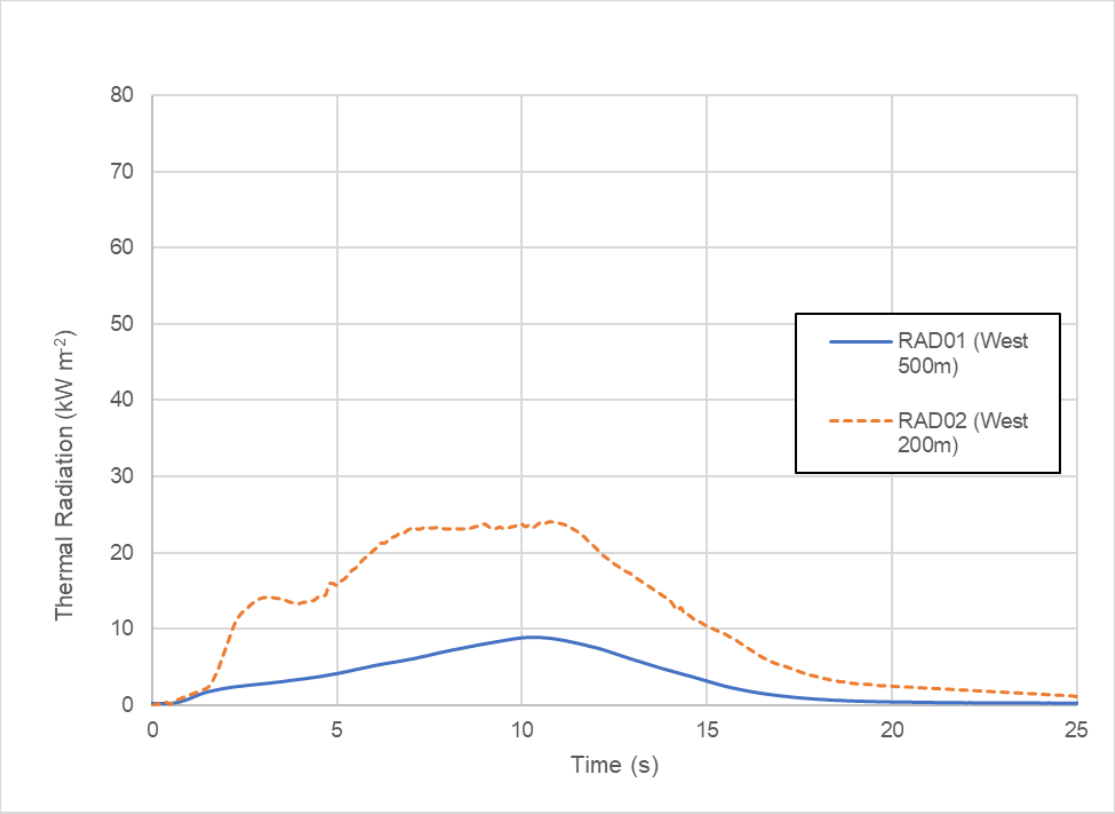

Figure 4-6 Thermal radiation – Test 2

Figure 4-7 Fireball from Test 1

Figure 4-8 Fireball from Test 2

Figure 4-9 Wind speeds during pipeline rupture tests

In the first test a peak thermal radiation flux of over 70 kW m^{-2} at 200 m was observed (see Figure 4-5). It took 6 seconds to reach this thermal radiation level. At 750 m it took over 20 seconds for the thermal radiation level to fall below 1 kW m^{-2}. The fireball mushroomed from the release point and was observed to be tilted by the prevailing wind direction (295°, 7.6 m/s). Thus the peak thermal radiation level was observed on the eastern radiometer. As a peak of 35 kW m^{-2} was observed on the western radiometer located 200 m form the release point, the thermal radiation field was found to be asymmetrical. It is further noted that RAD02 in the second test received a lower peak thermal radiation level compared to the first test. The thermal radiation readings to the east are likely to have been affected by the longer fracture length already discussed and the prevailing wind conditions, which were lower in the second test or the fracture of the pipeline. These would be areas worthwhile for further research.

Using the same method as Wang (68) (see equations (2-23) to (2-31) in section 2.6.3), the thermal radiation flux was calculated as shown in Figure 4-10. As the rational for the relationship of the fraction of heat radiated was unclear the calculated value of 0.61 was calculated using the Wang equation (test pressure of 134 bar (13.4 MPa)) and compared with a value of 0.3.

Comparison of the predicted thermal radiation levels against the test data are shown in Figure 4-10 and shows good agreement in the far field. In the near field the theoretical calculation overpredicts by 60%, with better agreement with a F_r value of 0.3. This is consistent with upper limit (0.14 to 0.35) of reported fraction of heat radiated data for other sources (75).

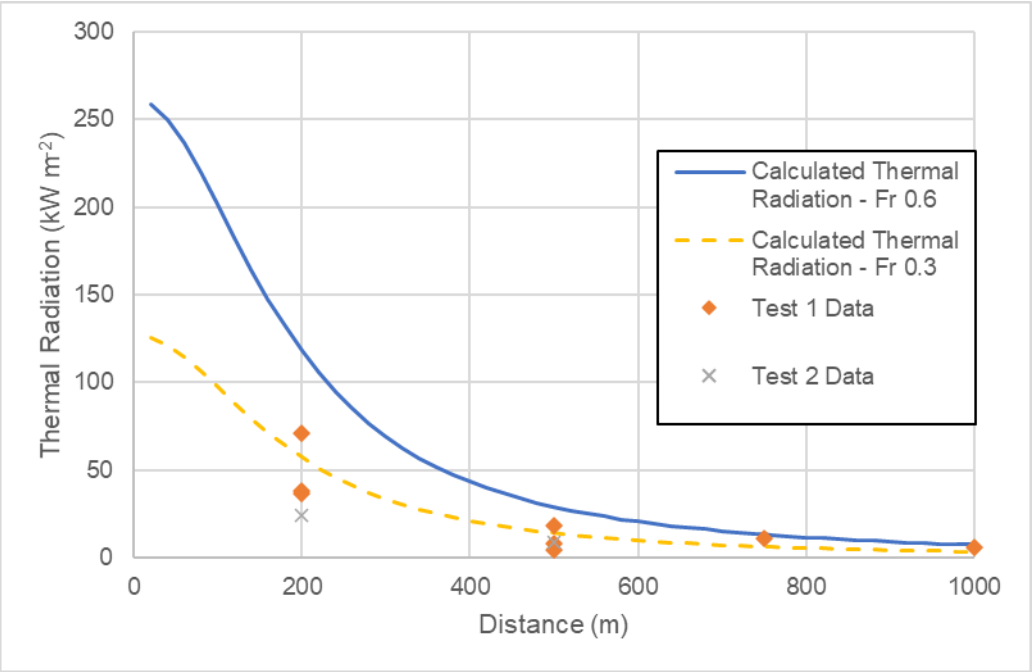

Figure 4-10 Thermal radiation and observed values from tests

4.3. Damage to Plants and Vegetation

In addition to radiometers, plants were also installed at radiometer locations for the second test (see Figure 4-11, Figure 4-12 and Figure 4-13).

After the second test, grass fires were additionally observed to the northeast of the rupture point (see Figure 4-14).

Figure 4-11 Plants located at RAD 02 for Test 2 before (left) and after (right)

Figure 4-12 Plants located at RAD 02 for Test 2 before (left) and after (right)

Figure 4-13 Plants located at RAD 03 for Test 2 before (left) and after (right)

(a)

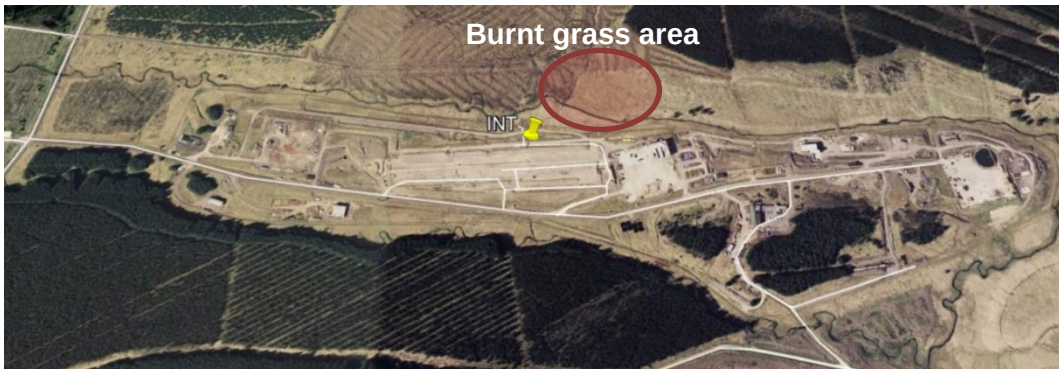

(b)

Figure 4-14 Burnt grass area following second test shown in (a) and relative location shown in (b) (centre located 150 m from INT)

In the second test, plants at locations RAD02 and RAD01 were exposed to a thermal radiation flux just over 20 and 10 kW m^{-2} respectively. Plants located at RAD03 would have been exposed to a thermal radiation flux of just over 70 kW m^{-2} based on the readings from the first tests. While there was no ignition, evidence of scorching was observed near the top of plants at locations RAD02 and RAD03. However, there also appeared to be shielding by the top layers of leaves. The plants at these locations would have been exposed to a thermal dose in the range 765 to 1215 $(kW\ m^{-2})^{4/3}\ s^{-1}$.

The burnt grass was located closer to the rupture location (150 m away) than the plants and did ignite. Although a radiometer was not located in this area to confirm the thermal radiation received, from Figure 4-10, the peak would be in range of 60-90 kW m^{-2}. The grass would have been exposed to a thermal dose in the range 1160 to 1980 $(kW\ m^{-2})^{4/3}\ s^{-1}$.

4.4. Fireball Diameter

The fireball diameter was analysed using the photographic records and the equations referred to in Section 3.1.2.14. Equation (2-20) was used to predict predicted fireball diameter. To use Equation (2-20), knowledge of the mass released is required. The mass released was calculated using the TNO Yellow Book correlation noting that this underpredicted the gas release rate described in Section 4.1.

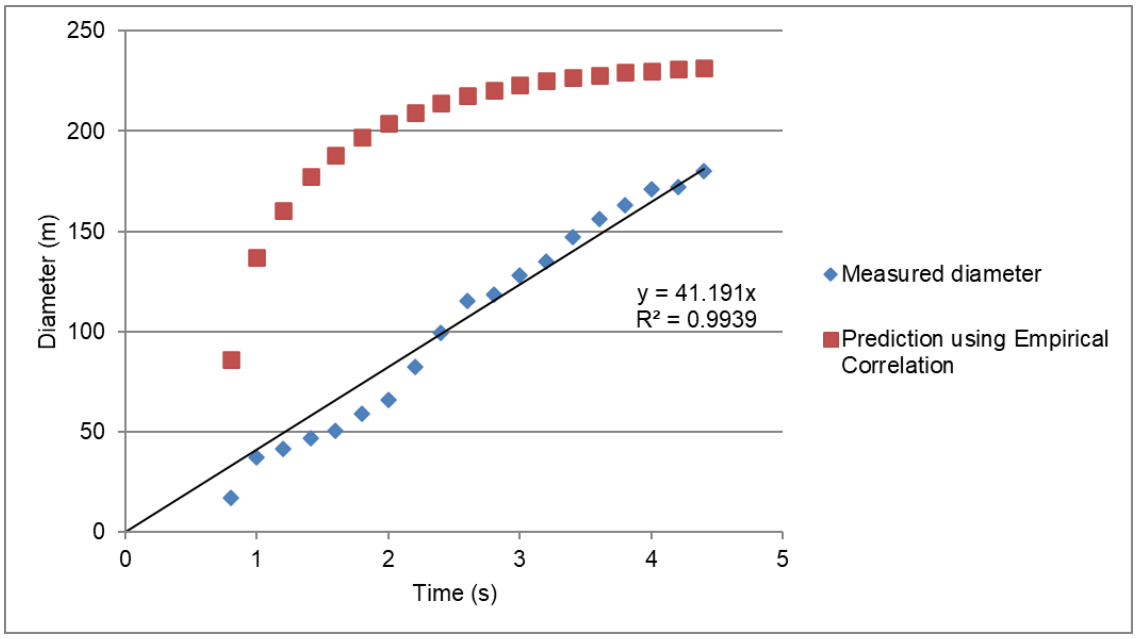

Figure 4-15 Comparison of measured fireball diameter with empirical predictions

Figure 4-15 shows that the empirical correlation overpredicts the diameter. The difference in the calculated and observed diameter values follow the same pattern for the prediction of the gas release rate (0-1s variable, 1-3s – large overprediction, 3-5s values converge), with the difference for fireball diameter larger. This result is not unexpected as HSE's model, which uses the empirical correlations, consistently overestimated the observed fireball consequences when compared with burn areas observed from incidents (114). A complex model for predicting the size of the initial fireball has been developed by Cleaver (36). However, there remains a demand for more simpler models. This data suggests that the simple models are cautious and would warrant improvement. To undertake this development additional publicly accessible data would be necessary.

The photographic records show the formation of two separate balls, possibly due to the staggered release of the material, however the overall shape is consistent with the mushroom caps referred to by Cleaver (36). It is important to note, however, that this shape deviates from the photographic records of LNG tests conducted by Wang (68), as illustrated in Figure 2-17, where a single sphere is depicted atop a stalk.

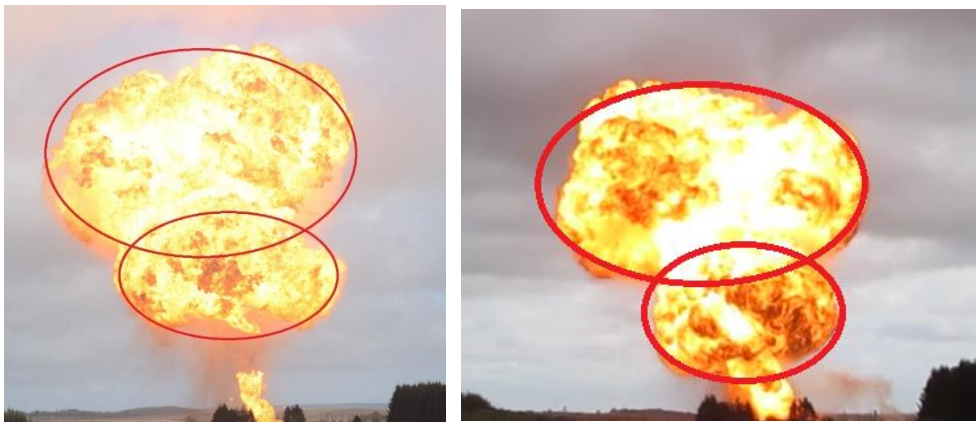

Figure 4-16 Analysis of photographic records

Evidence of the gas released (with ejected soil) prior to ignition is shown Figure 4-17. Figure 4-18 shows that the gas was ignited between 1 and 2 seconds after initiation of the test and Figure 4-19 shows that after 4 seconds the cloud had fully ignited at ground level. At this point there would have been limited gas left in the pipeline as shown in Figure 4-1, where between 4 and 6 seconds, the pressure decay to zero. The presence of the first ball is predicted to be due to the gas released from the ruptured section of the pipeline, with the second ball due to the gas released from the pipeline, with the stalk formed from the decaying gas release.

(a) 0 ms (b) 100 ms (c) 200 ms

Figure 4-17 Video footage shortly after the start of the test, with no ignition

(a) 1 s (b) 2 s (c) 3s

Figure 4-18 Video footage showing partial ignition of the cloud

Figure 4-19 Video footage showing full ignition of the cloud after 4 seconds

4.5. Free Field Overpressure

The overpressure measured in test 1 is shown in Figure 4-20. Overpressure that can cause injuries and or structural damage to buildings are those in excess of 30 mbar (0.44 psi) (57). Based on the readings taken from the 1st test, hazard distances from overpressures are smaller than the thermal radiation hazard distances. Based on this information, overpressure readings from the second test were not recorded.

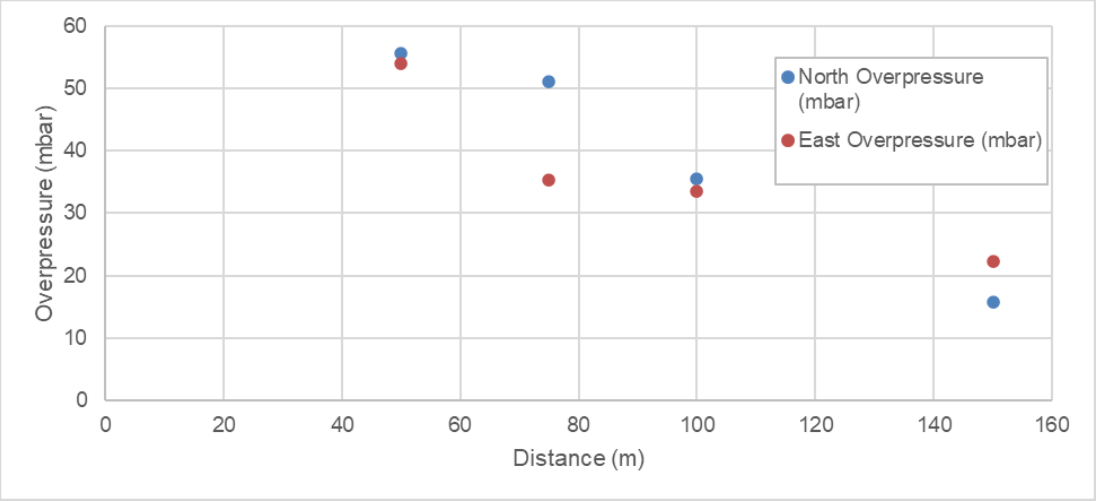

Figure 4-20 Free Field Overpressure

The overpressure values recorded in these tests are larger than those shown in Figure 2-14. This is expected as expected the current dataset is based on a release for a

1.2 m diameter pipeline whereas Figure 2-14 is based on a release from 150 mm diameter pipeline. In summary, the findings of this research support that the thermal radiation hazard poses a greater risk when evaluating overpressure readings at equivalent distances.

4.6. Crater Size

Measurements of the crater from both tests was undertaken by DNV's experienced Spadeadam site team referred to in Section 3.1. However due to the purpose of the tests whereby more than one pipeline length was deliberately fractured, the results are not considered to be representative of how pipelines are installed/fractured. This illustrated by the laser scan carried out following one of the tests (see Figure 4-21), which indicates the explosive charge could have caused the central crater, with outflow from either end of the test sections causing crater either side of this.

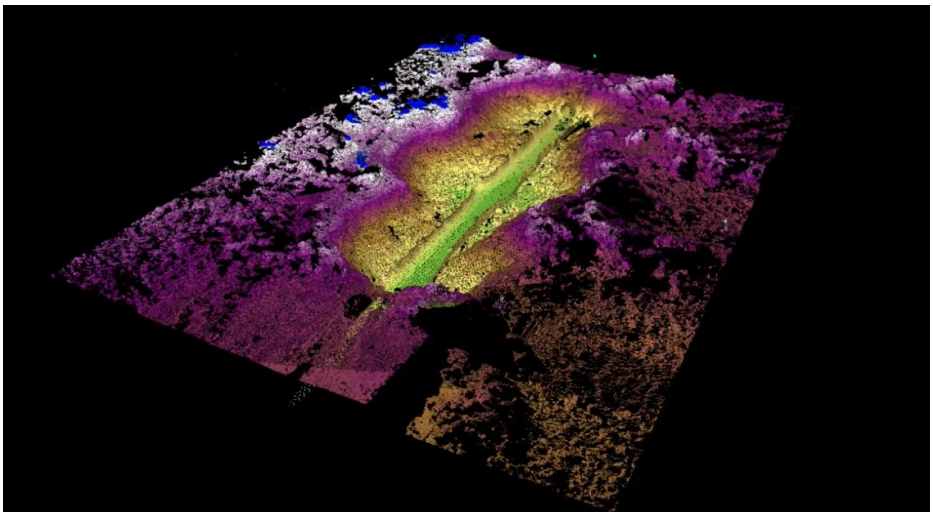

Figure 4-21: Laser scan of crater following 2nd test taken by DNV'sSpadeadam site team

Measured crater depths and widths recorded in the tests were compared with calculations using equations (2-8) to (2-12) assuming a 'w' value of 2.7 are shown in Table 4-1. The estimated crater depth falls in between the observed depths from both experiments. However, regarding the crater's width, the first test closely matches the predicted value, likely because of its shorter fracture length, which is consistent with the assumptions underlying the predictive equations (see Section 2.3).

Table 4-1 Predicted crater dimensions compared with test values

	Predicted (m)	Test 1 (m)	Test 2 (m)
D_{cra} (Equation (2-10))	3.58	2.9	4.5
Width (Equation (2-12))	13.3	15.5	21.0

4.7. Summary

The large scale tests indicate that the empirical correlations, derived from BLEVE experiments, which are utilised to predict fireball diameter, tend to overestimate the diameter when applied to an ignited release from a pipeline. The HSE have previously noted this conservatism with the use of empirical correlations for fireball releases (18), (114). This conservatism was supported by these tests, whereby measured thermal radiation was up to 70 kW m^{-2} within 200 m and there were many materials in the vicinity that did not ignite. This includes plants put out for the second test. While grass was ignited in the second test, it is possible that hot embers and debris could have fallen onto the grass to cause piloted ignition in patches as shown in the debris field shown in Figure 4-22. This highlights the need to understand the likelihood of ignition under variable heat fluxes.

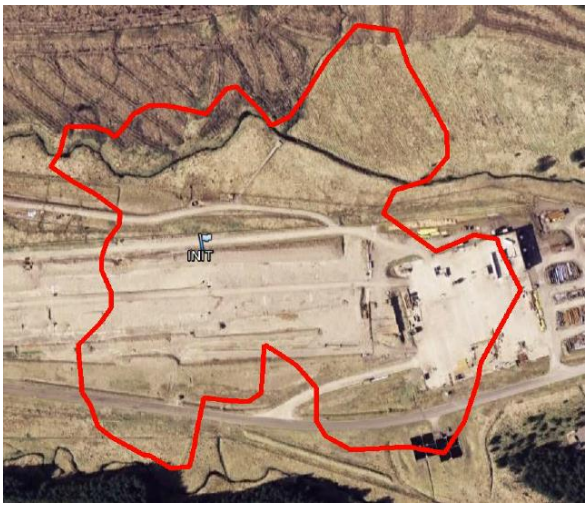

Figure 4-22 Debris field

CHAPTER 5

LABORATORY SCALE TEST RESULTS

5.1. Transient Tests

5.1.1. Introduction

Different material samples were exposed to variable thermal radiation flux. The measured mass loss was compared with Biot number for the material and the cumulative thermal dose (based on a 4/3 exponent), calculated as described in Section 3.2.3. The Biot number has been calculated for different materials using Equation (2-33), with a value for the convective heat transfer coefficient (h) for the cone calorimeter taken to be 14.3 – 25.2 kW $m^{-2} K^{-1}$ for the temperature range 410 – 930K (115). Values of 14.3 and 25.2 kW $m^{-2} K^{-1}$ was used to calculate the Biot number for the material samples tested as shown in Table 5-1. As outlined in Section 2, Biot numbers below 0.1 are thermally thin, implying uniform temperature across the material.

Table 5-1 Biot numbers calculated for the materials tested

Material	Thermal Conductivity ($W\ m^{-1}\ K^{-1}$)	Thickness (mm)	Calculated Biot Number (Dimensionless)	
			14.3	**25.2**
Perspex (Polymethylmethacrylate)	0.19 (88) – 0.27 (89)	2.00	0.11 - 0.15	0.19 – 0.27
Paper (Cellulose)	0.039 (116)	0.19	0.07	0.12
Paper card (Cellulose)	0.039 (116)	0.29	0.11	0.19
Polyethylene	0.35 -0.44 (88)	0.20	0.01	0.01
Polyethylene	0.35 -0.44 (88)	0.50	0.02	0.03
Polyethylene	0.35 -0.44 (88)	1.00	0.03	0.06
Cardboard	0.039 (116)	0.29	0.11	0.19
Laminated Cardboard	0.01[1]	0.52	0.74	1.31
Cotton	0.026-0.065 (117)	1.27	0.28 - 0.70	0.5 - 1.23
Cotton	0.026-0.065 (117)	0.20	0.04 - 0.11	0.08 – 0.19
Drain pipe (Poly vinyl chloride)	0.16 (88)	2.00	0.18	0.32
Foam (Polyurethane)	0.177 (118)	0.01	0.001	0.001
Grass (Wet)	0.44 – 0.59	0.2	0.007	0.01
Polyester clothing	0.38 (119)	1.2	0.05	0.08
[1] Assumed combination of polyethylene and cardboard, so increased value.				

5.1.2. No Ignition/Flaming Combustion

The majority of samples did not ignite (spontaneously) when subjected to transient thermal radiation fluxes that peaked at 70 kW m^{-2}, despite the thermal radiation flux being significantly in excess of the upper limit (40 kW m^{-2}) referred to by the HSE. However, there was visible evidence of smoke. The average mass loss rate has been plotted against Biot number and cumulative thermal dose for different materials in Figure 5-1 to Figure 5-3.

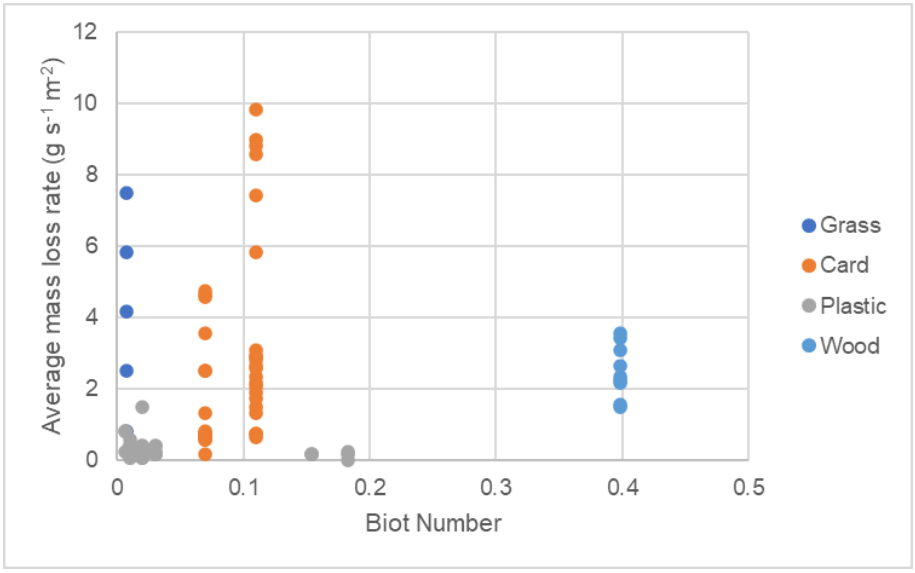

Figure 5-1 Plot of average mass loss rate against Biot number for different materials (No ignition, no pilot)

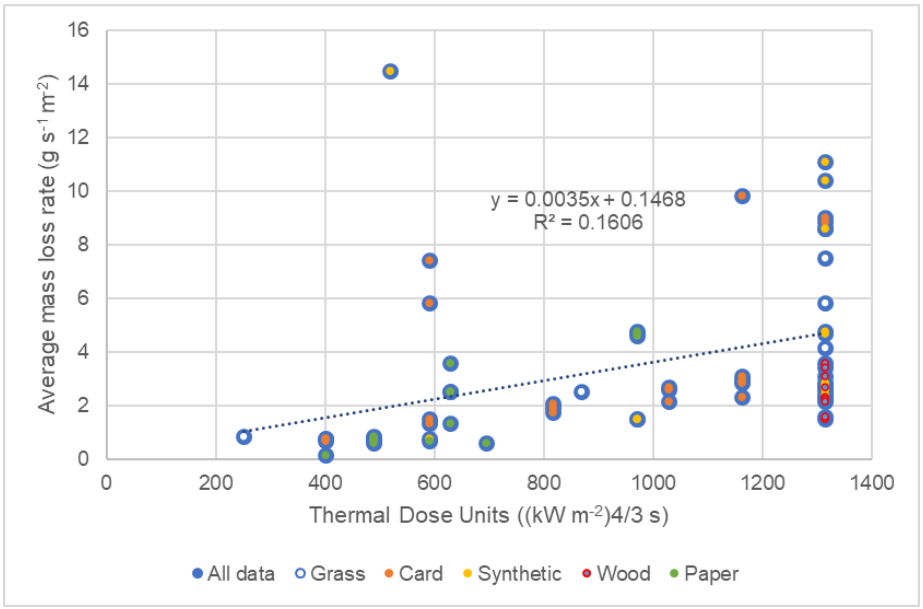

Figure 5-2 Plot of average mass loss rate against thermal dose for grass, card, Synthetics, Wood and Paper (No ignition, no pilot)

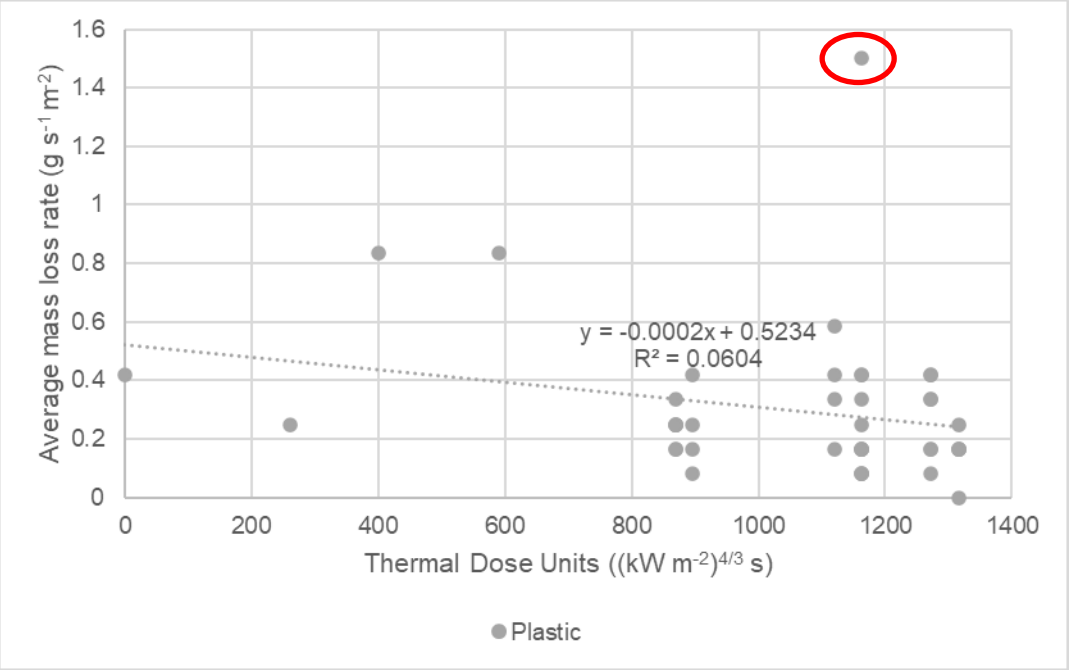

Figure 5-3 Plot of average mass loss rate against thermal dose for plastic (No ignition, no pilot)

Figure 5-2 illustrates that as the thermal dose increases, there is an intuitive increase in the mass loss rate. However, plastics deviate from this trend, with the average mass loss rate remaining below 1 g m^{-2} s^{-2} for the majority of samples tested. McAllister's measurements of critical mass flow rates for combustion (120) fall between 1-2 g m^{-2} s^{-2}. This suggests these materials, despite having a Biot number less than 0.1 so classed as thermally thin, are unlikely to spontaneously ignite during the fireball phase and imply the temperature of the polyethylene samples did not exceed thermal stability values of 406°C (88). Figure 5-1 to Figure 5-3 reveal significant scattering of the data and while scattering of experimental ignition data is common, see Figure 2-31, Figure 2-32 and Figure 2-33. However, the fit of the data (see each coefficient of determination shown in Figure 5-2 and Figure 5-3 and the highlighted result) is not satisfactory suggesting the need for consideration of other parameters more than just the Biot number.

5.1.3. Moisture Content

Experiments were carried out with grass taken from the ground less than 48 hours (wet) and over 3 months (dry) before the laboratory scale tests. The “wet” sample did not spontaneously ignite during the test whereas the “dry” sample did. Attempts were made to quantify the percentage moisture content of the samples with a probe, however only qualitative measurements were able to be obtained, which were not distinguishable from one another (i.e. readings of dry vs dry plus).

Figure 5-4 Wet sample of grass before (left) and after (right) a laboratory scale test – exposed to a thermal radaition dose of (1315 kW m^{-2})$^{4/3}$ s

Figure 5-5 Dry sample of grass before (left) and after (right) a laboratory scale test – exposed to to a thermal radaition dose of (1315 kW m^{-2})$^{4/3}$ s

The wet grass was subjected to a thermal dose of 1315 (kW m^{-2})$^{4/3}$ s (see Figure 5-6). This is likely to have been lower than the thermal dose that grass in the large scale tests is postulated to have been exposed to. The average mass loss rate was of the order 4-7 g m^{-2} s^{-1} which is in excess of the 1-2 g m^{-2} s^{-2} stated by McAllister. Subsequent experiments with dried grass exposed to the same thermal dose (1315 (kW m^{-2})$^{4/3}$ s) did spontaneously ignite. However tests with dried out grass lower thermal doses (250 and 870 (kW m^{-2})$^{4/3}$ s) did not ignite but had mass loss rates of the order 1-3 g m^{-2} s^{-1}.

Figure 5-6 No igntion of grass (No pilot)

Tests were also carried out with wet and dry towels. Initially dry towels (weight 3.7 g) were subjected to a thermal dose of 1315 (kW m^{-2})$^{4/3}$ s which ignited when dry, but

when wetted (total weight 11.3 g, water weight of 7.6 g) did not ignite, yet had an average mass loss rate of 11.1 g m^{-2} s^{-1}.

The experiments involving "wet" grass and towels demonstrate a dependency on moisture content for spontaneous ignition which would be worthwhile of further research. The effect of moisture on wood has been investigated by Lawson (121), which found that moisture increased the thermal conductivity and volumetric specific heat and heat was transferred to the water with evaporation cooling hotter regions.

5.1.4. Wood

There was no ignition during the transient tests with samples of plywood. There was only a slight difference between the before and after photos (see Figure 5-7), however the average mass loss rate ranged between 3 and 3.5 g m^{-2} s^{-1}.

Figure 5-7 Comparison of before and after photos of plywood, with blue arrow indicating where the sample holder has provided shielding

Additional tests were carried with painted samples of plywood which included 2.1 g of paint. There was negligible difference between the before and after photos and no evidence of scorching or blistering. The average mass loss rate ranged between 1.5 and 2.2 g m^{-2} s^{-1}, i.e. the paint provided shielding (see Figure 5-8). It would normally be expected that darker colours would increase the absorbed infrared radiation absorbed compared to the unpainted sample, however, absorption is also dependent upon the thickness of the paint as well as the pigments contained within (122).

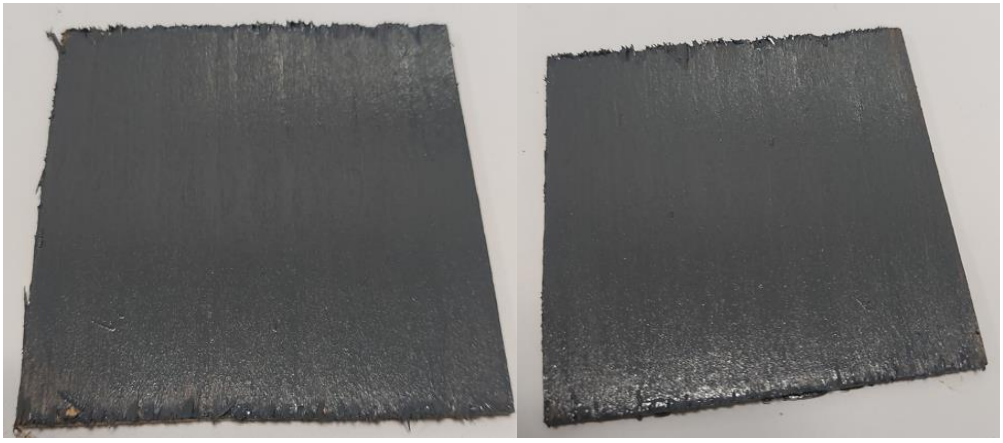

Figure 5-8 Comparison of before and after photos of painted plywood

Other industries do attempt to interpret post incident fire damage (123), (124). Therefore, the observation of no damage to a painted surface is of interest for post incident investigation as it could provide an insight into the sequence of events following ignition. The laboratory technique developed as part of this research could therefore be used to undertake post incident analysis of different materials.

5.1.5. Composite Materials

One test was carried out with a composite material. The composite material tested was a cardboard that had a laminated outer coating. When the cardboard face with the laminated coating was exposed to a thermal radiation of 1300 $(kW\ m^{-2})^{4/3}\ s$, the damage was limited to scorching (see Figure 5-9), whereas the face without the laminated coating spontaneously ignited (see Figure 5-10).

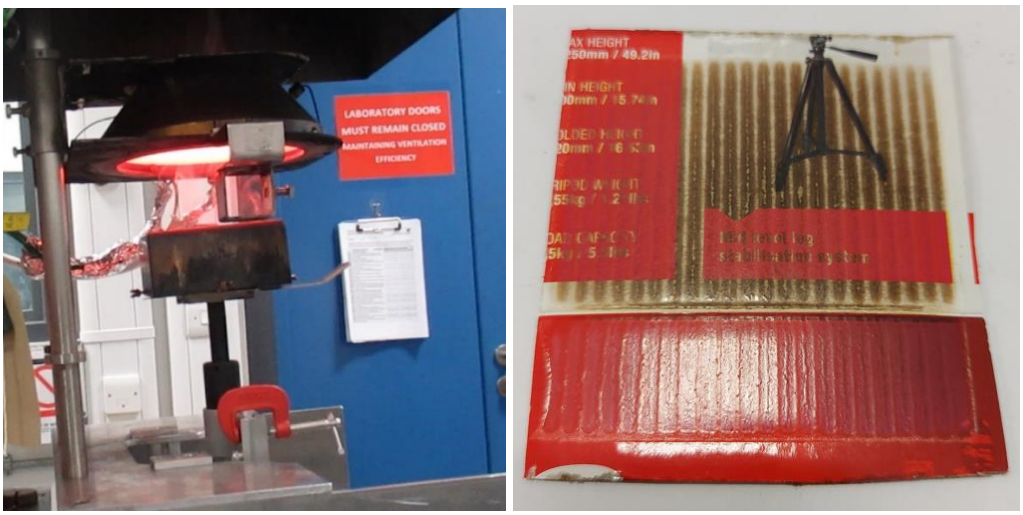

Figure 5-9 Pyrolysis and scorching of cardboard face with laminated coating (No pilot)

Figure 5-10 Spontaneous igntion of cardboard face without laminated coating (No pilot)

5.1.6. Spontaneous Ignition

Paper, cardboard, dried grass and 0.2 mm plastic spontaneously ignited in the short duration transient tests. The thermal dose exposure was calculated as described in Section 3.2.3 and plotted against Biot number as shown in Figure 5-11.

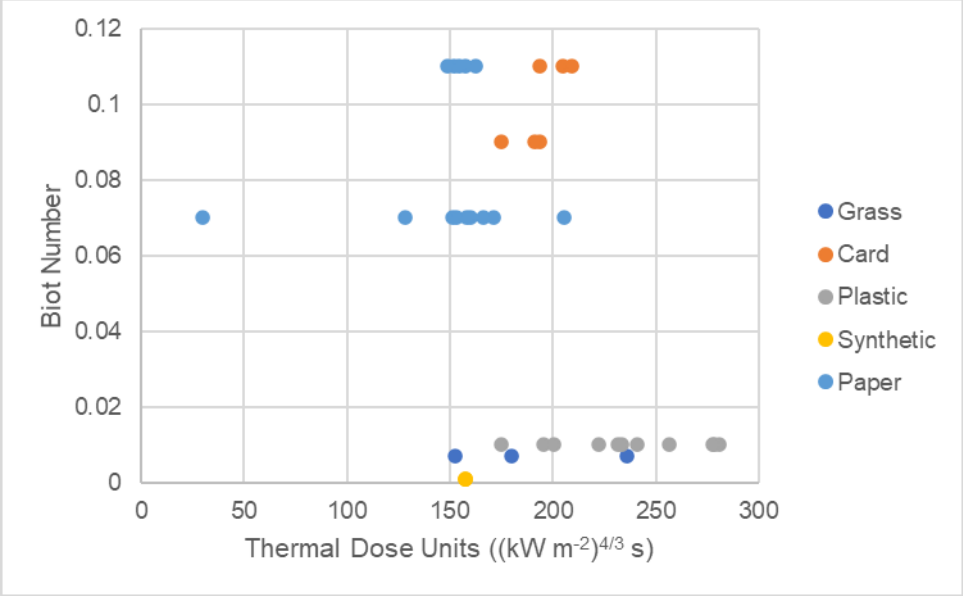

Figure 5-11 Spontaneous igntion of during transient tests (No pilot)

Figure 5-11 shows that materials with a Biot number of 0.11 or less ignited which is as expected as these are classified as thermally thin (88). However, Figure 5-1 shows that a number of materials with a similar Biot number did not ignite.

Based on the criteria of 40 kW m^{-2}, it would be expected that at least materials with a Biot number of less than 0.1 would ignite during the fireball phase. Therefore further investigation into the material properties other than Biot number is required.

Although, the calculation of thermal dose is the product of time and thermal radiation flux, a plot of thermal dose against time is shown in Figure 5-12 to provide context on the timescales for ignition.

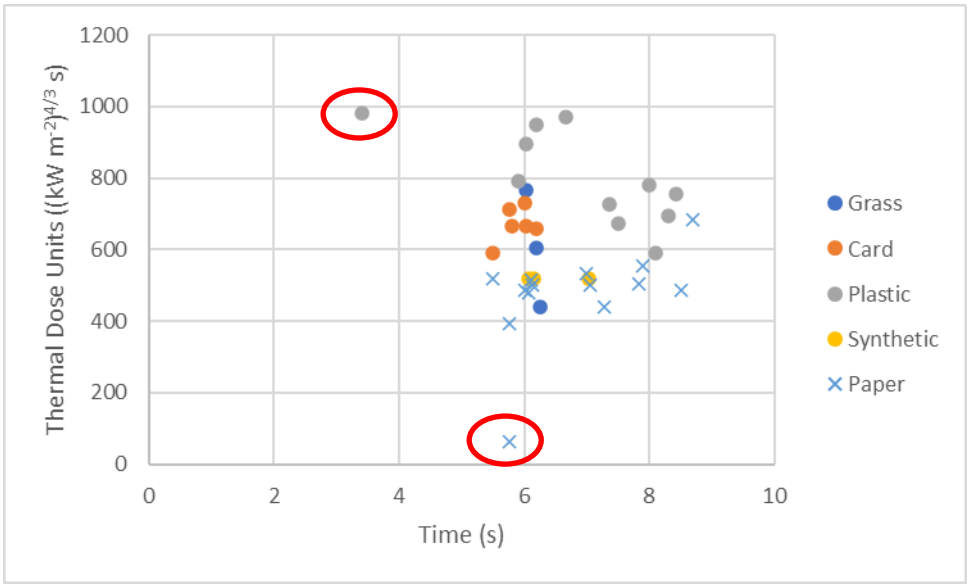

Figure 5-12 Igntion of materials in the transient tests

Figure 5-12 shows that ignition was mainly obtained on attainment of the maximum heat flux and that tests were repeatable i.e. within the envelope of 400-1000 thermal dose units and 6 – 8 seconds. The plastic and paper sample results outside this envelope (circled in red) occurred due to the edges of the sample folding under heat exposure during the test.

The study examined the ignition of wood edges, revealing no signs of ignition. Edge effects in other materials were not fully investigated in this study, however in Figure 5-13, the sample folded as it was raised upwards and lead to earlier ignition than other tests were the paper di not fold. Therefore, this suggest additional research would be warranted in this area.

Figure 5-13 Example of sample folding druing tests

The spontaneous ignition data for card, paper and 0.2 mm plastic was compared with Martin predictions for thermally thin materials (Equation (2-37)) in Figure 5-14. The value t_c is defined as time to reach critical heat flux in Section 2.7.6.2 and therefore was calculated by measuring the time to reach the experimental setup took to raise the sample holder to a value of 20 kW m^{-2}.

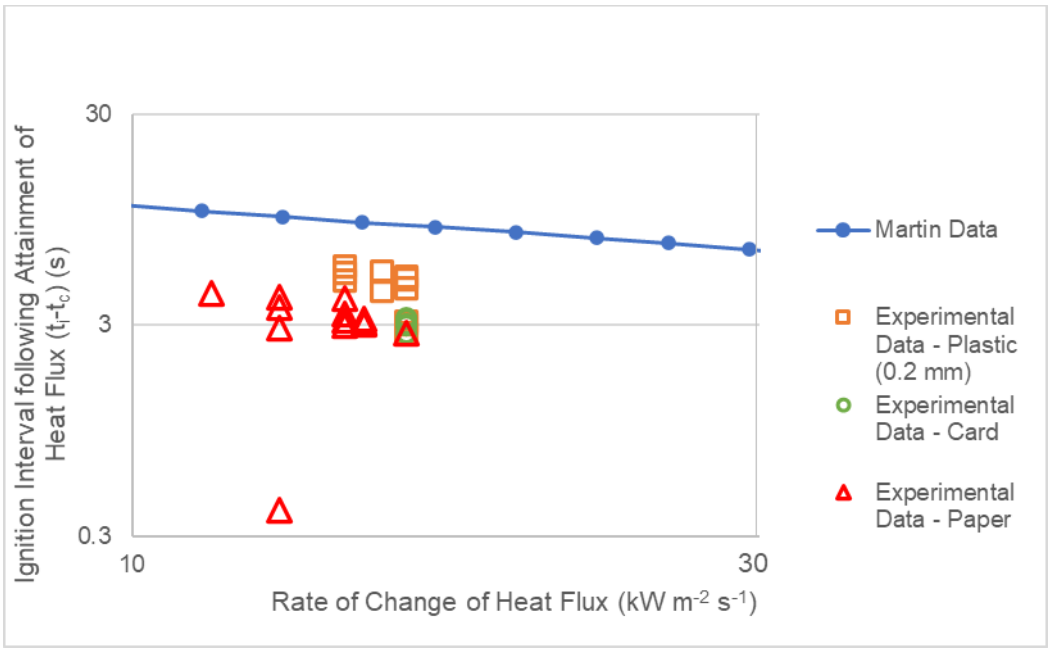

Figure 5-14 Comparison of experimental data with Martin predictions

The Martin predictions are a correct order of magnitude, however, the Martin predictions are not a conservative prediction. This research has not been able to validate other rate of change of heat fluxes, as this factor is generally the same at different distances from the release and for all fireball releases irrespective of diameter.

To demonstrate this, the rate of change of heat flux for the laboratory scale experiments is 11-16 W cm^{-2} s^{-1} which is based on the large scale test carried out. Analysis of Lowesmith's data (59) has been carried been using 'Engauge Digitizer' (125) and compared with the laboratory scale change in heat flux, see Figure 5-15.

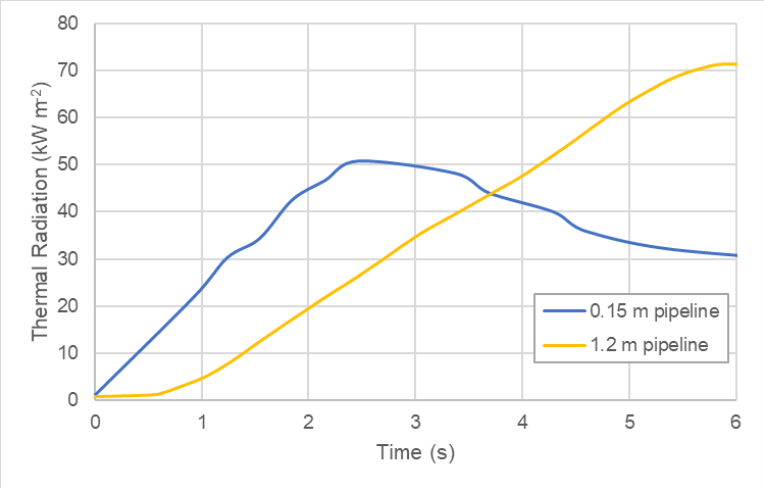

Figure 5-15 Comparison of rate of change in heat flux in the near field for two different sized pipelines

Figure 5-15 shows the rate of change of heat flux is 20 W cm^{-2} s^{-1} for the 0.15 m diameter pipeline and 12 W cm^{-2} $s^{-1}$for the 1.2 m diameter pipeline. Therefore the conclusions in this study would be valid for other pipeline diameters but further research should be undertaken where different rates of change in thermal radiation flux are present before using the Martin equations.

5.1.7. Temperature measurements

Video records of temperature measurements were undertaken as described in Section 3.2.9. The records show that samples reached temperatures in excess of 200°C. The results show that only a temperature range could be determined from the thermal imaging camera, therefore data capture could be improved by the use of sensors within the sample.

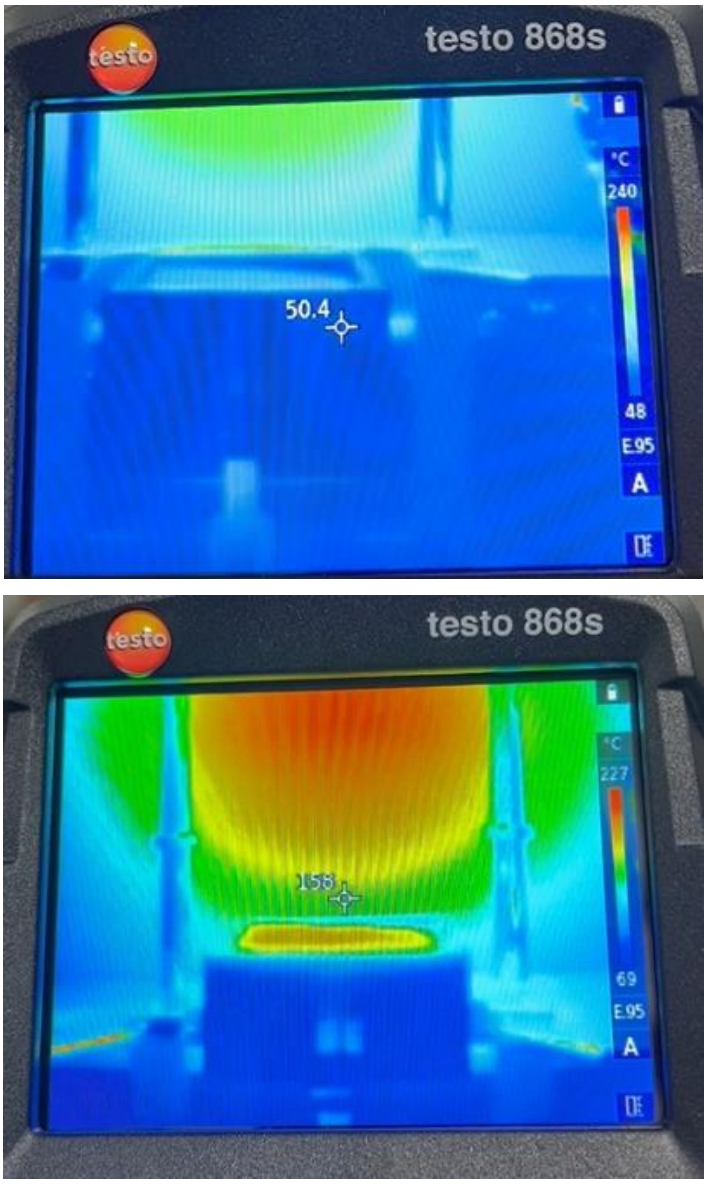

Figure 5-16 Temperature measurement of sample on the whilst being raised (left) and lowered (right)

5.2. Steady State Tests

For the steady state tests, samples of plastic with 3 different thicknesses, paper and cardboard were positioned on the sample holder 12.5 mm away from the heating element of the cone. These steady state tests were carried out with both a pilot and with no pilot present to investigate the potential for using a thermal dose for predicting ignition (see Equation (2-32)). The results are shown in Figure 5-17 and Figure 5-18, with trendlines fitted to give an indication of a fit of the data for the different materials tested.

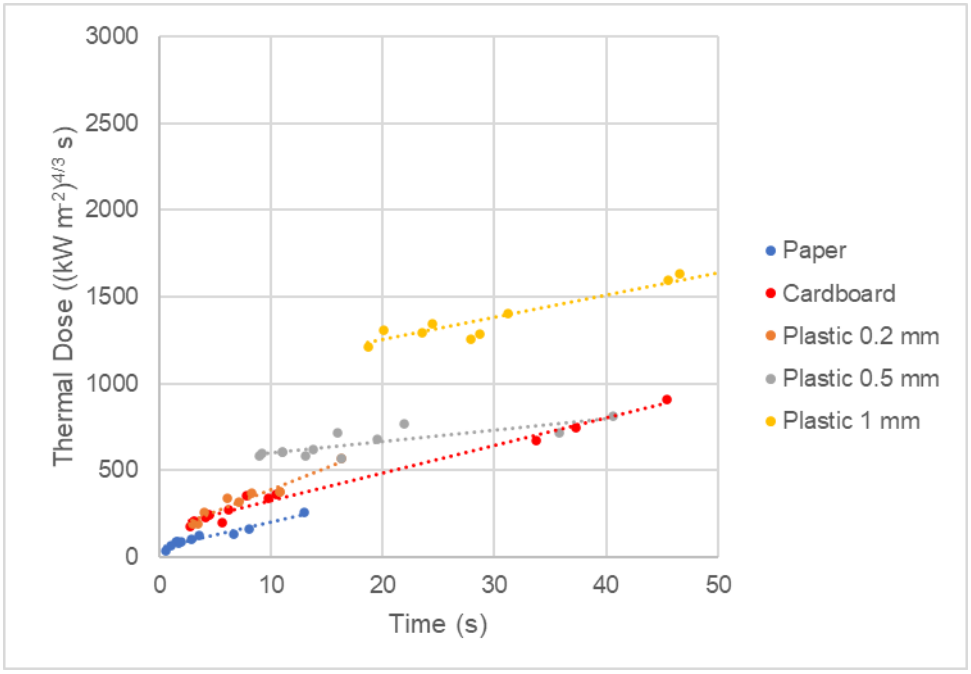

Figure 5-17 Thermal dose for piloted ignition - steady state exposure

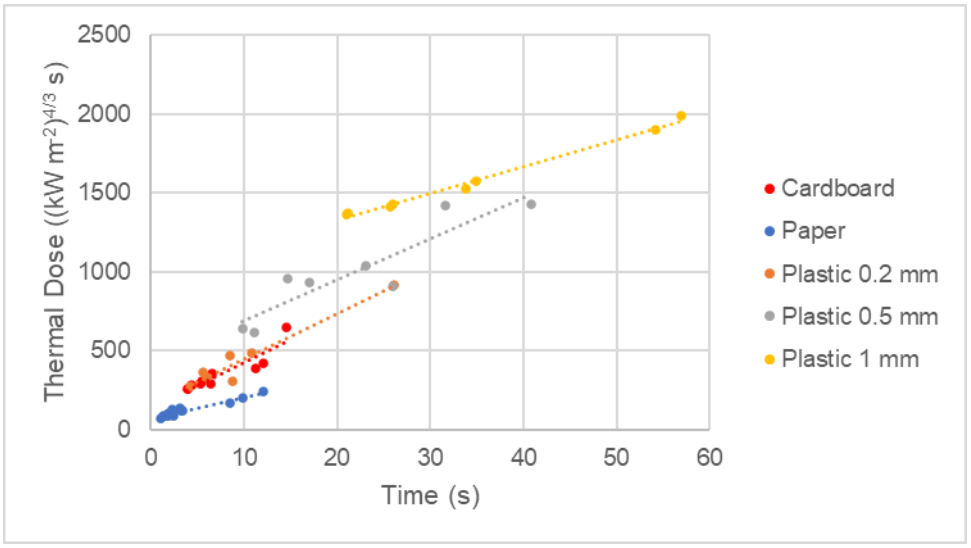

Figure 5-18 Thermal dose for spontaneous ignition - steady state exposure

5.3. Analysis

The thermal dose required to cause ignition in the steady state tests have been compared with the results for the transient tests in Table 5-2.

Table 5-2 Comparison of thermal dose required under different test conditions

Material	Steady State Exposure		Transient - Thermal Dose required for spontaneous ignition (kW m^{-2})$^{4/3}$ s)
	Thermal Dose required for piloted ignition (kW m^{-2})$^{4/3}$ s)	Thermal Dose required for spontaneous ignition ((kW m^{-2})$^{4/3}$ s)	
Card	644 - 2468	1019 - 2316	591 – 729
Paper	146 - 705	271 - 651	392 - 685
Polyethylene (0.2 mm)	732 – 1233*	996 – 2988*	591 - 971
Polyethylene (0.5 mm)	1866 - 2511	2330 – 5064*	No ignition
Polyethylene (1 mm)	4472 - 7285	5381 – 6510*	No ignition
* No ignition at 20 kW m^{-2}			

The results suggest that transient exposures require lower thermal doses compared to steady-state tests. Although, there was no ignition of the 0.5 or 1 mm polyethylene samples during the transient tests. The calculations above have utilized Equation (2-32) without alteration, maintaining the 4.3 exponent. Similar trends are obtained when using an exponent of 1. Based on the method employed by Eisenberg (81), it was anticipated that the thermal dose required for ignition should remain consistent regardless of a steady state or transient exposure. Therefore there must be other parameters other than thermal radiation flux and duration of exposure that affect ignition.

To enable a robust statistical analysis to be carried, the video records were examined to identify the first time that visible smoke was observed. This was achieved by examining the frame by frame images as shown in Figure 5-19. This point has been utilized as it is predicted to be the point at which the temperature at the surface is in the range of 200-260°C (88). This is particularly relevant as hemicellulose begins to release smoke at this temperature (for cardboard and paper samples). The surface temperature at the point of ignition is assumed to be 300°C (89).

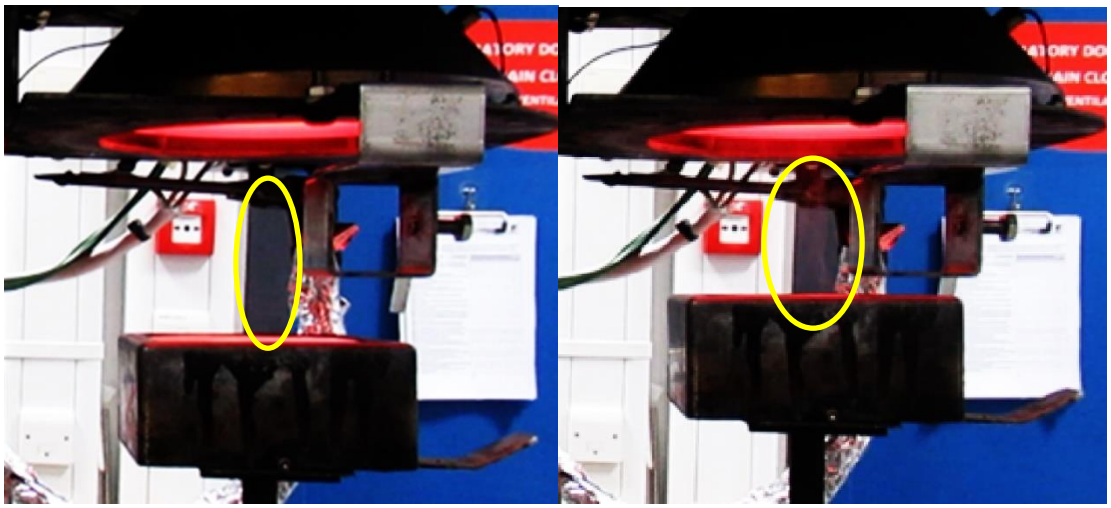

Figure 5-19 Example analysis of video records for smoke observations

Microsoft Excel was used to carry out multivariate linear regression analysis of the results. Multivariate linear regression analysis is a statistical technique that uses more than one independent variable to predict the outcome of a dependent variable. To carry out the analysis, the thermal dose was assumed to be function of density, thermal conductivity, specific heat capacity and thickness. The form of the equation used was:

$$L = Constant \rho^{p_1} h^{p_2} c_s^{p_3} l_t^{p_4} \quad \textbf{(5-1)}$$

As Equation (5-1) is a non-linear power correlation, this equation was transformed into a linear from by taking the natural logs as shown in Equation (5-2).

$$ln(L) = ln(Constant) + p_1\, ln(\rho) + p_2\, ln(h) + p_3\, ln(c_s) + p_4 ln(l_t) \quad \textbf{(5-2)}$$

In Equation (5-2), ln(constant) is the intercept, ln(L) is the dependent variable and p_1 to p_4 are the coefficients to be determined. The independent values used for density, thermal conductivity, specific heat capacity and thickness are shown in Table 5-3.

Table 5-3 Parameters used for the materials tested

Material	Density, ρ (kg m^{-3})	Thermal Conductivity, h (W m^{-1} K^{-1})	Specific heat capacity, c_s (J kg^{-1} K^{-1})	Thickness, l_t (mm)
Paper (Cellulose)	398.67	0.039 (116)	1.3 (88)	0.19
Cardboard	720.68	0.039 (116)	1.3 (88)	0.32
Polyethylene	478.82	0.4 (88)	2.1 (88)	0.20
Polyethylene	1074.76	0.4 (88)	2.1 (88)	0.50
Polyethylene	1307.28	0.4 (88)	2.1 (88)	1.00

The results of the multivariate regression analysis for the smoke observations are shown in Figure 5-20 with a plot of predicted thermal dose and the value measured from the experiments. The results of statistical tests to confirm the accuracy of the fit are shown in Table 5-4.

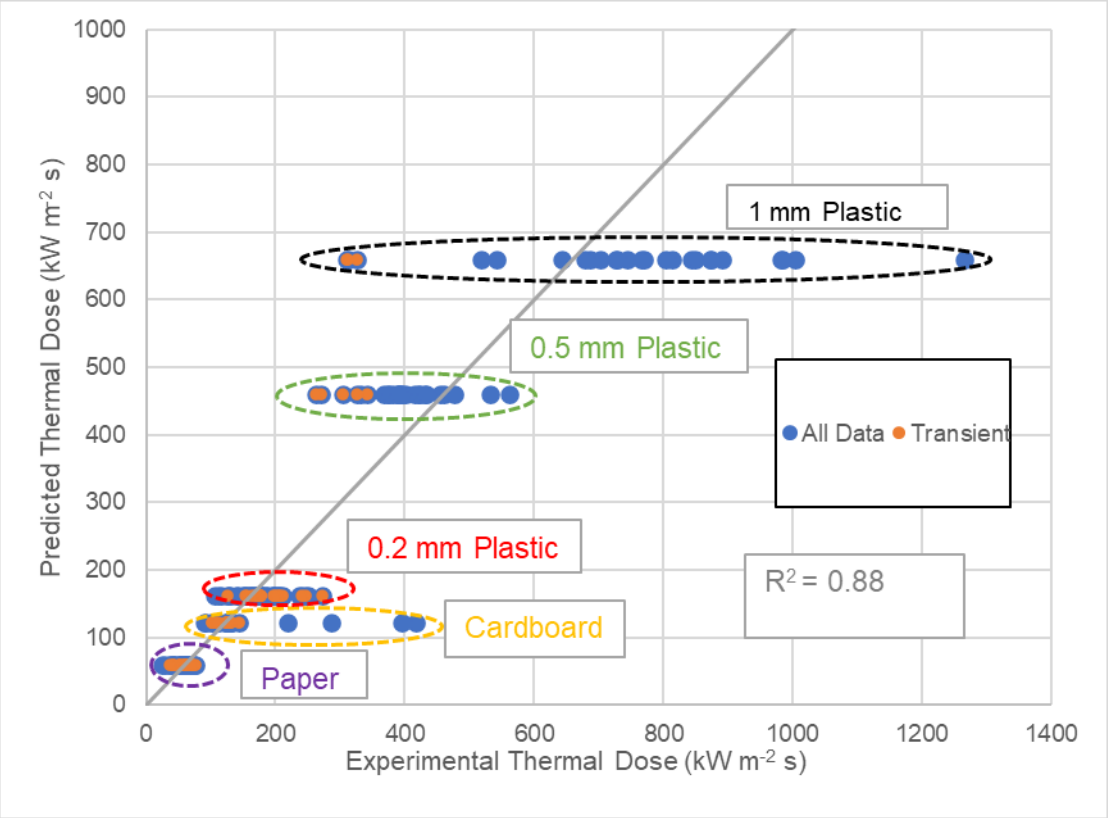

Figure 5-20 Results of multivariate regression analysis for smoke observations with 4 coefficients

Table 5-4 Statistical tests of the fit for data in Figure 5-20

Parameter	Coefficient	Standard Error	t Stat	P-value
Intercept	-0.65	1.58	-0.41	0.68
p_1 (Density)	1.04	0.22	4.80	4×10^{-6}
p_2 (Thermal conductivity)	0.34	0.03	12.69	N/A
p_3 (Specific heat capacity)	0	0	65535	N/A
p_4 (Thickness)	0.23	0.16	1.44	0.15

For the analysis the 4/3 exponent was initially varied and it was observed that an exponent of 1 yielded a more favourable coefficient of determination. A lower exponent shows the built environment is less sensitive to the thermal radiation flux than for human exposure.

To provide assurance in the derived coefficients a range of statistical tests were carried out. The standard error shows a percentage variability or uncertainty associated with the sample estimate of a population parameter. The values calculated above are reasonable with respect to standard error. The t stat is how many standard errors a sample estimate is from a proposed value. P values are used with t stat to determine the statistical significance, with lower values indicating that derived results are unlikely to have occurred by chance alone.

One unsatisfactory result is the zero value for the specific heat capacity coefficient. Investigation into different specific heat capacity values for paper and card yields a relatively high coefficient (~3) for the specific heat capacity. It is postulated that this due to similar specific heat values for the materials used in this research. Therefore the analysis without this coefficient was re-run with the results shown in Figure 5-21 and Table 5-5.

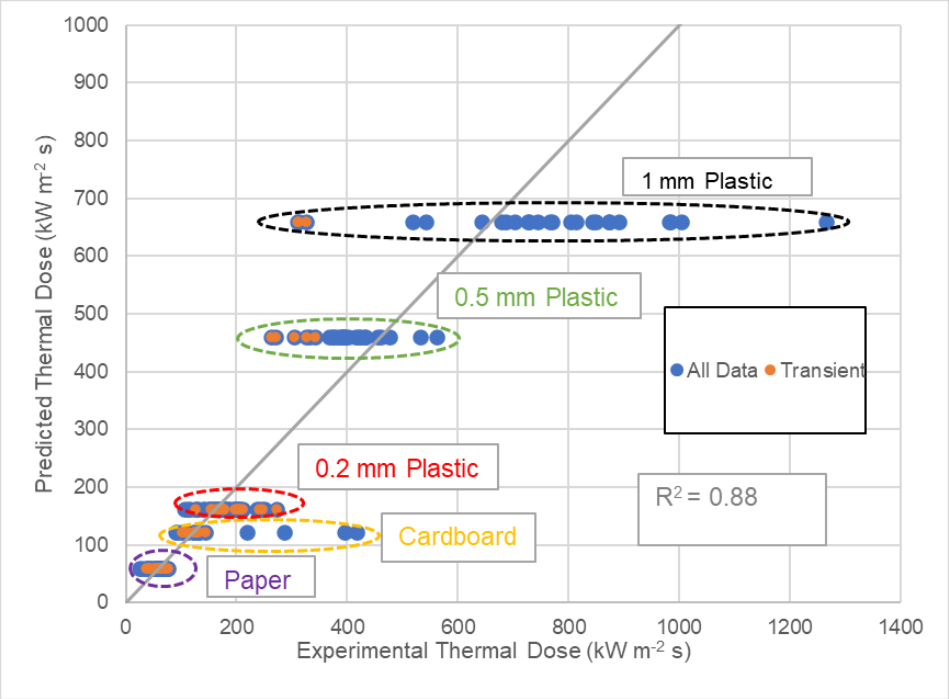

Figure 5-21 Results of multivariate regression analysis for smoke observations with 3 coefficients

Table 5-5 Statistical tests of the fit for data in Figure 5-21

Parameter	Coefficient	Standard Error	t Stat	P-value
Intercept	-0.65	1.58	-0.41	0.68
p_1 (Density)	1.04	0.22	4.80	4.0×10^{-6}
p_2 (Thermal conductivity)	0.34	0.03	12.69	5.6×10^{-25}
p_4 (Thickness)	0.22	0.16	1.44	0.15

Logically, the results are intuitive. As density, thermal conductivity, and thickness increase, the thermal dose necessary for production of smoke also rises. This is illustrated by Figure 5-21, which shows thermal dose ascending for paper (purple circle) and cardboard (yellow circle). The same trend is also shown for 0.2 mm (red circle), 0.5 mm (green circle) and 1 mm plastics.

The statistical analyses, coupled with a coefficient of determination of 0.88, provide confidence that the relationship between the thermal properties of a material and the dosage required for ignition is accurate. While additional testing on a broader range of materials is necessary, this research supports that refinements in the criteria for assessing whether a material would ignite is warranted.

5.3.1. Implications for Risk Assessment

In Section 2.1.1, reference was made to hazard distances for a 0.273 m diameter pipeline operating at 38 bar. To demonstrate the practical application of this research, distances at which the thermal dose required to induce smoking, as well as piloted and spontaneous ignition of paper, have been calculated and compared with equivalent piloted and spontaneous ignition previously provided in Section 2.1.1. The distances to specific thermal doses will be influenced by the mass of gas released, as detailed in Section 4, which affects the fireball duration. To illustrate the effect the use of thermal dose could have on pipeline risk assessment, the distances given in Table 5-6 are based on a fireball reaching a peak in 6 seconds, followed by a decline to zero within an additional 6 seconds.

While the study has been carried out for plastic, paper and cardboard, the correlation using the coefficients given in Table 5-5 has also been used to calculate the thermal dose required to cause smoking, piloted ignition and spontaneous ignition of hardboard with a density of 878 kg m^{-3}, a thermal conductivity of 0.05 W m^{-1} K^{-1} and a thickness of 0.95 mm (93) in Table 5-6.

Table 5-6 Comparsion of thermal dose criteria and with current data (For illustration only)

Method of Determination for hazard distance	Distance for smoking (m)	Piloted Ignition (m)	Spontaneous Ignition (m)
Fixed thermal radiation level for Wood	-	69.5 (12 kW m^{-2})	16.6 (32 kW m^{-2})
Thermal Dose for Paper	75 (60 TDU)	35 (122 TDU)	25 (142 TDU)
Thermal Dose for Wood	0 (212 TDU)	0 (542 TDU)	0 (926 TDU)
Thermal Dose for 1 mm Plastic	0 (660 TDU)	0 (1334 TDU)	0 (1792 TDU)

The zero distance values in Table 5-6 imply that the derived correlation formula could permit a building to be sited on a pipeline with sustaining significant damage from thermal radiation during the fireball phase. Practically, consideration would also need to be given to the physical parameters of the fireball since the above does not include effects of being engulfed within a fire and also the resulting crater fire that may result after the fireball. Overall it highlights the current approach for buildings is conservative with respect to ignition of the built environment from a fireball.

CHAPTER 6

CONCLUSIONS AND FUTURE WORK

6.1. Conclusions

6.1.1. Large Scale Tests

This research began with an opportunity to capture data from two large scale fracture propagation tests. While the literature review revealed the existence of several models capable of predicting outflow with sufficient accuracy, the tests enabled data on gas outflow rates to be gathered. In this research, the TNO Yellow Book method was employed. Although the TNO Yellow Book did not accurately predict the outflow rate for the initial phases, this discrepancy was attributed to the instantaneous loss of a section of the pipeline, following review of the video footage. However, the TNO Yellow Book method for calculation for outflow rate provided sufficient accuracy to estimate the thermal radiation in the near field for the large scale experimental data.

Knowledge of the outflow enabled the thermal radiation from the subsequent fireball to be calculated using the method described by Wang. In this research it was found that the fraction of heat radiated for natural gas was adjudged to be 0.3 in line with other reported data as opposed to 0.6 using the method quoted by Wang.

There is the possibility that the underprediction of the TNO Yellow Book method may cancel out overprediction of Wang, it is important to note the impact this could have on the calculations. In this case the overall mass released was known and the alternative values for fraction of heat radiated were used in the study.

Empirical correlations based on BLEVE experiments were used to predict the dimeter of the fireball. However, it was observed that these correlations tended to overpredict the diameter. This discrepancy is suggested to be a result of the staggered gas release rate from the pipeline, contrasting with the instantaneous release of flammable material characteristic of BLEVE events.

Overpressure hazards for natural gas were found to be insignificant compared to thermal radiation hazards as is currently reported in the literature.

6.1.2. Laboratory Scale Tests

A review of the primary hazards associated with natural gas transmission pipeline ruptures was undertaken. With respect to thermal radiation hazards, the criteria for

determining whether buildings ignite rely on fixed fluxes. However, observations from incidents revealed that the application of these fixed thermal radiation fluxes did not consistently result in building ignition and thus warranted further research. Compiling data from the large scale tests facilitated an examination of alternative methods for predicting the ignition of materials to be explored. Subsequently, a new experimental laboratory scale set up was developed.

The newly developed experimental laboratory scale setup successfully replicated fireball exposure and permitted materials to be subjected to varying heat fluxes. When comparing the laboratory scale thermal dose exposure with the large scale experimental data, a coefficient of 0.97 was obtained demonstrating that the laboratory scale setup accurately replicates the large scale tests.

Beyond fireballs, the laboratory setup could be used to research other applications, by adjusting the speed of the sample's rise or fall of a sample for example. Applications of interest in this context include the assessment of material responses to detonations, real fires and military scenarios that would otherwise be costly to replicate at large scale.

In this study, the investigation focused on the thermal dose linked to both spontaneous and piloted ignition across various materials. The application of the Biot number did not yield definitive results, as, in some instances, thermally thin samples ignited under transient doses, while other thermally thin materials did not ignite under equivalent test conditions. Steady-state tests were carried out to enable comparisons with the thermal dose needed for ignition in transient tests. It became evident that different thermal doses were necessary to induce ignition. The analysis of the Biot number, coupled with these findings, underscored the need to consider other parameters in the study.

In addition to the data on pilot and spontaneous ignition, video records were scrutinized to pinpoint the initial appearance of smoke during the tests. This facilitated a statistical analysis of three sets of data, with physical properties of the materials tested included. This approach proved successful, with a correlation for predicting ignition across limited set of materials that had a coefficient of 0.88. Application of the derived correlation with respect to the built environment highlighted that the current approach is conservative.

Considering the potential for multiple fatalities arising from gas pipeline releases, it is not proposed to alter the current limits. However, the current study does support that further research may lead to more precise criteria for the built environment.

The research also yielded observations that can be valuable for emergency response and incident investigation. For instance, when exposed to the high thermal radiation

fluxes characteristic of the near field of a fireball, painted wood was noted not to blister or scorch, and vegetation with high water content appeared unaffected.

6.2. Limitations of the Study

The primary limitation of this study is that the large scale data collection was conducted with natural gas. Although the insights regarding thermal radiation are applicable to other fuels with necessary adjustments made to variables like the fraction of heat radiated, it is crucial to note the recent interest in transitioning the transmission network to hydrogen. It has been recognised that while overpressure hazards are not prominent for natural gas, they could be significant for hydrogen. Consequently, further research is needed in this area.

In the small scale testing there was not sufficient variation (nor direct determination) of fundamental properties such as specific heat capacity and thermal conductivity with the consequence of uncertainty on the dependence on these parameters in transient thermal exposure scenarios. The purpose of this study was to establish whether there was a potential for such a relationship to be established and therefore a more methodical study should address these issues.

6.3. Recommendation for Future Research

During the course of this research, a number opportunities for further work have been identified.

Large scale tests could be undertaken to investigate the effect of wind direction on the fireball formation. Further tests could also provide further insights into gas release rate and thermal radiation hazards.

Experiments involving various materials were conducted, and in several instances, no ignition was observed, but there was limited visible damage. The laboratory scale setup developed in this research has the potential for modification, enabling the monitoring of material temperature and real-time mass loss rate. This modification could offer fundamental insights into how heat is transferred through solids during changes in heat flux.

The laboratory scale setup developed in this research could be used to test an array of materials encompassing a wider range of parameters which would allow for more rigorous statistical analyses. Examples of parameters to be explored include specific heat capacity and composite materials. This expanded testing capability facilitates the identification of critical parameters in exposure over time with greater precision.

Additionally, the laboratory scale setup could be utilised to explore wetted materials, such as cardboard, providing insights into the effect of water on ignition that could also inform ignition of vegetation.

Finally, it was observed that lower heat fluxes from the large scale tests exhibited a more asymmetrical form and the speed of the rise and fall could be adjusted to explore the impact this variation has on ignition.

REFERENCES

1. **Administration, US Energy Information. Global natural gas consumption doubled from 1980 to 2010 - Today in Energy - U.S. Energy Information Administration (EIA).**

2. **DNV. Energy Transistion Outlook. [Online] 2022. [Cited: 23 May 2023.] www.dnv.com/eto.**

3. **IGEM. *Steel pipelines for high pressure gas transmission.* Kegworth : IGEM, 2021. IGEM/TD/1 Edition 6.**

4. **EGIG. 11th EGIG Report. [Online] December 2020. [Cited: 6 February 2023.] https://www.egig.eu/reports/$60/$61.**

5. **U.S. Oil and Gas Pipeline Mileage. *Bureau of Transportation Statistics.* [Online] 2021. [Cited: 7 February 2023.] https://www.bts.gov/content/us-oil-and-gas-pipeline-mileage.**

6. **PHMSA. All Reported Incident 20 Year Trend. [Online] 2022. [Cited: 7 February 2023.] https://www.phmsa.dot.gov/data-and-statistics/pipeline/pipeline-incident-20-year-trends.**

7. **Pipelines. *Central Intelligence Agency.* [Online] 2023. [Cited: 7 February 2023.] https://www.cia.gov/the-world-factbook/field/pipelines.**

8. **Oil and Natural Gas Pipelines. *Canadian Association of Petroleum Producers.* [Online] 2023. [Cited: 7 February 2023.] https://www.capp.ca/explore/oil-and-natural-gas-pipelines/#:~:text=Transmission%20pipelines%20are%20large%2Ddiameter,117%2C000%20km%20of%20transmission%20pipelines..**

9. **Africa's Gas Infrastructure: December 2022. *Global Energy Monitor.* [Online] [Cited: 25 February 2024.] https://globalenergymonitor.org/wp-content/uploads/2022/11/GEM-Scramble-for-Africas-Gas.pdf.**

10. **Health and Safety Executive (HSE). A guide to the Pipelines Safety Regulations 1996. [Online] [Cited: 1 June 2023.] https://www.hse.gov.uk/pubns/priced/l82.pdf.**

11. **HSE. A guide to the Gas Safety (Management) Regulations. Guidance on Regulations. [Online] 1996. [Cited: 1 June 2023.] https://www.hse.gov.uk/pubns/priced/l80.pdf. 9780717611591.**

12. **HSE. A guide to the Control of Major Accident Hazards Regulations (COMAH) 2015. *Health and Safety Executive.* [Online] [Cited: 1 June 2023.] https://www.hse.gov.uk/pubns/priced/l111.pdf.**

13. **American Society of Mechanical Engineers. *Gas transmission and distribution piping systems.* New York : ASME, 2016.**

14. **BSI. *Pipelines For Maximum Operating Pressure Over 16 Bar : Functional Requirements.* Chiswick : BSi, 2013.**

15. IChemE. Hazards 8. *Safety and Loss Prevention.* [Online] [Cited: 1 June 2023.] https://www.icheme.org/media/11993/viii-paper-03.pdf.

16. Rew, P. *Cloud Fires.* Leeds : University of Leeds, Fire Dynamics Conference, 2014.

17. IGEM. *Assessing the risks from high pressure natural gas pipelines.* Kegworth : IGEM, 2013. IGEM/TD/2 Edition 2.

18. Bilo, M. and Kinsman, R. *Thermal radiation criteria used in pipeline risk assessment.* Bootle : Pipes & Pipelines, 1997.

19. Department of Transportation. State of the National Pipeline Infrastructure. [Online] [Cited: 18 March 2018.] https://www.hsdl.org/?view&did=804318.

20. National Transportation Safety Board (NTSB). PAR77-1. [Online] 1976. https://www.ntsb.gov/safety/safety-recs/recletters/P76_74_75.pdf.

21. NTSB. *Natural Gas Pipeline Rupture and Fire Near Carlsbad, New Mexico.* 2003. PAR 03/01. [Online] https://www.ntsb.gov/investigations/AccidentReports/Reports/PAR0301.pdf.

22. NTSB. Cleburne Natural gas transmission pipeline rupture and fire. [Online] 2013. https://www.ntsb.gov/investigations/AccidentReports/Reports/PAB1302.pdf.

23. NTSB. Natural Gas Transmission Pipeline Rupture and Fire San Bruno, California, Report No.: PAR1101. [Online] 2011. https://www.ntsb.gov/investigations/AccidentReports/Reports/PAR1101.pdf.

24. NTSB. Columbia Gas Transmission Corporation Pipeline Rupture Sissonville, West Virginia. [Online] 2014. https://www.ntsb.gov/investigations/AccidentReports/Reports/PAR1401.pdf.

25. ARIA. Rupture and ignition of a gas pipeline. [Online] 2009. https://www.aria.developpement-durable.gouv.fr/wp-content/files_mf/FD_27681_Ghislengheinv_2004ang.pdf.

26. Government Inspectorate of Mines. Thermal Damage from Belgium Gas Pipeline Incident. [Online] http://miningquiz.com/pdf/Disasters/PijplijnongevalteGell_ENG.pdf.

27. Cleaver, R.P., Cumber P.S. and Genillon, P. *A Model to Predict the Characteristics of Fires Following the Rupture of Natural Gas Transmission Pipelines.* Loughborough : IChemE, 2001. Vol. 79.

28. Oikonomidis, F., Shterenlikht, A. and Truman, C.E. *Prediction of crack propagation and arrest in X100 natural gas transmission pipelines with the strain rate dependent damage model (SRDD). Part 1: A novel specimen for the measurement of high strain rate fracture properties and validation of the SRDD model.* Bristol : International Journal of Pressure Vessels and Piping, 2013. Vol. 60.

29. Chen, C., Sheen, Y-N. and Wang, H-Y. *Case analysis of catastrophic underground pipeline gas explosion in Taiwan.* Taiwan : Engineering Failure Analysis, 2016. Vol. 65.

30. Lowesmith, B.J., Hankinson, G., Acton, M.R. and Chamberlain, G. *An Overview of the Nature of Hydrocarbon Jet Fire Hazards in the Oil and Gas Industry and a Simplified Approach to Assessing the Hazards.* Loughborough : Process Safety and Environmental Protection., 2007. Vol. 85(3).

31. Acton, M. R., Hankinson, G., Ashworth, B. P., Sanai, M. and Colton, J. D. *A Full Scale Experimental Study of Fires Following the Rupture of Natural Gas Transmission Pipelines.* Loughborough : ASME, 2000.

32. Mannan, S. *Lees' Loss Prevention in the Process Industries.* Oxford : Elsevier Butterworth-Heinemann, 2012.

33. Johnson, D. M., Pritchard, M. J. and Wickens, M. J. *Large Scale Catastrophic Releases of Flammable Liquids.* Solihull : British Gas, 1990. Vols. Report No.: Commission of the European Communities, Report EV4T.0014.

34. Zhang, Q. and Liang, D. *Thermal Radiation and Impact Assessment of the LNG BLEVE Fireball.* Guangzhou : Procedia Engineering. 2013, 2013. Vol. 52.

35. BSi. *Fire tests on building materials and structures.* Chiswick : BSi, 2004. BS 476-3.

36. Cleaver, R. P. and Halford, A. R. *A model for the initial stages following the rupture of a natural gas transmission pipeline.* Loughborough : Process Safety and Environmental Protection, 2015. Vol. 95.

37. Perry, R. H., Green, D. W. and Maloney, J. O. *Perry's chemical engineers' handbook, 7th Edition.* New York : McGraw-Hill, 1997.

38. Vagabond, J. Turbulent Flow and Viscosity. *Physics and Chemistry for IG and A level.* [Online] 2012. [Cited: 16 February 2023.] https://esfsciencenew.wordpress.com/2012/10/26/turbulent-flow-and-viscosity/.

39. COMSOL. What Are the Navier-Stokes Equations? [Online] [Cited: 27 March 2018.] https://www.comsol.com/multiphysics/navier-stokes-equations.

40. Holland, F. A. and Bragg, R. *Fluid flow for chemical engineers, 2nd Edition.* Oxford : Butterworth-Heinemann, 1999.

41. OGP. *Consequence Modelling, Report No.: 434–07.* London : s.n., 2010.

42. Bariha, N., Mishra, I. M. and Srivastava, V. C. *Hazard analysis of failure of natural gas and petroleum gas pipelines.* Uttarakhand : Journal of Loss Prevention in the Process Industries, 2016. Vol. 40.

43. Tu, J., Yeoh, G. H. and Liu, C. *Computational fluid dynamics: a practical approach. 2nd Edition.* Amsterdam : Elsevier, 2013.

44. Acton, M. R. *The Application of Risk Assessment to Routing Issues for Gas Transmission Pipelines.* Loughborough : IChemE, 2007. Vol. 7.

45. Mahgerefteh, H., Oke, A. O. and Rykov, Y. *Efficient numerical solution for highly transient flows.* London : Chemical Engineering Science., 2006. Vol. 61(15).

46. TNO. ***Yellow Book - Methods for the Calculation of Physical Effects. Report No.: CPR 14E.*** **The Hague : TNO, 1996.**

47. Unitrove. Natural Gas Density Calculator. ***Unitrove.*** **[Online] [Cited: 23 10 2023.] https://www.unitrove.com/engineering/tools/gas/natural-gas-density.**

48. Luccioni, B., Ambrosini, D., Nurick, G. and Snyman, I. ***Craters produced by underground explosions.*** **Tucumán : Computers & Structures., 2009. Vols. 87(21–22).**

49. NEN. ***Additional requirements for pipelines in or nearby important public works.*** **Delft : NEN, 202. NEN 3651.**

50. PRCI. ***Line Rupture and the Spacing of Parallel Lines.*** **Chantilly : PRCI, 2002. Report No. L51861.**

51. McGillivray, A. Review of the event tree structure and ignition probabilities used in HSE's pipeline risk assessment code MISHAP. ***HSE.*** **[Online] [Cited: 29 Apr 2018.] http://www.hse.gov.uk/research/rrpdf/rr1034.pdf. Report No.: RR1034.**

52. Gastec, Arup and Kiwa. ***Work Package 7, Safety Assessment: Conclusions Report (Incorporating Quantitative Risk Assessment).*** **London : Hy4Heat, 2021. Report ARP-WP7-GEN-REP-0005, Version 1.0.**

53. Spencer, H., Rew, P. J. ***Ignition probability of flammable gases.*** **Sudbury : HSE Books, 1997.**

54. American Institute of Chemical Engineers. ***Guidelines for chemical transportation risk analysis.*** **New York : Center for Chemical Process Safety of the American Institute of Chemical Engineers, 1995.**

55. Spencer, H., Rew, P. J. and Daycock, J. H. ***A model for the ignition probability of flammable gases: phase 2.*** **Sudbury : HSE Books, 1998.**

56. Acton, M. and Baldwin, P. ***Ignition Probability for High Pressure Gas Transmission Pipelines.*** **Calgary : ASME, 2008.**

57. TNO. ***Green Book - Methods for the determination of possible damage.*** **The Hague : TNO, 1992. Report No.: CPR 16E.**

58. Chemical Industires Association. ***Guidance for the location and design of occupied buildings on chemical manufacturing sites.*** **London : CIA, 2010.**

59. Lowesmith, B. J. and Hankinson, G. ***Large scale experiments to study fires following the rupture of high pressure pipelines conveying natural gas and natural gas/hydrogen mixtures.*** **Loughborough : Process Safety and Environmental Protection, 2013. Vols. 91(1–2).**

60. Florisson, O. ***The Value of the exisiting natural gas system for hydrogen, the sustainable future energy carrier (Progress obtained in the NaturalHy project).*** **Amsterdam : World Gas Conference, 2006.**

61. Raj, P. K. ***A review of the criteria for people exposure to radiant heat flux from fires.*** **Burlington : Journal of Hazardous Materials, 2008. Vol. 159(1).**

62. Hadjipanayis, M. A., Beyrau, F., Lindstedt, R. P., Atkinson, G. and Cusco, L. ***Thermal radiation from vapour cloud explosions.*** **London : Process Safety and Environmental Protection, 2015. Vol. 94.**

63. Hottel, H. C. and Sarofim, A. F. ***Radiative transfer.*** **New York : McGraw-Hill, 1967.**

64. Witlox, H., Harper, M. and Pitblado, R. Validation of Phast dispersion model as required for USA LNG Siting Applications. ***DNV.*** **[Online] [Cited: 17 June 2023.] https://brandcentral.dnv.com/download/DownloadGateway.dll?h=BE1B38BB718539CC0AB58A5FF2EA7A832BB095CBE75B38A1CD3A60A27EC7E35B99D0A0231C3D7C3F575869FA6A4795E1&_ga=2.204969168.1992436369.1687027151-333461245.1619688391.**

65. Wilday, J. ***A comparison of hazard and risks for carbon dioxide and natural gas pipelines.*** **Buxton : IChemE, 2009. Vol. 155.**

66. Witlox, H., Fernandez, M., Harper, M., Oke, A., Stene, J. and Xu, Y. ***Verification and validation of Phast consequence models for accidental releases of toxic or flammable chemicals to the atmosphere.*** **London : Journal of Loss Prevention in the Process Industries, 2018. Vol. 55.**

67. Marx, J. and Martinsen, W. E. ***An Improved Model for the Prediction of Radiant Heat from Fireballs.*** **San Francisco : International Conference and Workshop on Modeling Consequences of Accidental Releases of Hazardous Materials, 1999.**

68. Wang, K., Liu, Z., Qian, X. and Huang, P. ***Long-term consequence and vulnerability assessment of thermal radiation hazard from LNG explosive fireball in open space based on full-scale experiment and PHAST.*** **Beijing : Journal of Loss Prevention in the Process Industries, 2017.**

69. Roberts, T., Gosse, A. and Hawksworth, S. ***Thermal Radiation from Fireballs on Failure of Liquefied Petroleum Gas Storage Vessels.*** **Buxton : Process Safety and Environmental Protection, 2000. Vol. 78(3).**

70. Chamberlain, G. ***BLEVE.*** **Leeds : University of Leeds, Fire and Explosion Investigation Conference, September 2005.**

71. Pritchard, M. J. and Binding, T. M. ***FIRE2: A new approach for predicting thermal radiation levels from hydrocarbon pool.*** **Solihull : IChemE, 1992. Vol. No. 130.**

72. Dhurandher, B. K., Kumar, R. and Dhiman, A. I. ***Impact Assessment of Thermal Radiation Hazard from LPG Fireball.*** **Roorke : Procedia Earth and Planetary Science, 2015. Vol. 11.**

73. Satyanarayana, K., Borah, M. and Rao, P. G. ***Prediction of thermal hazards from fireballs.*** **Assam : Journal of Loss Prevention in the Process Industries, 1991. Vol. 4(5).**

74. Vílchez, J. A., Muñoz, M., Bonilla, J. M. and Planas, E. ***Configuration factors for ground level fireballs with shadowing.*** **Barcelona : Journal of Loss Prevention in the Process Industries, 2018. Vol. 51.**

75. McGrattan, K. Modelling Large Liquefied Natural Gas Fires. *Fire and Evacuation Modeling Technical Conference.* [Online] 2022. [Cited: 2 November 2023.] https://files.thunderheadeng.com/femtc/2022_d1-02-mcgrattan-paper.pdf.

76. Clay, G. A., Fitzpatrick, R. D., Hurst, N. W., Carter, D. A. and Crossthwaite, P. J. *Risk assessment for installations where liquefied petroleum gas (LPG) is stored in bulk vessels above ground.* Sheffield : Journal of Hazardous Materials, 1988. Vol. 20.

77. Sklavounos, S. and Rigas, F. *Estimation of safety distances in the vicinity of fuel gas pipelines.* Athens : Journal of Loss Prevention in the Process Industries, 2006. Vol. 19.

78. Rew, P. J. and Hockey, S. M. *Review of human response to thermal radiation.* Epsom : HSE, 1996. HSE Contract Research Report No. 97/1996.

79. NHS. Burns and scalds . *NHS.* [Online] [Cited: 4 April 2018.] https://www.nhs.uk/conditions/burns-and-scalds/.

80. NFPA. *Guide for Fire and Explosion Investigations.* Boston : s.n., 2021. NFPA 921.

81. Eisenberg, N. *Vulnerability Model. A Simulation System for Assessing Damage Resulting from Marine Spills.* Washington D. C. : Department of Transportation, 1975.

82. WS Atkins. *Thermal Radiation Criteria for Vulnerable populations.* Epsom : HSE, 2000. Contract Research Report 285/2000.

83. Society of Fire Protection Engineers. *Handbook of Fire Protection Engineering, 5th Edition.* Washington D. C. : SFPE, 2015.

84. Zardasti, L., Yahaya, N., Valipour, A., Rashid, A. and Noor, N. M. *Review on the identification of reputation loss indicators in an onshore pipeline explosion event.* Johor : Journal of Loss Prevention in the Process Industries, 2017. Vol. 48.

85. Daycock, J. H. and Rew, P. J. *Thermal radiation criteria for vulnerable populations.* Great Britain : HSE, 2000.

86. Jagger, S. and O'Sullivan, S. Human Vulnerability to Thermal Radiation Offshore. [Online] 2004. [Cited: 4 April 2018.] http://www.hse.gov.uk/research/hsl_pdf/2004/hsl04-04.pdf. Report No.: HSL/2004/04.

87. Zhao, Y. and Song, M. *Failure analysis of a natural gas pipeline.* Abadan : Engineering Failure Analysis, 2016. Vol. 63.

88. Drysdale, D. *An Introduction to Fire Dynamics. 3rd Edition.* Chichester : Wiley, 2011.

89. Quintiere, J. G. *Fundamental of Fire Phenomena.* Chichester : Wiley, 2006.

90. Whittaker, E. *Temperatures in heath fires.* Aberdeen : Journal of Ecology, 1961. Vol. 49.

91. Hobb, R. J., Mallik, A. U., and Gimingham, C. H. ***Studies on fire in Scottish UK heathland communities.*** **Aberdeen : Journal of Ecology, 1984. Vol. 72.**

92. Lane, A. and Tait, J. ***Maintaining and improving existing grasslands, heaths and moors in practical conservation. Grasslands, heathlands and moors.*** **Maidenhead : Open University Press, 1992.**

93. Hilado, C. J. and Murphy, R. M. ***Ignition and flash-fire studies of cellulosic material.*** **San Francisco : Fire and Materials., 1978. Vol. 2(4).**

94. Lawson, D.I. and Simms, D. L. ***The ignition of wood by radiation.*** **Borehamwood : british Journal of Applied Physics, 1952. Vol. 3.**

95. Moysey, E. B. and Muir, W.E. ***Pilot igniton of building materials.*** **Saskatchewan : Fire Technology, 1968. Vol. 4.**

96. Hilado, C. J. and Brauer, D. P. ***Ignition Testing of Fabrics and Fabric/Cushion Systems.*** **San Francisco : Fire Technology, 1979. Vol. 15.**

97. Simms, D. L. ***Experiments on the Ignition of Cellulosic Materials by Thermal Radiation.*** **Borehamwood : Combustion and Flame, 1961.**

98. Evangelista, P., Stohlgren, T., Guenther, D. and Stewart, S. ***Vegetation response to fire and postburn seeding treatments in juniper woodlands of the grand staircase-escalante national Monument, Utah.*** **Provo : Western North American Naturalist, 2004. Vol. 64(3).**

99. Tropical Savannas CRC & Bushfire CRC. Fire Ecology: Effects of fire on plants and animals. [Online] [Cited: 10 April 2018.] http://learnline.cdu.edu.au/units/env207/ecology/individual.html.

100. Scottish Environment Protection Agency. Environmental Risk Tolerability for COMAH Establishments. ***Chemical and Downstream Oil Industries Forum.*** **[Online] [Cited: 4 August 2018.] https://www.sepa.org.uk/media/219154/cdoif_guideline__environmental_risk_assessment_v2.pdf. Report No.: Version 2.**

101. Planas, E., Pastor, E., Casal, J. and Bonilla, J. M. ***Analysis of the boiling liquid expanding vapor explosion (BLEVE) of a liquefied natural gas road tanker: The Zarzalico accident.*** **Barcelona : Journal of Loss Prevention in the Process Industries, 2015. Vol. 34.**

102. Johnson, E.A. and Miyanishi, K. ***Forest fires: behavior and ecological effects.*** **San Diego : Calif: Academic Press, Inc, 2001.**

103. Auburn University. Environmental Effects. [Online] 28 March 2018. http://www.auburn.edu/academic/forestry_wildlife/fire/effects.htm.

104. Simms, D. ***On the Pilot Ignition of Wood by Radiation.*** **Borehamwood : Combustion and Flame, 1963. Vol. 7.**

105. Lizhong, Y., Zaifu, G., Yupeng, Z. and Weicheng, F. ***The influence of different external heating ways on pyrolysis and spontaneous ignition of some woods.*** **Hefei : Journal of Analytical and Applied Pyrolysis, 2007. Vol. 78(1).**

106. Martin, S. B. ***Prediction of ignition thresholds during ramp heating.*** **Redwood City : American Society for Testing and Materials, 1983.**

107. Cleaver, R. P. and Cumber, P. S. ***Modelling pipeline decompression during the propagation of a ductile fracture.*** **Loughborough : Technology B, Road A., 2000. Vol. 147.**

108. DNV. GasVLe. ***Veracity.*** **[Online] [Cited: 18 June 2023.] https://www.dnv.com/services/gasvle-8331.**

109. International Organization for Standardization. ***Reaction-to-fire tests, Heat release, smoke production and mass loss rate.*** **Geneva : s.n., 2015. BS ISO 5660.**

110. Twilley, W. H., Babrauskas, V. and Gaithersburg, M. D. User's guide for the cone calorimeter. ***National Bureau of Standards.*** **[Online] 1988. [Cited: 27 April 2018.] https://nvlpubs.nist.gov/nistpubs/Legacy/SP/nbsspecialpublication745.pdf. Report No.: NBS SP 745.**

111. Crawford, M. Factors From Finite Areas to Finite Areas. ***Radiation Confirguration Factors.*** **[Online] [Cited: 18 June 2023.] http://www.thermalradiation.net/calc/sectionc/C-12.html.**

112. Makino, H. and Amano, T. ***Demonstration of Crack Arrestability of X100 Line Pipe and Development of Evaluation Technologies for Three-dimensional Fracture Process.*** **Amagasaki : Nippon Steel and Sumitomo Metal, 2015. Technical Report No. 107.**

113. Wei, Z., Song, W., Lv, J., Fonzo, A., Mannucci, G. and Di Biagio, M. Ductile fracture propagation control in modern high strength steel pipeline for transportation of high pressure natural gas with H2 and CO2 contents: arrest requirements evaluation by numerical tool and full-scale testing verification. ***Pipeline Technology Journal.*** **[Online] [Cited: 29 November 2023.] https://www.pipeline-journal.net/articles/ductile-fracture-propagation-control-modern-high-strength-steel-pipeline-transportation.**

114. HSE. ***Report on a second study of pipeline accidents using the Health and Safety Executive's risk assessment programs MISHAP and PIPERS.*** **Norwich : HSE, 2002. https://www.hse.gov.uk/Research/rrpdf/rr036.pdf.**

115. Staggs, J. E. J. ***Convection heat transfer in the cone calorimeter.*** **Leeds : Fire Safety Journal, 2009. Vol. 44.**

116. Rbihi, S., Laallam, L., Sajieddine, M. and Jouaiti, A. ***Characterization and thermal conductivity of cellulose based composite xerogels.*** **Beni Mellal : Heliyon, 2019.**

117. Abbas, A., Zhao, Y., Zhou, J., Wang, X. and Lin, T. ***Improving Thermal Conductivity of Cotton Fabrics Using Composite Coatings Containing Graphene, Multiwall Carbon Nanotube or Boron Nitride Fine Particles.*** **Korea : Fibers and Polymers, 2013. Vol. 14.**

118. Zhao, J., Du, F., Zhou, X., Cui, W., Wang, X., Zhu, H., Xie, X. and Mai, Y. ***Thermal conductive and electrical properties of polyurethane/hyperbranched poly(urea-urethane)-grafted multi-walled carbon nanotube composites.*** **Wuhan : Composites Part B: Engineering, 2011. Vol. 42.**

119. Mishra, D., Dehury, J., Rout, L. and Satapathy, A. ***The effect of particle size, mixing conditions and agglomerates on thermal conductivity of BN-polyester***

& multi-sized BN-hybrid composites for use in micro-electronics. **Burla : Materials Today, 2020. Vol. 26.**

120. McAllister, S., Finney, M. and Cohen, J. *Critical mass flux for flaming ignition of wood as a function of external radiant heat flux and moisture content.* Atlanta : Combustion Institute, 2011.

121. Simms, D. and Law, M. *The ignition of west and dry wood by radiation.* Borehamwood : Combustion and Flame, 1967.

122. Dias, D., Machado, J., Leal, V., Mendes, A. *Impact of using cool paints on energy demand and thermal comfort of a residential building.* s.l. : Applied Thermal Engineering, 2014. Vol. 65.

123. Leung, E. H. and Halliday, D. X. *"Flashburning" — Interpreting the presence of heat damage to a suspect's clothing and footwear in the investigation of fires.* Ireland : Science and Justice, 2010.

124. Babrauskas, V. *Charring rate of wood as a tool for fire Charring rate of wood as a tool for fire.* Issaquah : Fire Safety Journal, 2005. Vol. 40.

125. Mitchell, M. Engauge Digitzer. *GitHub Pages.* [Online] [Cited: 15 October 2023.] https://markummitchell.github.io/engauge-digitizer/.

126. Sellami, I., Manescau, B., Chetehouna, K., De Izarra, C., Nait-Said, R. and Zidani, F. *BLEVE fireball modeling using Fire Dynamics Simulator (FDS) in an Algerian gas industry. Journal of Loss Prevention in the Process Industries.* Batna : Journal of Loss Prevention in the Process Industries, 2018. Vol. 54.